9-17-2015 12:00 AM

Dynamic studies of guest molecules in Metal-Organic Frameworks using Solid-State NMR

Yuanjun Lu
The University of Western Ontario

Supervisor
Yining Huang
The University of Western Ontario

Graduate Program in Chemistry
A thesis submitted in partial fulfillment of the requirements for the degree in Master of Science

Recommended Citation

Lu, Yuanjun, "Dynamic studies of guest molecules in Metal-Organic Frameworks using Solid-State NMR" (2015). *Electronic Thesis and Dissertation Repository*. 3237.
https://ir.lib.uwo.ca/etd/3237

DYNAMIC STUDIES OF GUEST MOLECULES IN METAL-ORGANIC FRAMEWORKS USING SOLID-STATE NUCLEAR MAGNETIC RESONANCE

(Thesis format: Monograph)

by

Yuanjun Lu

Graduate Program in Chemistry

A thesis submitted in partial fulfillment
of the requirements for the degree of
Master of Science

The School of Graduate and Postdoctoral Studies
The University of Western Ontario
London, Ontario, Canada

Abstract

Metal-organic frameworks (MOFs) are a new class of porous materials that possess large three-dimensional voids in their structures, which are ideal for applications such as gas adsorption and separation. In this work, Solid-state NMR (SSNMR) is used to examine the dynamics of guest molecules at various temperatures in MOFs that possess different types of channels. Chapter 2 introduces the $^{13}CO_2$ adsorption behavior in α-Mg formate studied by ^{13}C SSNMR in conjunction with molecular dynamic (MD) simulation. ^{1}H-^{13}C cross polarization (CP) technique has successfully determined the adsorption sites of CO_2 in this type of MOF to be hydrogen atoms. The dynamic analysis detects that at low temperature (room temperature and below), all of the adsorbed CO_2 undergo a localized rotation upon a single hydrogen site and a simultaneous non-localized two-sites hopping between two hydrogen sites, whereas at high temperature (above room temperature), a small portion of the adsorbed CO_2 molecules undergo only a localized rotation while the majority still follow the combined motion. Chapter 3 studies the ethylene adsorption behavior in α-Mg formate and CPO-27-M (M = Mg and Zn) by means of ^{2}H SSNMR. Two types of ethylene are found in α-Mg formate following distinct motions. The majority of the adsorbed ethylene undergoes a localized rotation and a simultaneous non-localized two-sites hopping, whereas the minority follows a localized rotation only. In CPO-27-M, all the adsorbed ethylene follows a localized rotation upon the unsaturated metal sites and a simultaneous non-localized hopping between six unsaturated metal sites. The affinity of ethylene towards CPO-27-Mg is found to be stronger than in CPO-27-Zn.

Keywords:

SSNMR, MOFs, CO_2, C_2H_4, dynamic study.

Co-Authorship Statement

Anmin Zheng (State Key Laboratory of Magnetic Resonance and Atomic and Molecular Physics, Wuhan Center for Magnetic Resonance, Wuhan Institute of Physics and Mathematics, Chinese Academy of Sciences, Wuhan, P. R. China) is credited for the molecular dynamic simulation of CO_2 adsorbed in α-Mg formate mentioned in Chapter 2.

Acknowledgement

Two years ago I decided to come to Canada and pursue a M.Sc. degree under the Dr. Yining Huang's supervision in Western University. Looking back, it has turned out to be one of the most brilliant decisions I have ever made. During these two years, I have come across so many talented and amazing individuals that my gratitude is really beyond my vocabulary. The supportive and friendly atmosphere in our department is very important for me to go this far.

First of all, I would like to give my deepest gratitude to my supervisor, Professor Yining Huang. Without him, I would not have started such an amazing journey. With his continuous support, I have had a very pleasant time working under his supervision. Second, I would like to thank Dr. Farhana Gulenoor, Dr. Wei David Wang and Dr. Jun Xu in our group for helping me find my way when I was first in the "Solid-state NMR maze"- with extreme patience. After they left our lab, our post-doc Dr. Bryan E.G. Lucier has become my savior every time I have NMR problem, as I can always get very helpful and sharp advice/solution from him. I would also like to thank Dr. Mathew Willians for his great help on the spectrometer. Dr. Paul Boyle from chem X-ray facility also helped me greatly for both my single crystal data and 9658 presentation, I really appreciate it. I would also like to thank Dr. Yang Song for his Powder diffraction course 9754, I really learnt a lot. Dr. Anmin Zheng from Wuhan Institute of Physics and Mathematics provided great help on molecular dynamic simulation, a special thanks to him as well.

I am so glad I have the opportunity of working as a teaching assistant with Janice Mathers, Sandy Holtslag and Sue England, as they have shown me what perfectly organized means, which has inspired me significantly in so many ways. In addition, I also want to thank Darlene McDonald for her great help in my grad study and life here, even before I came to Canada.

I would like to thank my friends Chen Rao, Weihong Gao, Yang Ye, Xuzhao Zhao, Shirley Fan, Saghar Khoshmashrab, Tianyu Qi, Jason Zhang, Yue Hu, Dan Vacarello, Fraser Filice, Maxwell Goldman, Vince Guo, Michelle Li, Shan Jiang, and Shoushun Chen for keeping me sane during tough times. I have had a great time with them and also learnt a lot from them.

I thank my parents for their unconditional and everlasting support for my life choice, study, and living expense. They always have faith in me, and I will try my best not to let them down.

At last, a special thanks to my partner Jeff VanKerkhove for his non-stop support.

Table of Contents

List of Figures

List of Tables

List of Abbreviations

BDC	1,4-benzendicarboxylate
CPO	Coordination Polymer of Oslo
CP	cross polarization
CSA	chemical shift anisotropy
DMF	N,N-dimethylformamide
DI	dipolar interaction
DOBDC	2,5-dioxido-1,4-benzenedicarboxylate
EFG	electric field gradient
EXPRESS	EXchange Program for RElaxing Spin Systems
FID	free induction decay
FT	Fourier transformation
HKUST	Hong Kong University of Science and Technology
MAS	magic angle spinning
MD	molecular dynamic
MIL	Materials of Institut Laviosier
MOF	metal-organic framework
NMR	Nuclear magnetic resonance
PAS	principal axis system
ppm	parts per million
pXRD	powder X-ray diffraction
QI	Quadrupolar interaction
SSNMR	Solid-State Nuclear magnetic resonance
TMS	tetramethylsilane
UiO	University of Oslo
ZIF	zeolitic imidazolate framework

List of Appendices

Chapter 1 Introduction

1.1 Metal-Organic Frameworks

Metal-organic frameworks, or MOFs, are a relatively new class of porous material with ultrahigh surface area.[1] In general, MOFs feature metal containing units (also known as secondary building unit, SBU) interconnected by organic linkers in three dimensions, creating crystalline porous structures. Since 1990, more than 20000 MOFs have been reported.[2] Figure 1.1 shows the framework structures of three well-studied MOFs, CPO-27-M,[3] (CPO is an acronym for Coordination Polymer of Oslo, also known as M_2(dobdc) or MOF-74. Metal centre: Mg, Co, Ni, Zn, Cu, Fe; Ligand: 2,5-dioxido-1,4-benzenedicarboxylate), HKUST-1 (acronym of Hong Kong University of Science and Technology, also known as Cu_3(BTC). Metal centre: Cu; Ligand: benzene-1,3,5-tricarboxylate, or BTC),[4] and MOF-5 (Metal centre: Zn, Ligand: 1,4-benzenedicarboxylate).[5] The three dimensional porous structures of these MOFs have made them exceptionally interesting in various industrial applications such as gas adsorption, separation, and catalysis.[2]

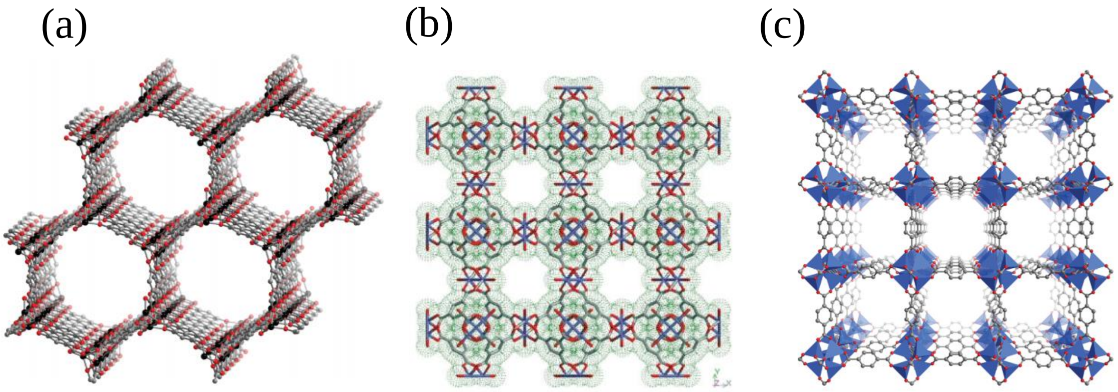

Figure 1.1 - Framework structures of CPO-27-Mg (a),[3] HKUST-1 (b),[4] MOF-5 (c).[5]

In order to accommodate those applications, long term chemical and physical stability of the materials is mandatory. Since MOFs are entirely composed of strong bonds, such as C-O, C-C, and M-O, they generally exhibit high thermal stability in the range of 250 ℃ to 500 ℃. However, some MOFs are sensitive to trace amount of chemicals in ambient condition, which would compromise their performances. For example, previous report suggests that MOF-5 retains only 28 % of its original porosity after 19 hours' exposure to 40 % relative humidity.[6] This property has made MOFs not entirely economical for industrial applications.

Enormous variability is one of the most attractive features of MOFs. Numerous SBU plus countless organic linkers give rise to an almost infinite number of MOFs. One classic case is CPO-27-Mg.[7] The metal centre can also be Co, Ni, Zn, Mn, Fe, and Cu while the framework remains isostructural. In 2012, Yaghi et al reported a series of isoreticular MOFs originating from CPO-27-M with substantially expanded pores.[8] The adopted organic linkers possess 2 to 11 phenyl rings, constructing a series of MOFs with pore sizes from 10 × 14 Å to as high as 85 × 98 Å. These results are very promising for applications such as gas adsorption and catalysis, which generally require large surface area for the reaction to take place.

Several methods have been reported to effectively produce MOFs with high crystallinity and long range 3D structure,[9] such as solvothermal, mechanochemistry,[10] electrochemistry,[11] and microwave heating.[12] Syntheses of MOFs are usually followed by solvent removal procedure which allows exposure of pores in the frameworks.[9] For the sake of large scale commercialization, a simple and rapid synthesis route under moderate conditions is preferential. One recent study reported a easy and straightforward way of preparing ZIF-8 (acronym of zeolitic imidazolate framework-8. Metal centre: Zn; ligand: 2-methylimidazole),[13] which only requires mixing the starting materials at room temperature. Another example is Mg formate MOF. BASF has applied a patent which reports mixing Mg oxide and formic acid at 75 ℃ would produce Mg formate with very good crystallinity.[14] So far, there are a number of MOFs that are commercially available, most of which are from BASF,[15] through their product series of "Basolite MOFs" including HKUST-1, ZIF-8, $Mg(O_2CH)_2$, and MIL-53-Al.

1.2 MOFs in gas adsorption

The high porosity of MOFs is of significant value in terms of gas adsorption and separation. Recent research has mainly focused on using MOFs as adsorbents for greenhouse gases and toxic chemicals such as CO_2, C_2H_4, H_2S, CO, NO, Cl_2, etc.[16]

CO_2 capture has been a hot research area arising from the increasing concerns of climate change. Currently, the biggest source of CO_2 emission is undoubtedly fossil fuel combustion. Two routes of capturing CO_2 using alkanolamine absorbents are generally adopted by the industries:[17] pre-combustion (CO_2 capture takes place at 30 bar and 40 ° C before combustion) and post-combustion capture (CO_2 capture takes place at 50-75 ℃ and 1 bar after combustion). After capture, CO_2 is desorbed and injected into a deep underground porous field (old oil well, or saline aquifer) to prevent leakage.[18] However, alkanolamine is known to slowly corrode the pipelines and vessels, potentially increasing the operating cost. In addition, this type of absorbents also suffers from stability issues during high temperature CO_2 desorption process. Therefore developing “harmless” absorbents that could function under mild operating conditions is urgent.

Large pore MOFs have proven to have better adsorption behavior in pre-combustion capture processes, whereas relatively small pore MOFs have demonstrated better performance in post combustion process due to the difference in their adsorption mechanisms.[19, 20] Because of the high pressure and ambient temperature condition during pre-combustion process, MOFs with high porosity are able to bear more CO_2. For instance, MOF-200, with Brunauer-Emmett-Teller (BET) surface area around 4530 m^2/g, is able to provide a CO_2 uptake of 2347 mg/g (235 wt %) at 50 bar.[19] On the other hand, in the context of post-combustion capture, a number of MOFs possessing modest porosity have shown exceptional adsorption behavior due to the presence of miscellaneous affinity sites, such as the unsaturated metal sites, amine, hydroxyl and thiol functional groups.[21-23] As mentioned earlier, MOFs bearing unsaturated metal sites like

HKUST-1 and CPO-27-M exhibit significantly high adsorption capacity due to the strong electronic interactions between the unsaturated metal nodes and CO_2 molecules. Similarly, electron donor-acceptor interaction is also the main reason why the functionalized MOFs show stronger adsorption than the non-functionalized ones. In J. Long's recent work, mmen (N,N′-dimethylethylenediamine) was used to functionalize Mg_2(dobpdc) (Metal centre: Mg, ligand: 4,4′-dioxido-3,3′- biphenyldicarboxylate), which is an expanded variant of CPO-27-Mg. The functionalized Mg_2(dobpdc) has displayed an exceptional capacity for CO_2 adsorption at extraordinarily low pressures. The CO_2 uptake is 2 mmol/g (8.1 wt %) at 0.39 mbar and 25 ℃,[24] which is 15 times higher than the unfunctionalized Mg_2(dobpdc). This is primarily due to the strong interaction between unpaired electrons on N- in mmen and CO_2. Hence tailoring functional groups onto organic linkers purposely has become a common strategy for improving adsorption behavior. MIL-53 (MIL is an acronym for Materials of Institut Lavoisier. Metal centre: Al; Ligand: benzene-1,4-dicarboxylate, BDC) is thought to be effective for both pre-combustion and post-combustion captures due to its unique structural change with respect to pressure and temperature.[25] At 25 bar and 304 K, MIL-53-Al with a pore size of 8.5×8.5 Å^2 is able to adsorb 30.6 wt % of CO_2,[26] whereas at 1 bar and 298 K, the pore size shrinks to 2.6×13.6 Å^2 and exhibits a CO_2 uptake of only about 10 wt %.[27] This unique pressure and temperature induced structural change is known as the breathing effect of this type of MOF.

Ethylene is involved in various important chemical processes in industries, such as the production of polyethylene and ethylene oxide.[28] Ethylene is primarily produced by petroleum steam cracking. During this process, a gaseous mixture including ethylene, methane, and propene is produced. The industrial method of trapping C_2H_4 from this gas mixture is by means of repeated condensation and distillation,[29] which is considered to be one of the most energy consuming steps in the production of C_2H_4. Therefore for the sake of energy consumption, it is important to develop absorbents that are able to selectively pick up ethylene under mild conditions. M. Bulow et al. reported the significant preferential adsorption behavior for ethylene over ethane by HKUST-1.[30] In this type of MOF, each Cu site is six coordinated. One coordination site is from the neighboring Cu atom; four other coordination sites are the contributions of two BTC ligands, and one more from solvent molecule.[5] Upon dehydration, the solvent molecule is removed and the Cu site is five coordinated and becomes unsaturated, also known as the open metal site. The preferential adsorption is attributed to the electrostatic interaction between π-electrons from C_2H_4 and partially positive charge of unsaturated Cu site on the frameworks. This observation is further supported by Wang and his co-workers' Monte Carlo simulation,[31] in which a selectivity factor of 2 for C_2H_4 over C_2H_6 is obtained. However, very few works have focused on the dynamics of adsorbed ethylene molecules in MOFs, which is strongly relevant to the selective adsorption.

1.3 Gas adsorption characterization

Several characterization methods have been reported to assist the thorough investigation of guest-host interactions in MOFs, such as single crystal or powder diffraction,[27,32] vibrational spectroscopy,[33] and nuclear magnetic resonance.[34]

Among these characterization methods, single crystal X-ray diffraction has been considered as the definitive structural determination method, which is able to provide the precise location of the adsorbed guest species. In the case of $Sc_2(BDC)_3$ MOF (Metal centre: Sc, ligand: Terephthalic acid),[32] single crystal X-ray diffraction successfully locates the position of the adsorbed CO_2, CH_4 and C_2H_6 molecules in the frameworks. A 14 ° rotation of the terephthalic linkers is found during CO_2 adsorption, resulting in two different types of triangular channels therefore two distinct types of CO_2 adsorption. The structure of CO_2 adsorbed $Sc_2(BDC)_3$ is shown in Figure 1.2a.

Although single crystal diffraction is a very powerful tool to accurately pinpoint the location of the guest species, it can be troublesome to perform due to the difficulty in preparing crystal samples with ideal quality. In addition, it is also unable to identify the location of light elements such as hydrogen. Therefore, powder X-ray diffraction (pXRD) and neutron diffractions are also commonly used in detecting guest-host interaction as alternative methods.[35] In the case of MIL-53-Cr,[27] a clear left shift of low angle peaks in pXRD pattern was observed after the introduction of CO_2, resulting from the breathing effect in this type of MOF, as shown in Figure 1.2b. In the case of CPO-27-Fe,[36] the use of neutron diffraction has successfully identified the adsorption sites, which are the unsaturated metal centres, as well as the adsorption behaviors upon the metal sites of a number of hydrocarbons.

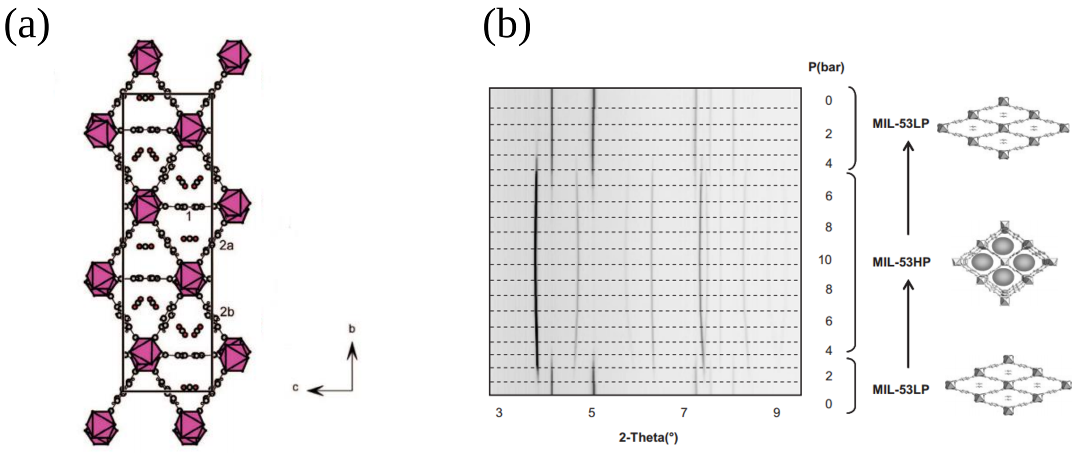

Figure 1.2 - Two sites adsorption of CO_2 molecules in ScBDC at 1 bar and 253 K (a),[32] and pXRD patterns of MIL-53-Cr under various pressures of CO_2 at 293 K (b).[27]

In addition to diffraction methods, vibrational spectroscopy (IR and Raman) is also commonly used to determine the motion of the adsorbed guest molecules. FTIR spectra have confirmed that the CO_2 adsorption site in CPO-27-Ni is at the unsaturated Ni sites with an end-on fashion.[33] An unusual splitting of the asymmetric stretching mode of CO_2 is also observed in IR spectrum, which can be interpreted by a bended structure of CO_2 molecules, other than its usual linear form. This result is further confirmed by powder XRD refinement, which shows the

O-C-O angle has become 162°. In the case of ZIF-8, in-situ high pressure IR spectrum clearly shows a direct interaction between CO_2 and imidazole ring on the framework, suggesting stronger adsorption behavior under high pressure.[37]

Multiple computational methods have been reported to predict the gas adsorption behaviors, as complements to experimental data due to their limitation in idealizing the system of interest.[38,39] With the use of grand canonical Monte Carlo molecular simulation, the position of the adsorbed hydrocarbons including C_2H_4, C_2H_6, C_3H_8, C_3H_6 in CPO-27-Mg is successfully identified, which is upon the unsaturated Mg sites exposed to the channels.[38] In this work, the molecular dynamic simulation conducted by our collaborator Dr. Anmin Zheng is also used to assist the determination of adsorption site of CO_2 in α-Mg formate.

1.4 Solid-state NMR in MOF studies

Nuclear magnetic resonance (NMR) has become a very useful tool in deriving fine structural information of materials.[40] Compared to commonly used solution NMR, solid state NMR (SSNMR) is relatively challenging due to the longer experimental time, complicated experimental setup, and more importantly, the difficulty in interpreting the broad powder pattern. Unlike the averaged signal resulting from the rapid molecular tumbling from solution NMR (isotropic sharp peaks), broad powder patterns are usually observed in SSNMR due to the randomly oriented molecules in solid phase.[41] With more advanced developments in hardware, techniques, and pulse sequences, such as magic angle spinning (MAS) and cross-polarization (CP),[42,43] as well as a number of simulation programs, more information can be obtained from SSNMR spectra.

One of the biggest uses of SSNMR in MOFs studies is structural determination. For instance, recent study of -Br and $-NH_2$ functionalized UiO-66-Zr (Metal centre: Zr; Ligand: 1,4 -

benzenedicarboxylic acid; Formula: $Zr_6O_4(OH)_4(CO_2)_{12}$) shows that with the use of ^{1}H SSNMR, spatial proximity of the non-equivalent H, metal centre, and functional groups can be successfully resolved.[44] ^{2}H NMR used in another study also regarding UiO-66-Zr discovered a distribution of the π-flipping rate of BDC ligand.[45] Our group has also reported a number of MOFs' studies using SSNMR. With ^{25}Mg NMR, we successfully refined the structure of α-$Mg_3(HCOO)_6$.[46] We also confirmed different oxygen species in CPO-27-Mg, UiO-66-Zr, MIL-53-Al, etc using ^{17}O NMR.[40] In one of our most recent publications, we studied a number of MOFs and identified the inaccuracies in previous structural reports.[47]

In addition to structural studies, SSNMR has also been widely used in revealing guest-host interactions. A classic and well-studied case is CPO-27-Mg.[34] With the use of ^{13}C SSNMR, a uniaxial rotation of a CO_2 molecule upon an open metal site is identified through a wide temperature range. A controversial result of this work is that the rotation angle of CO_2 molecules decreases as temperature increases, which is contradictory to the fact that gas molecules are more dynamic at higher temperature. In the follow-up study conducted by the same research group, the ^{13}C NMR spectra was further analyzed and interpreted into two distinct types of CO_2 motions at low and high temperatures.[48] They claimed that at sufficiently low temperature, the adsorbed CO_2 molecules undergo fluctuation around the minimum energy configuration near the open metal site. While the temperature reached 150 K, an intermediate movement of CO_2 molecules consisting of localized fluctuation and non-localized hopping between the six unsaturated metal centres in xy plane was predicted. Whereas at higher temperature, only a hopping motion of CO_2 molecules between six different open metal was found. However, ^{17}O NMR study from our group suggests that both localized wobbling and the non-localized hopping of CO_2 are present from 150 K to 403 K in this type of MOF, which is also confirmed by ^{13}C SSNMR results.[49] Other MOFs are also subjected to SSNMR study in terms of guest-host interactions studies and have shown unique adsorption behaviors. For example in CD-MOF-2 (Metal centre: Rb; Ligand: γ-cyclodextrin),[50] the discovery of carbonic acid using ^{13}C magic angle spinning (MAS) indicates a direct chemical reaction between CO_2 and the framework, instead of simple adsorption-desorption.

As mentioned earlier, the unsaturated metal sites in certain MOFs are the primary adsorption site for guest molecules. In some cases, SSNMR is also used in detecting the change in the metal cations' local environment in addition to direct guest species examination. By resolving the qudrupolar powder pattern of ^{25}Mg NMR of CPO-27-Mg,[51] Jun et al found that upon activation, which is the solvent removal process mentioned earlier in this chapter, the local environment of Mg became disordered due to the distortion of MgO_5 square-pyramid, while long-range ordering remained according to XRD results. When water was reintroduced back to the framework, the perfectly ordered structure was restored. A similar result was discovered when small organic molecules were introduced into the system.

Therefore, SSNMR is extremely useful for providing information about guest-host interactions in MOFs.

1.5 Physical background of SSNMR

In general, NMR active nuclei all possess intrinsic angular momentum, known as the spin (I). The values of I is positive half integer or integers (i.e. 1/2, 1, 3/2…). Some nuclei that have I = 0 do not possess intrinsic angular momentum. As a result, those nuclei are NMR inactive. An easy way to distinguish whether a nucleus is NMR active is by the number of protons and neutrons.[52] If the number of protons and neutrons are both even, these nuclei are NMR inactive. If there is an odd number of protons OR neutrons, or an odd number of protons AND neutrons, these nuclei are NMR active.

SSNMR interactions

Nuclear spins undergo different types of interactions with their surroundings in the presence of an external magnetic field. There are five nuclear spin interactions taking place in NMR, including Zeeman, dipolar, chemical shift, quadrupolar interactions (for spin I > 1/2), and scalar-coupling.[53] Their corresponding magnitudes are shown in Table 1-1.

Table 1-1. Nuclear interactions and the corresponding magnitudes

Nuclear interactions	Magnitude (Hz)
Zeeman	10^6~10^9
Dipolar	0~10^5
Chemical shift	0~10^5
Quadruplar	0~10^9
J (spin-spin)-coupling	0~10^4

Zeeman is known as the strongest among all interactions,[53] and all other interactions can be considered small perturbations of the Zeeman interaction. Since the first four interactions are involved in identifying host-guest behavior in this study, brief introductions are included in this section.

1) Zeeman interaction

Zeeman interaction refers to the interaction of the magnetic moment of the nuclear spin with external magnetic field. Without an external magnetic field, nuclei are all in the degenerate ground state. After being exposed to the magnetic field, the non-degeneracy of the ground state occurs and 2I + 1 energy levels are formed, distinguished by magnetic quantum number m_I (m_I = -I, -I + 1, -I + 2……, I - 2, I - 1, I.). The rate of transitions from low energy level to adjacent high energy level is termed as Larmor frequency, shown in equation 1. The energy split of a spin

1/2 nucleus after being exposed to external magnetic field (B_0) is shown in Figure 1.3 as illustration.[41]

$$\nu = \left(\frac{\gamma}{2\pi}\right) B_0 \tag{1}$$

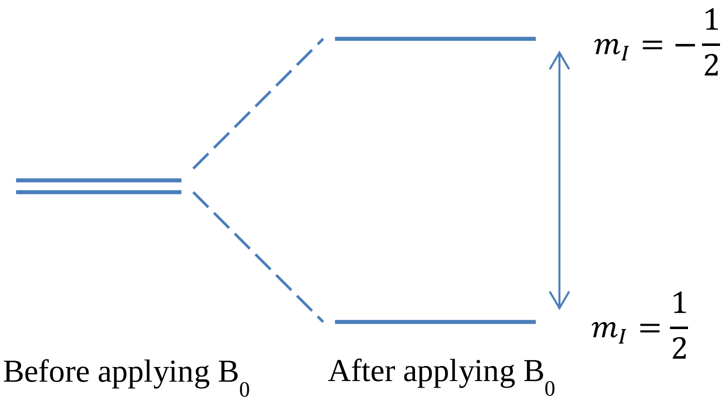

Figure 1.3 - Illustration of Zeeman interaction of a spin1/2 nucleus

where ν the nucleus dependent Larmor frequency, γ is the gyromagnetic ratio, an intrinsic property of the nucleus and B_0 is the applied magnetic field in Tesla.

The energy difference between the split levels can be calculated using following Equation 2.

$$\Delta E = h\nu = \left(\frac{h}{2\pi}\right)\gamma B_0 \tag{2}$$

Applying a higher magnetic field would create a larger gap between split energy levels, resulting in a stronger NMR signal.

2) Dipolar interaction

Dipolar interaction (DI) is a through space interaction between two spins, usually denoted by

I and S.[41] Each spin has a magnetic moment and can be considered as a small bar magnet, where each magnet yields a small local field felt by the other. Dipolar coupling constant (D) is used to quantify the strength of dipolar interaction, from which the frequency change induced by DI can be calculated, as shown the Equations 3 and 4. The principle of dipolar interaction is shown in Figure 4a.

$$D = \frac{\mu_o}{4\pi}\frac{\gamma_I\gamma_S}{r_{IS}^3}\frac{h}{2\pi} \tag{3}$$

$$\nu = \nu_L \pm \frac{1}{2}D(1 - 3\cos^2 \alpha) \tag{4}$$

where r_{IS} is the inter-nuclear distance, α is the angle between inter-nuclear vector and the direction of external magnetic field, μ_0 is the permeability of vacuum, γ_I and γ_S are the magnetogyric ratios of spin I and S, ν_L is the Larmor frequency, and ν is the modified frequency by DI. It is clear that DI has strong dependence on inter-nuclear distance, gyromagnetic ratio, and angle α. Figure 1.4b shows a typical Pake doublet NMR spectrum arising from dipolar coupling interaction for a heteronuclear powder sample.

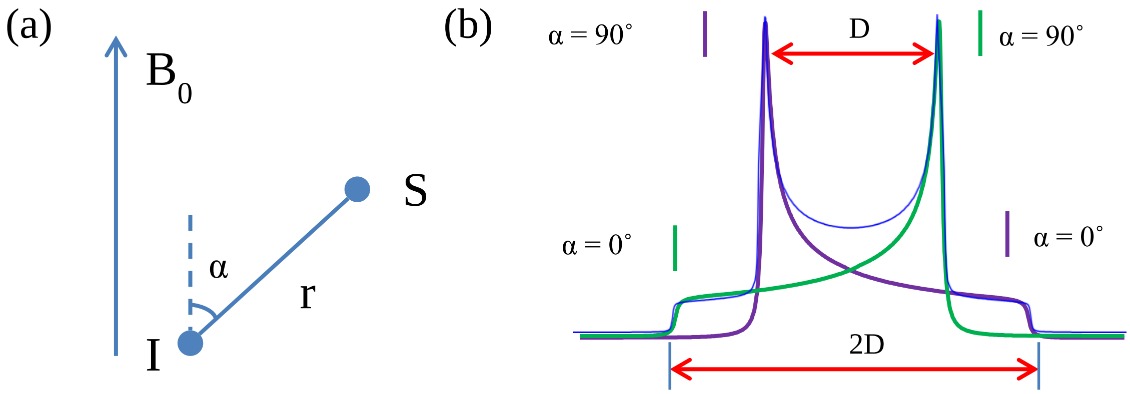

Figure 1.4 - Principle of dipolar interaction (a), and simulated dipolar coupling spectrum of two heterogeneous nuclei I and S (b). Purple and green lines represents the dipole of S either augment or cancel the magnetic field that I is experiencing. The blue line is the integrated Pake doublet powder pattern.

A typical Pake doublet is composed of two subspectra, which are ascribed to two opposite perturbations to Zeeman caused by the parallel and anti-parallel direction of the second spin with respect to B_0. The two “horns” arise from the 90 ° I-S vector with respect to B_0, and the two “feet” on the bottom are resulting from the I-S vector parallel to $B_{0.}$ The frequency gap between the two “horns” and two “feet” are exactly D and 2D, which is the most straightforward way of calculating the dipolar coupling constant. The higher intensity of the two horns are due to the numerous spin pairs with inter-nuclear vectors lying perpendicular to B_0, whereas the weaker intensity of the two “feet” result from significantly fewer spin pairs with inter-nuclear vectors lying along B_0. Experimentally, the broad and featureless NMR pattern arising from DI could be troublesome for further analysis. A feasible approach is to run magic angle spinning, which refers to tilting the sample tube to 54.74 ° with respect to B_0. As a result, the term $1 – 3\cos^2\alpha$ in Equation 4 equals 0, therefore $\nu = \nu_L$ and DI is successfully eliminated.

3) Chemical shift interaction

Placing a single atom into a magnetic field would induce circulation of the electronic cloud.[41] Accordingly, a small magnetic field is generated. If the generated magnetic field direction is opposite the main magnetic field, the nucleus is shielded from the main magnetic field by its own surrounding orbiting electrons, resulting in the shift of observed frequency, known as the chemical shift interaction (CS). Its influence on Zeeman can be interpreted by Equation 5.

$$\nu = \frac{\gamma}{2\pi}B = \frac{\gamma}{2\pi}B_0(1-\sigma) \tag{5}$$

where ν is the resonance frequency, B_0 and B represent the main and modified magnetic field, respectively, and σ is the chemical shielding constant ($\ll 1$). σ is represented by three principal components, σ_{11}, σ_{22} and σ_{33}, along the three orthogonal directions of molecular framework, as known as chemical shielding anisotropy (CSA). In solution phase, molecules undergo rapid reorientation therefore the chemical shielding anisotropy is averaged-out, resulting in sharp peaks in comparison with the broad powder pattern obtained by SSNMR.

According to Equation 5 it is not hard to see that chemical shielding is magnetic field dependent. Therefore it is hard to compare spectra obtained from different fields. In order to solve this problem, chemical shift tensors are introduced as an alternative to σ, as shown in Equation 6.

$$\delta = \frac{10^6(\nu - \nu_{ref})}{\nu_{ref}} \tag{6}$$

where δ is chemical shift, which represents the frequency difference between the reference sample and sample of interest in the form of part per million (ppm), ν_{ref} and ν are the resonance frequency of reference sample and sample of interest. In this case, the field dependency is easily eliminated. As with σ, chemical shift δ is also represented by three principal values, δ_{11}, δ_{22} and δ_{33} along the three orthogonal directions of molecular frame, as known as the principal axis system (PAS). The three components are in the order of $\delta_{11} > \delta_{22} > \delta_{33}$. For linear molecules such as CO_2 and C_2H_2, δ_{33} is along the molecular axis and δ_{11} and δ_{22} are equivalent and perpendicular to δ_{33}. As an example, PAS of a CO_2 molecule is shown in Figure 1.5 a, and ^{13}C spectrum of stationary $^{13}CO_2$ is shown in Figure 1.5 b.

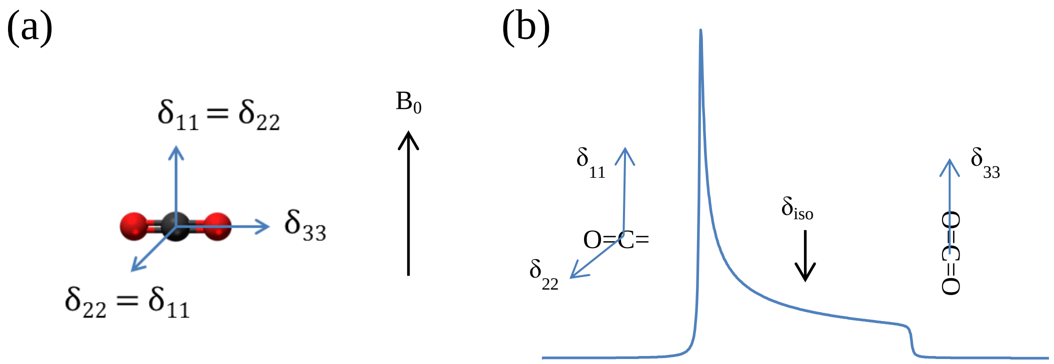

Figure 1.5 - PAS of CO_2 molecule (a), and simulated ^{13}C spectrum of CO_2 (b).

The shape of the ^{13}C spectrum of CO_2 is well-known as the axial symmetric powder pattern, which is generally discovered among linear molecules. In a powder sample, molecules are randomly oriented and stationary. The CO_2 molecules lie perpendicular to B_0 give rise to the more intense resonance at less shielded side, which correspond to δ_{11} and δ_{22}. In comparison, much less CO_2 molecules lie along B_0, resulting in weak signal at more shielded side, which is corresponding to δ_{33}. The CO_2 molecules oriented between 0° and 90° with respect to B_0 give rise to resonance in between the two edges. Accordingly, a broad powder pattern is observed.

Herzfeld-Berger convention is used in this work to quantitatively interpret NMR line shape, as shown in Equation 7-9:[54]

$$\delta_{iso} = \frac{1}{3}(\delta_{11} + \delta_{22} + \delta_{33}) \tag{7}$$

$$\Omega = \delta_{11} - \delta_{33} \tag{8}$$

$$\kappa = \frac{3(\delta_{22} - \delta_{iso})}{\Omega} \tag{9}$$

Isotropic chemical shift δ_{iso} is simply the average of the three principal CS tensor components, which is also the observed frequency if the nucleus of interest is in solution phase. In addition, δ_{iso} of the same nucleus in different compounds exhibit distinctive values, which assist the identification of the chemical environments of the nucleus of interest. Span Ω describes the whole width of the spectra, and skew κ illustrates the symmetry of the spectrum, which ranges within -1 to 1. Axial symmetric powder patterns is generally observed when symmetry of C_3 or higher reside at the nucleus site, which show a skew value of 1 or -1. For the spectrum with κ between 1 and -1, it is known as the asymmetric powder pattern, indicating a less symmetric local structure of C_2 or less. The influence of Ω, κ and δ_{iso} on NMR spectrum is shown in Figure 1.6.

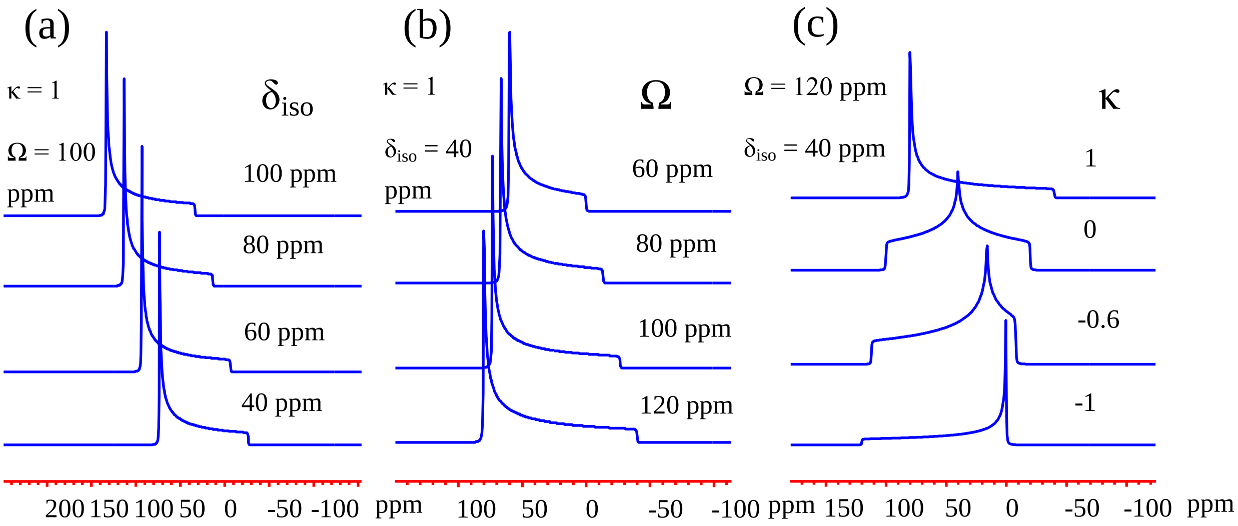

Figure 1.6 - The influence of δ_{iso} (a), Ω (b), and κ (c) on ^{13}C NMR line shape.

4) Quadrupolar interaction

All nuclei with a spin number greater than 1/2 hold an electric quadrupole moment, resulting from the non-spherical charge distribution. The nuclear quadrupole moment Q is able to couple with the local electric field gradients (EFG) and gives rise to quadrupolar interaction (QI). Similar to chemical shielding interaction, QI is characterized by three components of the EFG tensors in principal axis system (PAS), V_{xx}, V_{yy} and V_{zz} (V_{zz} is the largest principal component), and in the order of $V_{zz} > V_{yy} > V_{xx}$. When evaluating QI, two commonly reported parameters are the quadrupolar coupling constant (C_Q) and the asymmetry (η_Q), as shown in Equation 10 and 11.[52]

$$C_Q = \frac{eQV_{zz}}{h} \tag{10}$$

$$\eta_Q = (V_{xx} - V_{yy})/V_{zz} \tag{11}$$

The magnitude of C_Q indicates the strength of the QI. The higher the value, the more non-symmetric the geometry of the nucleus is, resulting in stronger QI. η_Q is used to describe the symmetry of the spectrum, ranging from 0 to 1.

In the third chapter of this work, deuterium NMR is conducted to examine the adsorption behaviors of deuterated ethylene in MOFs. Deuterium is a spin 1 quadrupolar nucleus that possesses a relatively small Q, which is on the order of 10^{-3} barn in comparison with 10^{-2} or 10^{-1} barn of other quadrupolar nuclei.[55] As a result, the line shape of ^{2}H SSNMR is usually narrow and very sensitive to any sort of motional change including the reorientation of the molecules or the increasing or decreasing of the exchange rate. Therefore, ^{2}H SSNMR is widely used to determine the molecular dynamics.

The observed spectrum also shapes into Pake doublet, just like the dipolar interaction induced ones.[56] However, the origin is different in these two cases. With the presence of an external magnetic field, the degenerate energy levels of deuterium nucleus split into three due to Zeeman interaction, corresponding to three spin quantum number, $m_I = +1$, $m_I = 0$, and $m_I = -1$. And the two energy transitions between the three energy levels show identical values. The observed Pake doublet in ^{2}H SSNMR is the result of first-order quadrupolar interaction, which acts as the perturbation of the Zeeman states, as shown in Figure 1.7 a. Two subspectra are clearly observed in the Pake doublet due to the opposite change in the two transitions, corresponding to transitions from m_I = -1 to 0 and from m_I = 0 to 1. In most organic compounds,

V_{zz} is typically along C-D or O-D vector, and V_{xx} and V_{yy} are equivalent and perpendicular to Vzz.[57] As a result, the two subspectra are also axially symmetric. More C-D or O-D are likely to be perpendicular to B_0, resulting in high intensity of the two “horns”. The C-D or O-D bonds lie along B_0, on the other hand, give rise to weak resonance as two “feet”. And the bonds that lie between these two extreme conditions give rise to resonance in between. Consequently, two axially symmetric powder patterns are observed and compose a Pake doublet.

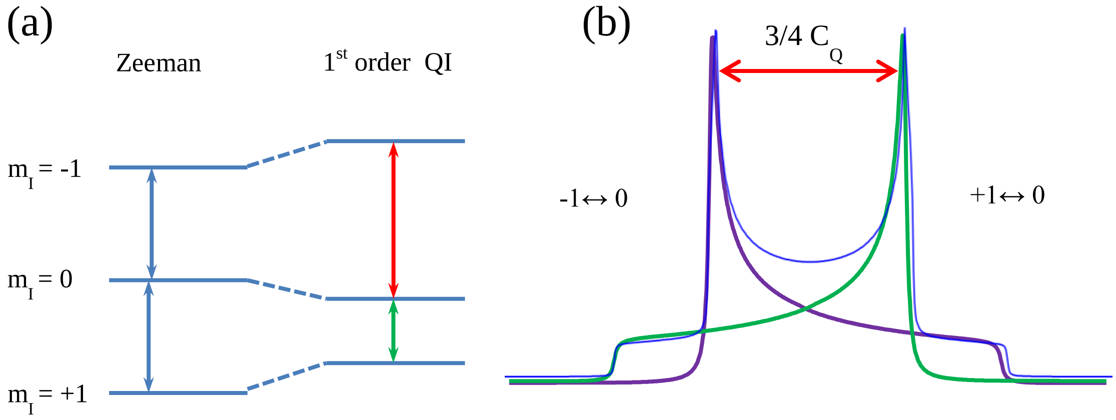

Figure 1.7 - Qualitative illustration of the energy split of ^{2}H nucleus (a). Simulated NMR spectrum of ^{2}H (b). The green and purple lines are from two transitions between +1↔ 0 and -1↔ 0. The blue line is the integrated Pake doublet powder pattern.

C_Q can be easily calculated by the frequency difference between the two horns of the Pake doublet, which equals 3/4 of C_Q. Figure 1.8 shows the influence of C_Q and η_Q on SSNMR spectrum.

With decreasing C_Q, the width of the spectrum decreases as well as the distance between two horns. When η_Q increases from 0 to 1, the width of the spectrum remains the same while the two horns are gradually merging together.

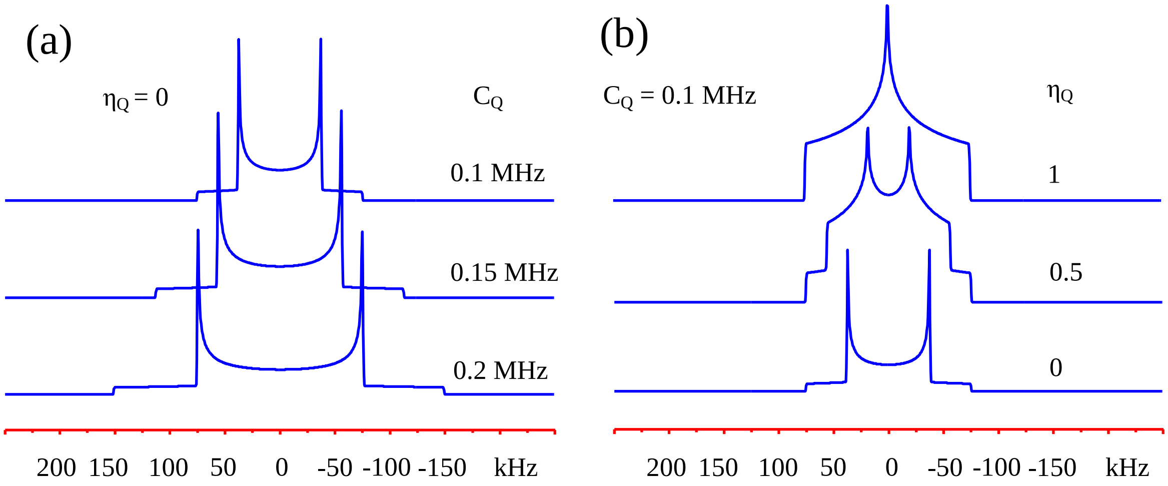

Figure 1.8 - The effect of C_Q (a) and η_Q (b) towards ^{2}H NMR line shape.

1.6 Experimental background of SSNMR

In order to demonstrate the change of magnetization during NMR experimentation in a simple and straightforward manner, a vector model consisting of a Cartesian coordinate system known as the rotating frame of reference is introduced in this section. Here, a simple 90 ° pulse (some time denoted as a π/2 pulse) experiment is demonstrated in Figure 1.9.

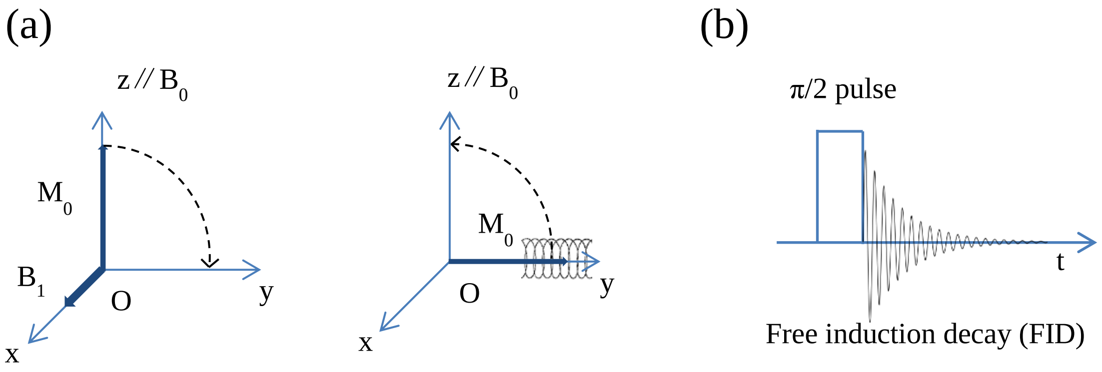

Figure 1.9 - Schematic of one pulse experiment in vector model (a) and in time domain (b).

Generally, the external magnetic field B_0 is considered along z axis of this frame. During SSNMR experiment, after a sample is placed in a magnetic field, the magnetic moments of the nuclei would generate a net magnetization that lie along B_0, denoted as M_0. The detection coil of the NMR probe can be considered in the xy plane of the rotating frame. Therefore, in order to make M_0 detectable, a 90 °rotation of the magnetization from z axis to xy plane is performed by applying second magnetic field B_1 along x axis. After M_0 is rotated to the xy plane and recorded, B_1 is switched off. The net magnetization then gradually relaxes back to the z axis to achieve thermal equilibrium due to B_0. This relaxation process gives rise to an oscillating signal termed as free induction decay (FID) in the time domain, shown in Figure 1.9b. Fourier transformation (FT) is then performed to convert the FID into frequency domain.

1.6.1 NMR pulse sequences

Multiple pulse sequences are programmed based on the simple one pulse experiment to fulfill various purposes. Here, time domain schemes of some pulse sequences used in this work are briefly introduced, as shown in Figure 1.10.

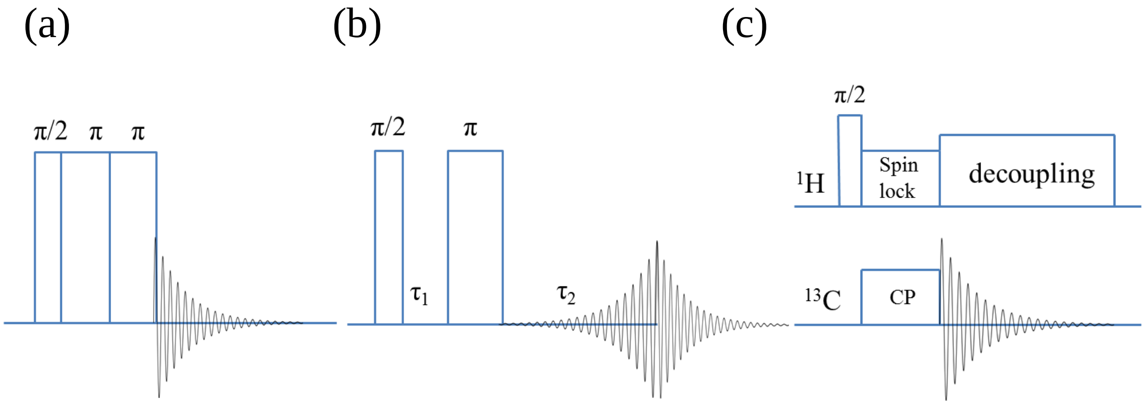

Figure 1.10 - Schematic of pulse sequences of DEPTH (a), Echo (b), and Cross Polarization (CP) (c).

1) DEPTH

DEPTH sequence originates from a simple 90° pulse experiment and is normally used to eliminate the background resonance originating from probe materials.[58] Generally, DEPTH consists of one $\pi/2$ pulse followed by two consecutive π pulses, as shown in Figure 1.10 a. In this case, the magnetization from the probe would be rotated further away from the transverse plane where the detection lies after three consecutive pulses. As a result, the resonance of the probe is too weak to collect.

2) Echo

In certain cases, the relaxation time of nuclei can be so fast that there is not enough time for the current to transfer from applying B_1 to receiving radio frequency energy from the sample. As a result, a broad and truncated powder pattern is sometimes observed due to failure in collecting the full FID. Echo sequence is designed for this situation.[59] An initial $\pi/2$ pulse rotates the magnetization to the xy plane, followed by echo dephasing time τ_1. During this time, magnetizations start to evolve with different paces in the transverse plane. Then, a π pulse is applied to "flip" the magnetizations 180°, which would refocus them back to the detection coil over the course of τ_2. This process is known as "echo", after which FID is collected. °

3) Cross Polarization (CP)

Some nuclei are known to be NMR unfavorable due to various reasons such as long relaxation time, low natural abundance, or low gyromagnetic ratio γ. The spectra of such nuclei usually show low signal-to-noise ratios as well as long experimental time. Cross polarization (CP) is designed to transfer magnetization from NMR favorable nuclei (such as ^{1}H and ^{19}F) to unfavorable ones (such as ^{13}C and ^{17}O) via dipolar coupling, resulting in higher signal-to-noise ratios and faster acquisition.[60] The polarization transfer between two nuclei that possess different Larmor frequencies is achieved by satisfying the Hartmann-Hahn condition, as shown in Equation 12.

$$\gamma_S B_S = \gamma_I B_I \tag{12}$$

where γ_S and γ_I are the gyromagnetic ratio of dilute spin S and abundant spin I, B_I and B_S are the radio frequency fields that are applied on two channels for two nuclei. Here, one of the most common CP experiments, ^1H-^{13}C cross polarization, is used for illustration, where ^1H is known as abundant spin, and ^{13}C is the dilute spin, as shown in Figure 1.8 c. After applying a $\pi/2$ pulse on ^1H channel, a spin lock pulse B_I is then applied to keep the magnetization from dephasing. Meanwhile, another pulse B_S is applied to ^{13}C channel so that the magnetization of ^{13}C will be built up in xy plane due to dipolar coupling. This period is known as the contact time. Longer contact time allows ^1H to enhance the signal of ^{13}C nuclei weakly coupled to it, or in other word, ^{13}C nuclei that are distant to it. Whereas shorter contact time, the signal enhancement only happens between strongly coupled ^1H and ^{13}C. Then, decoupling occurs on the ^1H channel, and the ^{13}C FID is collected.

1.6.2 Spectrum simulation

In SSNMR study, several simulation software packages are developed to assist in explaining the results. Among them, NUTs is usually used for NMR data processing such as Fourier transformation, phase correction and line broadening;[61] WSolids and dmfit software packages are used to derive NMR parameters such as chemical shift parameters δ_{iso}, Ω and κ,[62,63] quadrupolar parameters C_Q and η_Q, and dipolar coupling constant D. EXPRESS (EXchange Program for RElaxing Spin Systems) simulation based on Matlab platform is generally used to predict the dynamics of guest molecules.[64] The principle of EXPRESS simulation is to virtually apply certain degree and rate of rotations to the PAS of the guest species, which then give rise to corresponding simulated NMR spectrum. Two simultaneous sets of rotation are involved in simulating the dynamics of guest molecules in this work. Firstly, the PAS of EFG/CSA tensors are brought into alignment with an intermediate jumping frame by three consecutive rotations involving angles α, β and γ, known as the Euler angle.[65] This operation is considered to be equivalent to a localized rotation of the guest molecules upon single adsorption site. Secondly, the intermediate jumping frame is rotated to different orientations in the crystal fixed frame, which is considered to be equivalent to non-localized hopping between the adsorption sites. The above-mentioned software packages are all used in this study.

1.7 Outline of thesis

Conducting SSNMR experiments at various temperatures (VT) is extremely useful for investigating guest-host interactions, particularly gas adsorption behavior in this work. With the help of conventional simulation packages, the NMR parameters such as chemical shift parameters, dipolar coupling constant, and quadrupolar coupling constant, as well as the dynamics of guest molecules at different temperatures can be obtained. In the second chapter of this study, CO_2 adsorbed in α-Mg formate is studied. ^{13}C NMR is used to analyze CO_2 mobility from 173 K to 393 K, and ^{1}H-^{13}C CP experiments were carried out to investigate the adsorption site in α-Mg formate. Molecular dynamic simulations conducted by our collaborators provide complementary results about CO_2 distribution in the framework. The third chapter of this work focuses on ethylene adsorbed in different types of MOFs, including α-Mg formate and CPO-27-M (M = Mg and Zn). ^{2}H NMR is adopted to show mobility changes of deuterium enriched ethylene from 173 K to 393 K in three types of MOFs. Among these MOFs, CPO-27-M with Mg and Zn are isostructural, so the similarities and differences in adsorption properties are compared. Single crystal X-ray diffraction is performed upon ethylene adsorbed α-Mg formate as a complementary method to comprehend the adsorption behavior. By the end of chapter 3, the origin of the different adsorption behaviors of CO_2 and C_2H_4 in α-Mg formate is also discussed in this chapter. The last chapter of this work discusses future work and conclusions.

1.8 Bibliography

(1) Zhou, H.-C.; Long, J. R.; Yaghi, O. M. *Chemical Reviews* **2012**, *112*, 673.

(2) Furukawa, H.; Cordova, K. E.; O'Keeffe, M.; Yaghi, O. M. *Science* **2013**, *341*.

(3) Dietzel, P. D. C.; Blom, R.; Fjellvåg, H. *European Journal of Inorganic Chemistry* **2008**, *2008*, 3624.

(4) Chui, S. S.-Y.; Lo, S. M.-F.; Charmant, J. P. H.; Orpen, A. G.; Williams, I. D. *Science* **1999**, *283*, 1148.

(5) Dybtsev, D. N.; Nuzhdin, A. L.; Chun, H.; Bryliakov, K. P.; Talsi, E. P.; Fedin, V. P.; Kim, K. *Angewandte Chemie International Edition* **2006**, *45*, 916.

(6) Guo, P.; Dutta, D.; Wong-Foy, A. G.; Gidley, D. W.; Matzger, A. J. *Journal of the American Chemical Society* **2015**, *137*, 2651.

(7) Rosnes, M. H.; Opitz, M.; Frontzek, M.; Lohstroh, W.; Embs, J. P.; Georgiev, P. A.; Dietzel, P. D. C. *Journal of Materials Chemistry A* **2015**, *3*, 4827.

(8) Deng, H.; Grunder, S.; Cordova, K. E.; Valente, C.; Furukawa, H.; Hmadeh, M.; Gándara, F.; Whalley, A. C.; Liu, Z.; Asahina, S.; Kazumori, H.; O'Keeffe, M.; Terasaki, O.; Stoddart, J. F.; Yaghi, O. M. *Science* **2012**, *336*, 1018.

(9) Stock, N.; Biswas, S. *Chemical Reviews* **2012**, *112*, 933.

(10) Klimakow, M.; Klobes, P.; Thünemann, A. F.; Rademann, K.; Emmerling, F. *Chemistry of Materials* **2010**, *22*, 5216.

(11) Campagnol, N.; Van Assche, T.; Boudewijns, T.; Denayer, J.; Binnemans, K.; De Vos, D.; Fransaer, J. *Journal of Materials Chemistry A* **2013**, *1*, 5827.

(12) Klinowski, J.; Almeida Paz, F. A.; Silva, P.; Rocha, J. *Dalton Transactions* **2011**, *40*, 321.

(13) Cravillon, J.; Münzer, S.; Lohmeier, S.-J.; Feldhoff, A.; Huber, K.; Wiebcke, M. *Chemistry of Materials* **2009**, *21*, 1410.

(14) Leung, E.; Mueller, U.; Cox, G.; WO/2010/106121; 2010.

(15) *Sigma-Aldrich*. http://www.sigmaaldrich.com/ *(May 1, 2015).*

(16) DeCoste, J. B.; Peterson, G. W. *Chemical Reviews* **2014**, *114*, 5695.

(17) Sumida, K.; Rogow, D. L.; Mason, J. A.; McDonald, T. M.; Bloch, E. D.; Herm, Z. R.; Bae, T.-H.; Long, J. R. *Chemical Reviews* **2011**, *112*, 724.

(18) *Clean Coal Test: Power Plants Prepare to Capture Carbon.* *http://news.nationalgeographic.com/news/energy/2014/03/140331-carbon-capture-kemper-coal-climate/* *(Accessed May 1, 2015).*

(19) Furukawa, H.; Ko, N.; Go, Y. B.; Aratani, N.; Choi, S. B.; Choi, E.; Yazaydin, A. Ö.; Snurr, R. Q.; O'Keeffe, M.; Kim, J.; Yaghi, O. M. *Science* **2010**, *329*, 424.

(20) Stavitski, E.; Pidko, E. A.; Couck, S.; Remy, T.; Hensen, E. J. M.; Weckhuysen, B. M.; Denayer, J.; Gascon, J.; Kapteijn, F. *Langmuir* **2011**, *27*, 3970.

(21) Millward, A. R.; Yaghi, O. M. *Journal of the American Chemical Society* **2005**, *127*, 17998.

(22) Llewellyn, P. L.; Bourrelly, S.; Serre, C.; Vimont, A.; Daturi, M.; Hamon, L.; De Weireld, G.; Chang, J.-S.; Hong, D.-Y.; Kyu Hwang, Y.; Hwa Jhung, S.; Férey, G. *Langmuir* **2008**, *24*, 7245.

(23) Zhao, Y.; Wu, H.; Emge, T. J.; Gong, Q.; Nijem, N.; Chabal, Y. J.; Kong, L.; Langreth, D. C.; Liu, H.; Zeng, H.; Li, J. *Chemistry – A European Journal* **2011**, *17*, 5101.

(24) McDonald, T. M.; Lee, W. R.; Mason, J. A.; Wiers, B. M.; Hong, C. S.; Long, J. R. *Journal of the American Chemical Society* **2012**, *134*, 7056.

(25) Jiang, Y.; Huang, J.; Marx, S.; Kleist, W.; Hunger, M.; Baiker, A. *The Journal of Physical Chemistry Letters* **2010**, *1*, 2886.

(26) Bourrelly, S.; Llewellyn, P. L.; Serre, C.; Millange, F.; Loiseau, T.; Férey, G. *Journal of the American Chemical Society* **2005**, *127*, 13519.

(27) Serre, C.; Bourrelly, S.; Vimont, A.; Ramsahye, N. A.; Maurin, G.; Llewellyn, P. L.; Daturi, M.; Filinchuk, Y.; Leynaud, O.; Barnes, P.; Férey, G. *Advanced Materials* **2007**, *19*, 2246.

(28) Rebsdat, S.; Mayer, D. In *Ullmann's Encyclopedia of Industrial Chemistry*; Wiley-VCH Verlag GmbH & Co. KGaA: 2000.

(29) Geier, S. J.; Mason, J. A.; Bloch, E. D.; Queen, W. L.; Hudson, M. R.; Brown, C. M.; Long, J. R. *Chemical Science* **2013**, *4*, 2054.

(30) Min Wang, Q.; Shen, D.; Bülow, M.; Ling Lau, M.; Deng, S.; Fitch, F. R.; Lemcoff, N. O.; Semanscin, J. *Microporous and Mesoporous Materials* **2002**, *55*, 217.

(31) Wang, S.; Yang, Q.; Zhong, C. *Separation and Purification Technology* **2008**, *60*, 30.

(32) Miller, S. R.; Wright, P. A.; Devic, T.; Serre, C.; Férey, G.; Llewellyn, P. L.; Denoyel, R.; Gaberova, L.; Filinchuk, Y. *Langmuir* **2009**, *25*, 3618.

(33) Dietzel, P. D. C.; Johnsen, R. E.; Fjellvag, H.; Bordiga, S.; Groppo, E.; Chavan, S.; Blom, R. *Chemical Communications* **2008**, 5125.

(34) Kong, X.; Scott, E.; Ding, W.; Mason, J. A.; Long, J. R.; Reimer, J. A. *Journal of the American Chemical Society* **2012**, *134*, 14341.

(35) Carrington, E. J.; Vitorica-Yrezabal, I. J.; Brammer, L. *Acta Crystallographica Section B* **2014**, *70*, 404.

(36) Bloch, E. D.; Queen, W. L.; Krishna, R.; Zadrozny, J. M.; Brown, C. M.; Long, J. R. *Science* **2012**, *335*, 1606.

(37) Hu, Y.; Liu, Z.; Xu, J.; Huang, Y.; Song, Y. *Journal of the American Chemical Society* **2013**, *135*, 9287.

(38) Pham, T.; Forrest, K. A.; Eckert, J.; Georgiev, P. A.; Mullen, A.; Luebke, R.; Cairns, A. J.; Belmabkhout, Y.; Eubank, J. F.; McLaughlin, K.; Lohstroh, W.; Eddaoudi, M.; Space, B. *The Journal of Physical Chemistry C* **2014**, *118*, 439.

(39) Zhang, Z.; Li, Z.; Li, J. *Langmuir* **2012**, *28*, 12122.

(40) He, P.; Xu, J.; Terskikh, V. V.; Sutrisno, A.; Nie, H.-Y.; Huang, Y. *The Journal of Physical Chemistry C* **2013**, *117*, 16953.

(41) Duer, M. J. *Solid-state NMR spectroscopy: principles and applications*; Oxford: Blackwell Science, 2002.

(42) Andrew, E. R.; Bradbury, A.; Eades, R. G. *Nature* **1958**, *182*, 1659.

(43) Pines, A.; Gibby, M. G.; Waugh, J. S. *The Journal of Chemical Physics* **1973**, *59*, 569.

(44) Devautour-Vinot, S.; Maurin, G.; Serre, C.; Horcajada, P.; Paula da Cunha, D.; Guillerm, V.; de Souza Costa, E.; Taulelle, F.; Martineau, C. *Chemistry of Materials* **2012**, *24*, 2168.

(45) Kolokolov, D. I.; Stepanov, A. G.; Guillerm, V.; Serre, C.; Frick, B.; Jobic, H. *The Journal of Physical Chemistry C* **2012**, *116*, 12131.

(46) Xu, J.; Terskikh, V. V.; Huang, Y. *Chemistry – A European Journal* **2013**, *19*, 4432.

(47) He, P.; Lucier, B. E. G.; Terskikh, V. V.; Shi, Q.; Dong, J.; Chu, Y.; Zheng, A.; Sutrisno, A.; Huang, Y. *The Journal of Physical Chemistry C* **2014**, *118*, 23728.

(48) Lin, L.-C.; Kim, J.; Kong, X.; Scott, E.; McDonald, T. M.; Long, J. R.; Reimer, J. A.; Smit, B. *Angewandte Chemie International Edition* **2013**, *52*, 4410.

(49) Wang, W. D.; Lucier, B. E. G.; Terskikh, V. V.; Wang, W.; Huang, Y. *The Journal of Physical Chemistry Letters* **2014**, *5*, 3360.

(50) Gassensmith, J. J.; Furukawa, H.; Smaldone, R. A.; Forgan, R. S.; Botros, Y. Y.; Yaghi, O. M.; Stoddart, J. F. *Journal of the American Chemical Society* **2011**, *133*, 15312.

(51) Xu, J.; Terskikh, V. V.; Huang, Y. *The Journal of Physical Chemistry Letters* **2013**, *4*, 7.

(52) Levitt, M. H. *Spin Dynamics Basics of Nuclear Magnetic Resonance*; John Wiley & Sons Ltd: West Sussex, England, 2007.

(53) MacKenzie, K. S., M. E. *Multinuclear Solid-State Nuclear Magnetic Resonance of Inorganic Materials, 1st Edition*; Pergamon: Oxford, 2002.

(54) Harris, R. K.; Becker, E. D.; De Menezes, S. M. C.; Granger, P.; Hoffman, R. E.; Zilm, K. W. *Solid State Nucl. Magn. Reson.* **2008**, *33*, 41.

(55) Stone, N. J. *Atomic Data and Nuclear Data Tables* **2005**, *90*, 75.

(56) Pake, G. E. *The Journal of Chemical Physics* **1948**, *16*, 327.

(57) Nandagopal, M.; Utz, M. *Journal of Chemical Physics* **2005**, *123*.

(58) Cory, D. G.; Ritchey, W. M. *Journal of Magnetic Resonance* **1988**, *80*, 128.

(59) Tanner, J. E.; Stejskal, E. O. *The Journal of Chemical Physics* **1968**, *49*, 1768.

(60) Hartmann, S. R.; Hahn, E. L. *Physical Review* **1962**, *128*, 2042.

(61) *Acorn NMR Inc.* http://www.acornnmr.com/nuts.htm *(July 15, 2015).*

(62) *Software Klaus Eichele.* http://anorganik.uni-tuebingen.de/klaus/soft/index.php *(July 15, 2015).*

(63) *NMR@CEMHTI.* http://nmr.cemhti.cnrs-orleans.fr/dmfit/default.aspx *(July 15, 2015).*

(64) Vold, R. L.; Hoatson, G. L. *Journal of Magnetic Resonance* **2009**, *198*, 57.

(65) Rose, M. E. *Elementary Theory of Angular Momentum*; Wiley: New York, 1957.

Chapter 2 Dynamic study of $^{13}CO_2$ in α-Mg formate using ^{13}C SSNMR

2.1 Introduction

Among all MOFs, those containing s block metals are especially attractive in comparison with transition metals due to their cheap cost, light weight, and high natural abundance.[1,2] Previously reported microporous α-magnesium formate (α-$Mg_3(HCOO)_6$) MOF is easily-prepared, inexpensive, and structurally stable for a wide range of temperature.[3,4] Among all its analogues containing different metal centres,[5] α-Mg formate is the only commercially available formate MOF (trade name Basosiv M050, BASF), which possesses large one dimensional channels that have made it particularly interesting for gas adsorption studies.[6] In this chapter, ^{13}C SSNMR in conjunction with molecular dynamic simulation is used to study CO_2 adsorption behavior in α-Mg formate at various temperatures.

Three types of Mg formate with slight variations in structure have been reported.[3] α-Mg-formate crystallizes in monoclinic space group $P2_1/n$, whereas β and γ-Mg-formate crystallize in orthorhombic space group $Pca2_1$ and Pbcn. Due to the simple synthesis route of α-Mg formate and the difficulty in preparing pure phase β and γ-Mg-formate,[3,7] α-Mg-formate is chosen as the focus of this work. According to previous reports, a simple solvothermal reaction takes place at moderate temperatures over a short period of time was adopted to prepare α-Mg formate. A follow-up activation process is performed at relatively high temperature, which would remove the leftover solvent molecules present in the pores thereafter exposing the channels. The structure of activated α-Mg-formate is shown in Figure 2.1.

In the activated structure of α-Mg formate, two types of chemically independent oxygen η^1 and η^2 are present,[8] which correspond to the oxygen atoms that bound to one or two Mg sites.

Four distinct types of Mg are found in the structure, and each Mg site is octahedrally coordinated by six oxygen atoms. The four types of Mg sites can be differentiated by the number and types of oxygen they are connected to. Mg1 is bound with six η^2 oxygen; Mg2 and Mg4 are both connected with two η^2 oxygen and four η^1 oxygen; Mg3 is connected with four η^2 oxygen and two η^1 oxygen. As shown in Figure 2.1 b.

To form 3D porous structure, Mg1-O$_6$ and Mg3-O$_6$ octahedra are connected in an edge-shared fashion, forming zigzag chains. The parallel zigzag chains are interconnected by Mg2-O$_6$ and Mg4-O$_6$ octahedra in a vertex-shared fashion, creating 1D channels down crystallographic b axis with channel size of 4.5 Å × 5.5 Å.

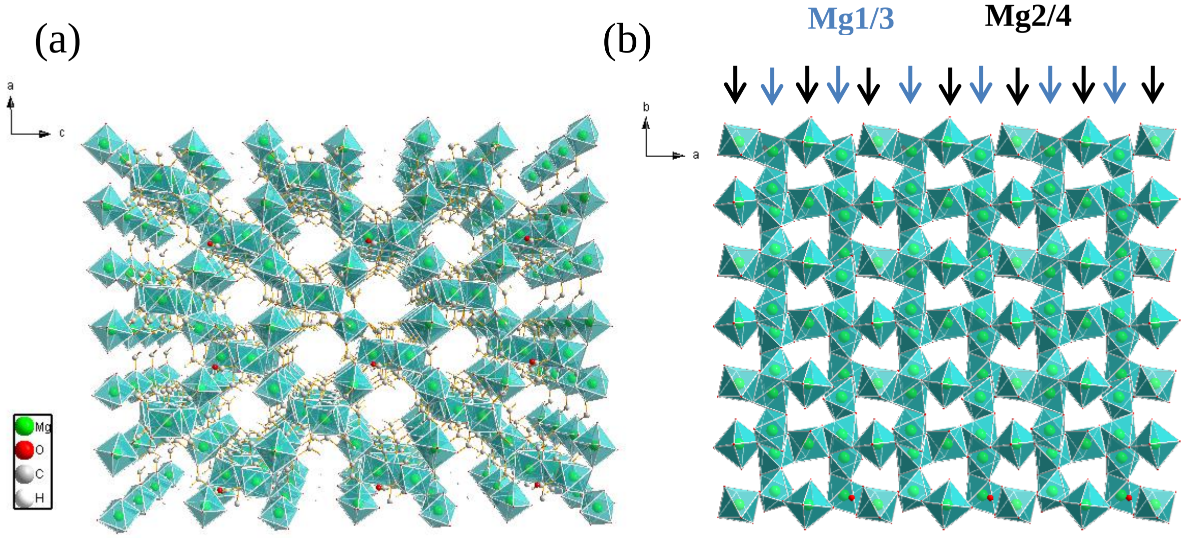

Figure 2.1 - Mg formate 3D structure viewed down crystallographic b axis (a) and 2D structure viewed down c axis (b). Blue arrows indicate the zigzag chains formed by Mg1O and Mg3O octahedra; black arrows indicate Mg2O or Mg4O octahedra that bridge two zigzag chains. For clarity, oxygen and hydrogen atoms are omitted in (b).

Unlike MOFs that possess unsaturated metal sites exposing to the channels, which usually exhibit exceptional uptake of guest molecules,[9] α-Mg formate MOF does not possess any unsaturated metal sites or S- or N- containing functional groups that serve as strong electron acceptor.[10] Therefore, no strong electronic donor-acceptor interaction could take place during guest-host interaction. The Mg sites in α-Mg formate are fully coordinated to six oxygen atoms and hidden at the centre of Mg-O octahedra and are inaccessible to guest species. On the other hand, the 3D structure in Figure 2.1 shows that the hydrogen atoms from the formate anions are pointing toward the 1D channels, which have direct access to guest species. Therefore, it is reasonable to examine the possibility of hydrogen atoms along the interior of the framework to be the adsorption sites in this type of MOF.

Only a few studies have demonstrated the guest-host interaction of α-Mg formate due to its relatively small pore size compared to other types of MOFs.[11] In Kimoom Kim's work,[6] α-Mg formate shows exceptional selectivity of C_2H_2 over other guest molecules including CO_2, H_2, N_2, O_2 and CH_4, which results from the strong van der Waals interaction between the hydrogen atoms from C_2H_2 and oxygen atoms from the framework wall. In addition, the single crystal structure of the C_2H_2 adsorbed MOF reported by this work shows two independent positions of C_2H_2 in the zigzag channels. Our group has also done some research regarding α-Mg formate. In one of our recent works,[12] a pressure induced irreversible phase change was observed in α-Mg formate based on Raman results. When guest molecules such as DMF and benzene are loaded into the framework, no such phase transition was observed. Another work of our group successfully resolved the adsorption sites of pyridine, benzene and DMF adsorbed in α-Mg formate by means of ^{1}H MAS as well as the dynamics of the guest molecules by ^{2}H SSNMR, which have provided strong structural evidence with regards to this guest-host system when single crystal data is not available.[13] To the best of our knowledge, only one publication so far has shown the CO_2 uptake of α-Mg formate. R. Banerjee's study shows the CO_2 uptake at one bar of α-Mg formate is 70 cm^3/g.[3] No previous studies have been conducted on the adsorption mechanisms of guest molecules in this type of MOF. As a result, the adsorption sites and CO_2 dynamics in this type of MOF remain elusive.

SSNMR has been widely used to study guest-host interactions in MOFs due to its sensitivity to molecular dynamics.[14-18] Under different thermal conditions, CO_2 molecules undergo different types of motion, resulting in very different NMR line shape. A previous study shows that the nearly stationary CO_2 molecules at 20 K would give rise to a broad axially symmetric powder pattern with $\delta_{11} = \delta_{22} = 245$ ppm, $\delta_{33} = -90$ ppm, and $\delta_{iso} = 132$ ppm,[19] as shown in Figure 2.2a (bottom). As for completely mobile CO_2, the NMR spectrum is a single sharp peak with an isotropic chemical shift of 125 ppm, resulting from the averaged NMR interactions due to fast molecular tumbling, as shown in Figure 2.2a (top). In some special cases such as CO_2 being trapped in porous materials, the movement of CO_2 molecules is limited due to its interaction with the interior of the frameworks. Under such circumstances, the observed NMR line shape lies between the two extreme conditions, as shown in Figure 2.2a (middle). The shape and width of CSA powder pattern depend on the rate and type of motion of CO_2 molecules. As a result, the NMR line shapes are not necessarily axial symmetric any more. Therefore, it is very interesting to study CO_2 molecules throughout a wide temperature range, which would provide more insight about the adsorption behavior in this specific type of MOF.

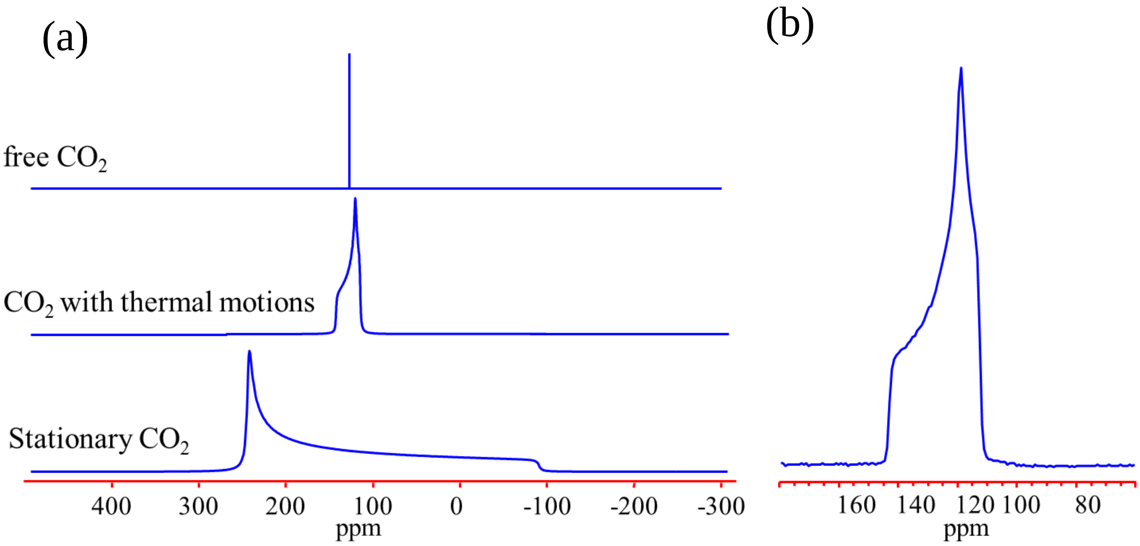

Figure 2.2 - ^{13}C spectra of mobile CO_2 (a top); CO_2 with certain motions (a middle); completely stationary CO_2 (a bottom). Enlarged ^{13}C spectrum of CO_2 with certain motions (b).

Simulation software packages such as NMR-WEBLAB and EXPRESS are able to predict the effect of motions on NMR active nuclei.[20,21] Certain motions upon the principal axis system would give rise to distinct NMR line shapes. In this work, EXPRESS simulation is used to predict the molecular motion of CO_2 loaded α-Mg formate.

2.2 Experimental

2.2.1 Synthesis

α-$Mg_3(HCOO)_6$ was synthesized on a simple solvothermal procedure reported elsewhere previously.[4] 0.77 g $Mg(NO_3)_2\cdot 6H_2O$ (Sigma-Aldrich, 99%) was dissolved in a mixed solution contained 10 ml N,N dimethylformamide (DMF) and 0.23 ml formic acid (Alfa Aesar, 97%) in a 23 ml Teflon inlet. The Teflon inlet was then dropped into an autoclave, sealed and placed in the oven under 110 °C for 72 hours. The white powdery product was washed repeatedly with DMF and recovered by vacuum filtration, marked as the “as-made” sample. In order to remove the solvent molecules in the pores as much as possible and expose the channels, the as-made sample was placed on a watching glass and activated in an oven under 150 °C for 24 hours, denoted as the activated sample.

2.2.2 Gas adsorption

A gas adsorption apparatus consisting of a home-built Schlenk line (total volume of 82.7 mL) attached to a vacuum pump and a pressure gauge was used to further activate the sample and monitor the gas adsorption process. First, approximately 0.13 - 0.15 g activated α-$Mg_3(HCOO)_6$ was packed into the horizontal bottom of a 5 mm L-shaped glass tube (to fit the 5 mm SSNMR coil). A small amount of glass fiber was then stuffed tightly on top of the powder sample to prevent spatter under vacuum conditions. Subsequently, the glass tube was attached to the

Schlenk line and kept under vacuum condition for 5 hours under 150 ℃ as further sample activation. A round bottom flask containing pressurized $^{13}CO_2$ was also attached to the apparatus after the activation process, and a known amount of gas was released into the Schlenk line. In this study, an adsorption amount of 0.1 CO_2/Mg was chosen. The loading amount was represented by molar ratio between CO_2 and Mg. Since the amount of sample in the L-shape tube is known, the amount of gas required can be calculated into pressure by ideal gas law, which can be directly observed from the pressure gauge. The L-shape tube was then immersed into liquid nitrogen and the gas in Schlenk line was adsorbed into the MOF sample. After this step, the L-shape tube was flame-sealed and kept in a glass vial for further NMR use.

2.2.3 Powder X-ray diffraction

Powder X-ray diffraction (pXRD) was used to determine the composition of the product. In this study, pXRD data was collected by a Rigaku diffractometer using Co Kα radiation (λ=1.7902). All samples were scanned between 5°- 45 ° at a scan rate of 10 ° per min, with a 0.02 ° increment.

2.2.4 SSNMR characterization

SSNMR experiments were carried out by a Varian infinity plus 400 spectrometer (magnetic field 9.4 T). An attached temperature control unit was used to adjust temperature within the theoretical range of 123 K to 423 K. The Depth spectrum was collected using double channel 5 mm static probe from 173 K to 393 K with a 20 ℃ increment. In order to achieve thermal equilibrium of the whole system, there was 20 minutes elapsed time between each two acquisitions. The optimized 90 ° pulse length and pulse delay for ^{13}C was 2.25 μs and 6 s, and the acquisition number was 256. For static CP experiments, a contact time array of 0.5 ms, 3 ms, 6 ms, 8 ms and 10 ms were carried out at 173 K, 293 K for both the $^{13}CO_2$ adsorbed and activated α-Mg formate to determine the adsorption sites. All spectra were referenced to methylene carbon of CH_3CH_2OH at 56.83 ppm from Tetramethylsilane (TMS), which has $\delta_{iso} = 0$. NUTs software was used to process NMR raw data such as Fourier transformation (FT), phase correction, and line broadening.[22] WSolids and dmfit software packages were used to extract NMR parameters such as δ_{iso}, Ω and κ that define NMR line shapes.[23,24] A successful simulation was accepted when no visible difference between the experimental spectra and the simulated ones can be observed. EXPRESS simulation package based in Matlab platform accounted for the interpretation of molecular motions of CO_2 in the framework based on the fact that different motions produce distinct NMR line shape.[21] The adopted principal axis system (PAS) of the stationary CO_2 during EXPRESS simulation are: δ_{iso} = 125 ppm, Ω = 335 ppm and κ = 1.[19] The motions are abbreviated as C_n, which stands for either n fold rotation upon an adsorption site or n fold hopping between sites. The rate of all motions is considered in a fast regime, which is 5×10^8 Hz. Visual comparison between the simulated spectra and experimental ones determines whether it is a successful simulation or not.

2.3 Results and discussion

The pXRD patterns of as-made and activated α-Mg formate are shown in Figure S2.1. Both are in good agreement with the simulated ones obtained from literature reported structures.[4]

Figure 2.3 shows the result of ^{13}C VT experiments of the CO_2 loaded α-Mg formate sample. It is worth mentioning that the spectra shown here are solely contributed by the adsorbed CO_2 molecules, not from the MOF itself since only CO_2 is ^{13}C enriched, not the framework carbon atoms.

At 173 K, the NMR spectrum is a broad powder pattern. As temperature increases up to 313 K, the spectrum gradually gets narrower. In addition, the NMR line shape undergoes a continuous “flip”, which means that δ_{22} of the powder pattern progressively moves to the more shielded side as temperature increases. This change in NMR line shape is a result of the change in molecular motion of CO_2 under different thermal conditions. From 313 K, a second resonance near 125 ppm starts emerging, which is ascribed to free CO_2 signal. As temperature keeps increasing to 393 K, this resonance has become more and more evident, indicating more mobile CO_2 molecules present in the system. Interestingly, a third resonance at 145 ppm becomes more significant during the heating process, and the NMR line width is abnormally broadened at 393 K.

Due to the distinct NMR behavior at temperature below and above room temperature, low temperature results (LT, 173 K- 293 K) and high temperature results (HT, 293 K- 393 K) will be discussed separately in this chapter.

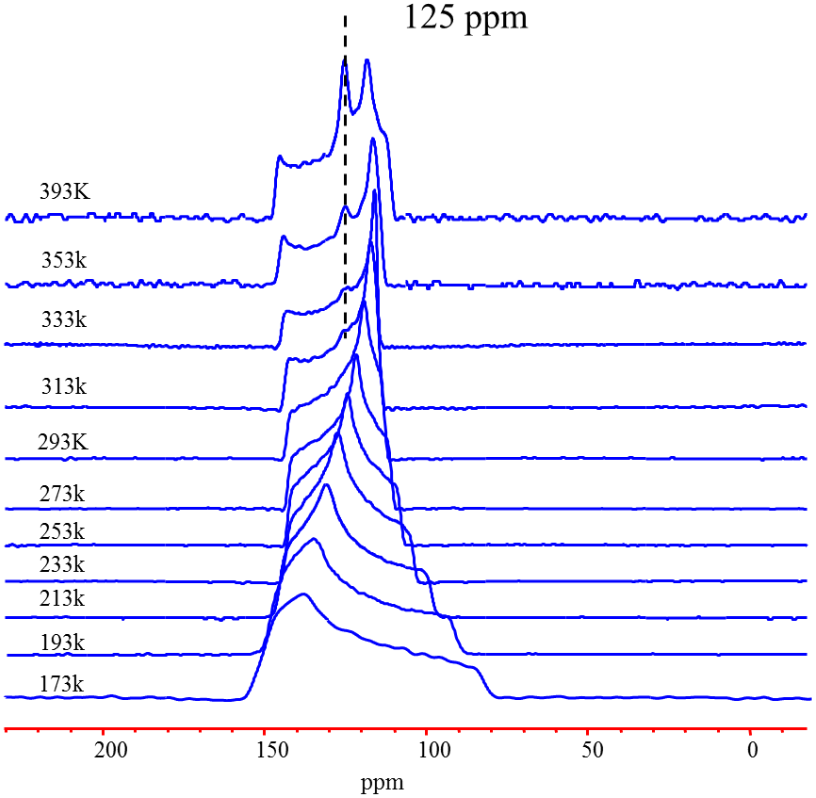

Figure 2.3 - ^{13}C VT spectra of $^{13}CO_2$ adsorbed α-Mg formate from 173 K to 393 K.

2.3.1 Low temperature experiment

Before studying the CO_2 loaded MOF, it is important to verify the degree of activation and the structural stability of α-Mg formate within the experimental temperature range. Therefore, CP static experiments with the use of a contact time array of activated α-Mg formate were conducted at both 173 K and 293 K. If there were DMF molecules not completely removed by the activation process, or a change in local environment occurs, severe difference would be observed between short contact time CP spectra and long contact time ones. The results are shown in Figure 2.4.

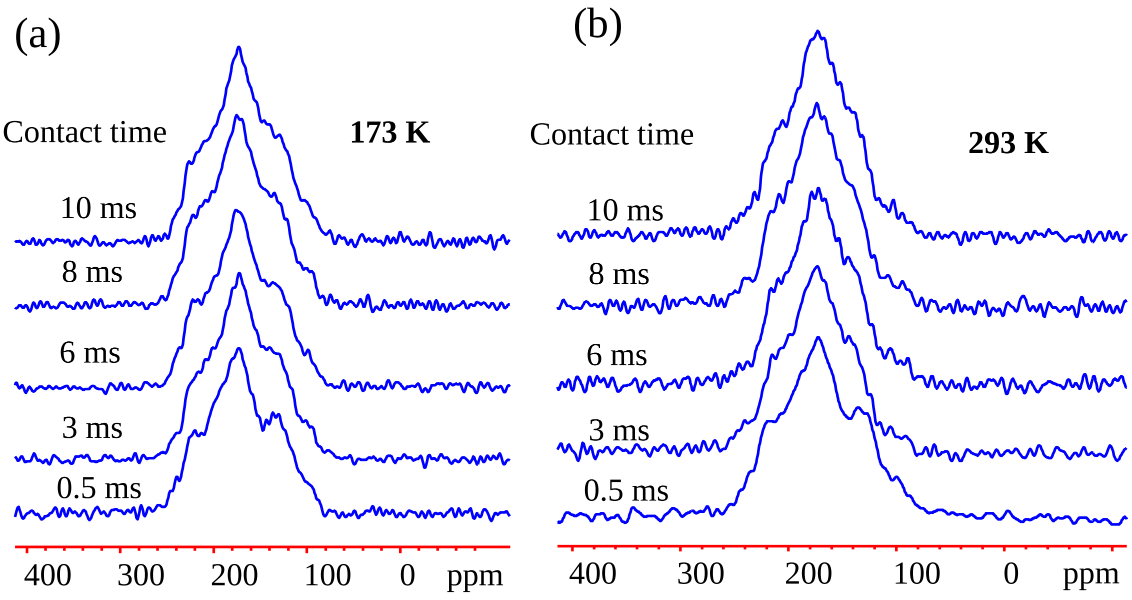

Figure 2.4 - ^{13}C CP spectra of the activated α-Mg formate with the use of different contact time at 173 K (a) and 293 K (b).

The “volcano” shape spectra of the activated α-Mg formate are the results of overlapping signals from six crystallographically non-equivalent carbon atoms from the framework, which have already been resolved in previous work of our group.[13] No severe change is observed between the spectra acquired at 173 K and 293 K with the use of the same contact time, indicating the good structural stability of this type of MOF within this temperature range. In addition, CP spectra remain constant upon the use of contact time from 0.5 ms to 10 ms at both temperatures, indicating a complete activation of the framework. No leftover solvent molecules can be detected in the system.

Figure 2.5 shows the LT static spectra of CO_2 loaded in α-Mg formate and the simulated NMR spectra using dmfit software from 173 K to 293 K. The derived CSA parameters are summarized in Table 2.1.

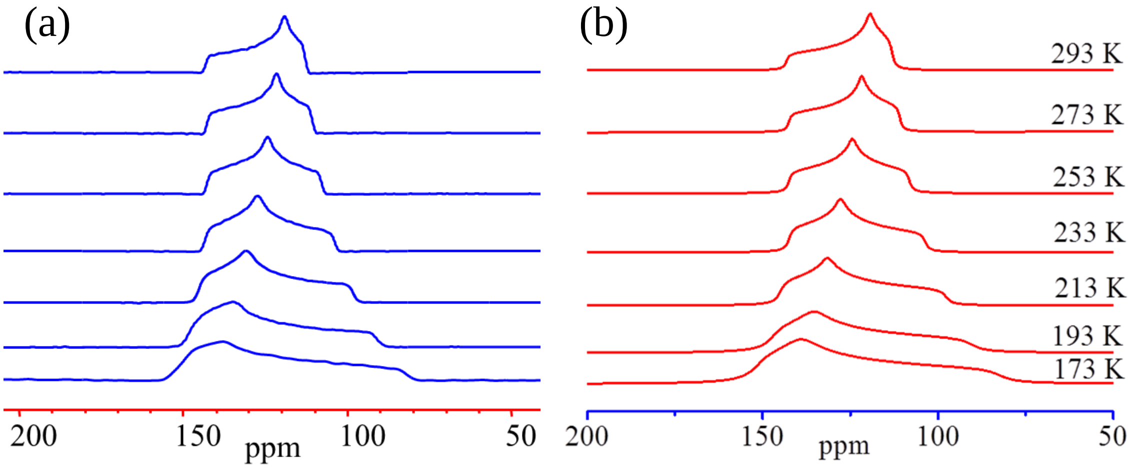

Figure 2.5 - ^{13}C LT experimental (a) and simulated spectra (b) of $^{13}CO_2$ loaded in α-Mg formate.

In this temperature range, δ_{iso} remains constant at 125 ppm. As mentioned in chapter 1, Ω reflects the width of NMR spectrum. The broadest spectrum observed in this work was at 173 K, with Ω value of 69 ppm. The discrepancy between the literature value of Ω for stationary CO_2 in solid form (335 ppm at 20 K) and our experimental result suggests that the molecular motion of CO_2 is restricted,[19] but far from stationary in this temperature range. As temperature increases, the decrease of Ω suggests that CO_2 molecules experience higher degree of motional freedom. The continuous change of κ from positive to negative values result from the gradual flip of δ_{22} from the more shielded to less shielded side. Originally at 173 K, δ_{22} is at 138 ppm. As the temperature increases to 293 K, δ_{22} has shifted to 116 ppm. This interesting phenomenon is associated with the significant difference in CO_2 molecular motions, which will be discussed later in this chapter.

Table 2-1 Derived CS parameters for LT spectra of $^{13}CO_2$ loaded in α-Mg formate**.**

	173 K	**193 K**	**213 K**	**233 K**	**253 K**	**273 K**	**293 K**
δ_{iso} (ppm)	125(1)	125(1)	125(1)	125(1)	125(1)	125(1)	125(1)
Ω (ppm)	69(1)	57(1)	47(1)	39(1)	34(1)	32(1)	30(1)
κ	0.64(1)	0.58(1)	0.43(1)	0.24(1)	-0.05(1)	-0.31(1)	-0.58(1)

In the structure of α-Mg formate, three types of hydrogen atoms are pointing towards the channels and have direct access to guest species (H1, H5 and H6), which make them the possible adsorption sites during guest-host interactions. Therefore, CP experiments employed a contact time array from 0.5 ms to 10 ms were conducted upon CO_2 loaded α-Mg formate to study the spatial connectivity between framework hydrogen atoms and carbon atoms. As mentioned in Chapter 1, CP is mediated by the ^{1}H-^{13}C dipolar interaction, which is strongly dependent on the inter-nuclear distance. Only the carbon atoms close enough to protons will give rise to significant resonance.[25] The use of longer contact time allows the detection of ^{13}C nuclei far from ^{1}H. When shorter contact times are employed, only ^{13}C nuclei in close proximity to ^{1}H are detected.

The static spectra of CO_2 loaded α-Mg formate along with the CP spectra of activated α-Mg formate are stacked for comparison purposes. From the results summarized in Figure 2.6, the spectra obtained with a contact time of 0.5 ms at both 173 K and 293 K show almost identical NMR line shapes to those of empty frameworks. When longer contact time was employed at both temperatures, an additional resonance at more shielded direction becomes more and more significant. This resonance in the 10 ms contact time spectrum shows an almost identical line shape with the overlaid $^{13}CO_2$ spectrum, indicating it results from the adsorbed CO_2 molecules. Since the carbon atoms in CO_2 molecules are further from the hydrogen atoms than the carboxylic carbon atoms, the adsorbed CO_2 signal cannot be observed in spectrum that employed a short contact time of 0.5 ms, resulting in the similarity between the CP spectra of CO_2 adsorbed and activated α-Mg formate. With increasing contact time, the resonance associated with CO_2 gradually emerges from the "volcano-shape" resonance from the activated framework, suggesting the weak dipolar coupling between the hydrogen atoms from the framework and carbon atoms from CO_2 molecules is successfully detected by the use of longer contact time.

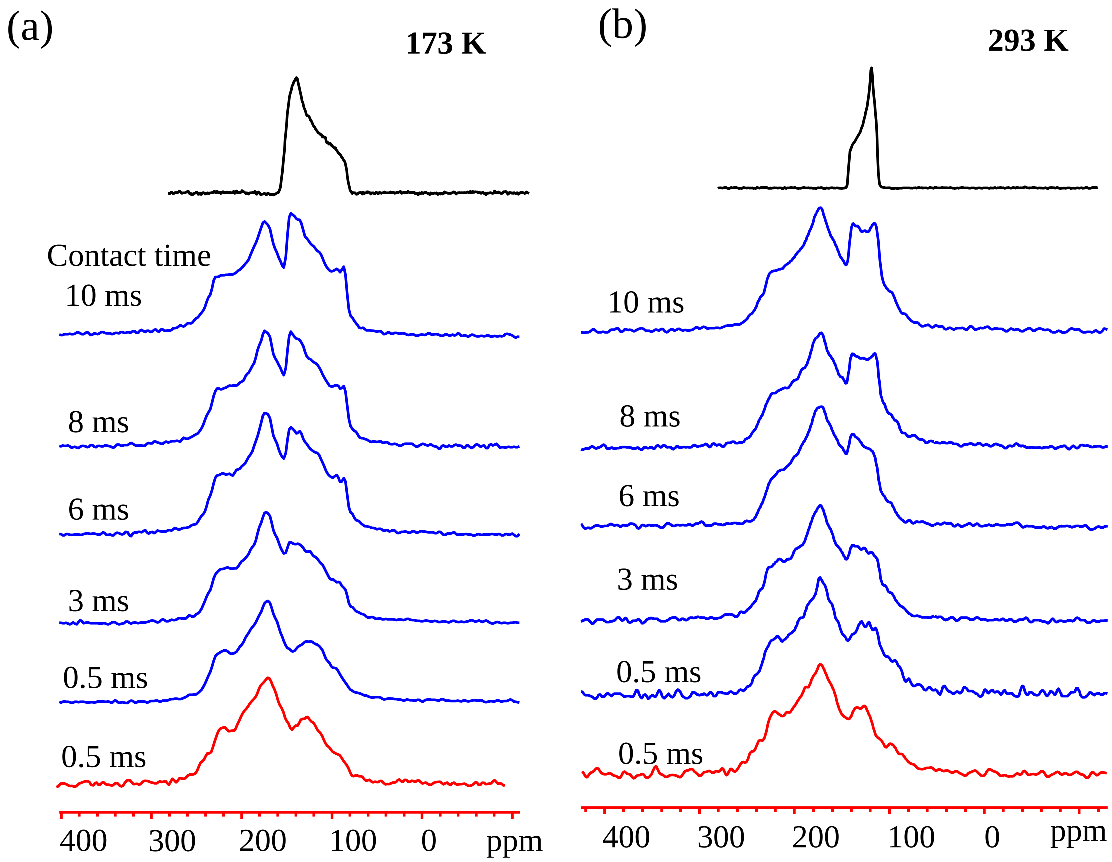

Figure 2.6 – ^{13}C CP spectra obtained at 173 K (a) and 293 K (b) with different contact times. Red and blue spectra are the CP spectra of activated α-Mg formate and CO_2 loaded α-Mg fromate. Black spectra are ^{13}C VT spectra of $^{13}CO_2$ loaded MOF obtained at 173 K and 293 K, same with the ones shown in Figure 2.3.

These results have confirmed that ^{13}C from guest molecules are able to be detected through CP experiments with the use of long contact time, indicating CO_2 molecules are within close proximity to hydrogen atoms from the frameworks. Therefore, we can conclude that CP results have successfully confirmed the hypothesis that hydrogen atoms are the adsorption sites.

Dynamic analysis of the adsorbed CO_2 molecules using EXPRESS simulation

After confirming the adsorption site to be hydrogen, the next step is to properly explain the interesting change in NMR line shapes and provide insight regarding the motions that CO_2 molecules possess at each temperature. EXPRESS simulation was carried out to fulfill this task.[21] Similar to a previous study,[16] a combined motion of a localized rotation of CO_2 molecules upon one hydrogen site, which can be modulated by a six-fold (C_6) rotation in EXPRESS simulation, and a simultaneous non-localized twofold (C_2) inter-sites hopping between two hydrogen sites is predicted. Based on this proposed model, the simulated spectra show closest resemblance to the experimental ones compared to other models, shown in Figure 2.8a and b. The combined motion is characterized by rotation angle θ and inter-sites hopping angle γ, and the rate of two motions remain at the fast limit throughout the whole temperature range, which is 5×10^8 Hz. θ represents the angle between the localized rotation axis and the longitudinal axis of CO_2 molecule; γ is the angle between the rotation axis and the non-localized hopping axis. The EXPRESS derived θ and γ are summarized in Table 2.2, and the scheme of the combined motion is depicted in Figure 2.7. Previous reports about CO_2 adsorption in MOFs have depicted an end-on adsorption upon the adsorption site.[14,26] Therefore, the localized rotation of CO_2 molecules in this study is also assumed to occur upon hydrogen sites in an end-on way, and rotate in a cone-shape fashion.

The values of θ and γ derived from EXPRESS simulation suggest that both θ and γ become greater as temperature increases, and the change of γ is more severe in comparison to the relatively smaller variation of θ, indicating temperature affects the hopping motion more substantially than the uniaxial rotation motion. From 173 K to 293 K, γ experiences a drastic change from 23 ° to 42 °, whereas θ only changes from 45 ° to 49 °, indicating that at higher temperature during LT experiments, the localized rotation of CO_2 molecules upon hydrogen sites takes place in a slightly larger cone, and the inter-sites hopping occurs between two hydrogen sites more distant from each other.

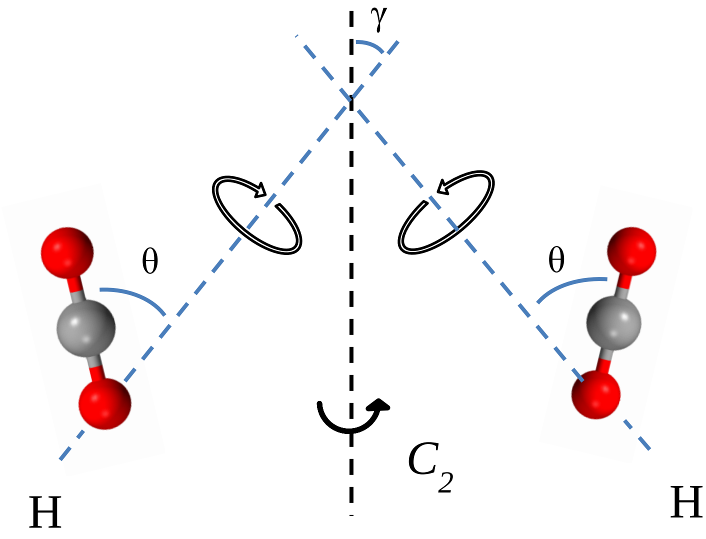

Figure 2.7 - Schematic of localized rotation of CO_2 molecule upon hydrogen and simultaneous two sites hopping between two hydrogen sites.

Table 2-2 EXPRESS simulation derived localized rotation angle θ and non-localized hopping angle γ of $^{13}CO_2$ loaded in α-Mg formate at LT.

	173 K	**193 K**	**213 K**	**233 K**	**253 K**	**273 K**	**293 K**
θ (°)	45(0.5)	47(0.5)	48(0.5)	48.5(0.5)	49(0.5)	49(0.5)	49(0.5)
γ (°)	23(1)	23(1)	27(1)	32(1)	36(1)	39(1)	42(1)

EXPRESS simulation using a single motion of C_6 localized rotation or a C_2 inter-sites hopping were also conducted to verify the validity of the combined motion. The results are shown in Figure 2.8 c and d.

It is clear that the ones using only C_6 localized rotation or C_2 inter-sites hopping deviate from the experimental spectra significantly, which has further confirmed the reliability of the $C_6 + C_2$ combined motion for the CO_2 loaded α-Mg formate.

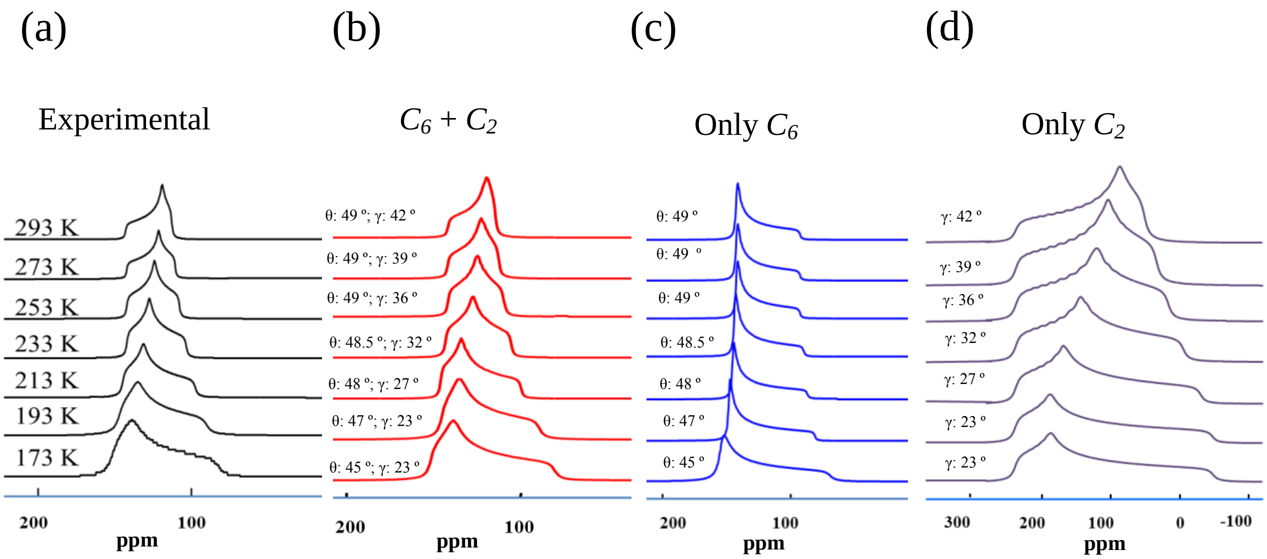

Figure 2.8 - LT experimental ^{13}C spectra of $^{13}CO_2$ loaded α-Mg formate (a); EXPRESS simulations using the combined motion (b), only C_6 localized rotation (c) and only C_2 inter-sites hopping (d) of $^{13}CO_2$.

2.3.2 High temperature experiment

The HT experiment demonstrates distinct results from the LT ones. Above 313 K, more than one powder pattern can be derived from the experimental spectra, indicating multiple non-equivalent adsorption sites take place at higher temperature instead of the single one during LT experiments. For the sake of clarity, the deconvolution of spectrum obtained under 393 K using dmfit software is enlarged in Figure 2.9, and the deconvolution of spectra obtained at other temperatures during HT experiment are included in Figure 2.10 a.

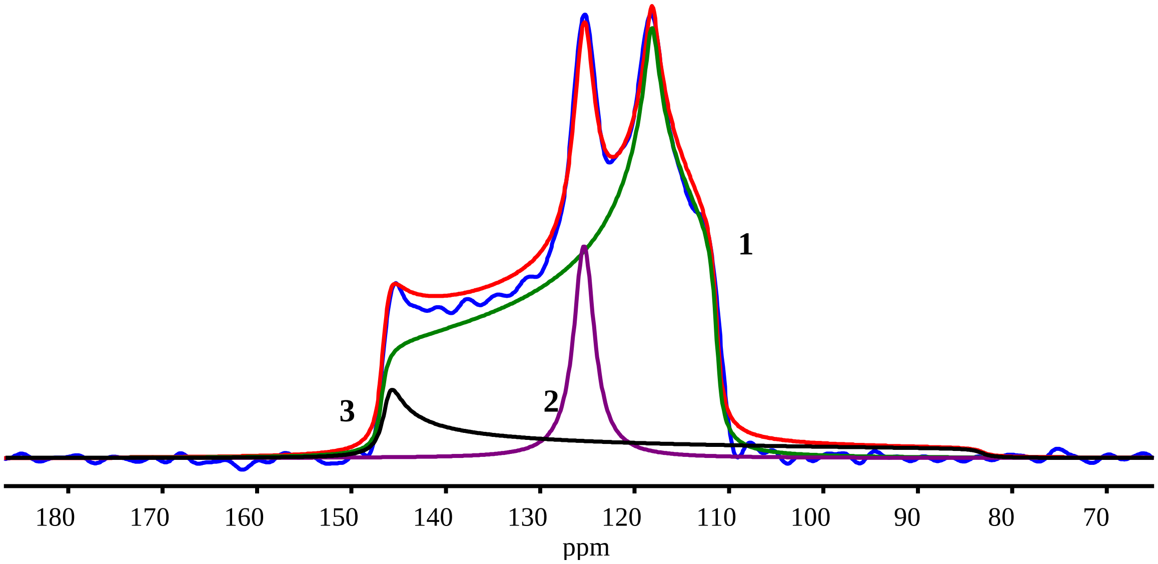

Figure 2.9 - Three-sites deconvolution of ^{13}C VT spectrum of $^{13}CO_2$ loaded α-Mg formate obtained at 393 K. The color code is shown as following: Site 1 - green; Site 2 - purple; Site 3 - black; Summation of the three-site simulation - red; Experimental - blue.

From the deconvoluted spectrum, it is clear that the powder pattern resulting from the CO_2 molecules possessing the combined motion has changed continuously between 173 K and 393 K. This site is denoted as site 1. Since the LT behavior of this site has already been discussed during LT experiment section, only the high temperature behavior of this site will be discussed in this section. The derived spectra of site 1 at each temperature are shown in Figure 2.10 a.

In addition to site 1, the signal emerging near 125 ppm from 313 K is ascribed to free CO_2 molecules (denoted as site 2). As temperature increases, site 2 becomes more and more significant, suggesting more CO_2 molecules become free from the adsorption sites at higher temperatures. A third resonance (denoted as site 3) on the less shielded side appears when the temperature reaches 333 K in addition to site 1 and 2. This resonance continuously gets more intense as temperature increases. The weight percentage of each site at each temperature is shown in Table 2.3. In this section, the three sites will be analyzed and discussed separately.

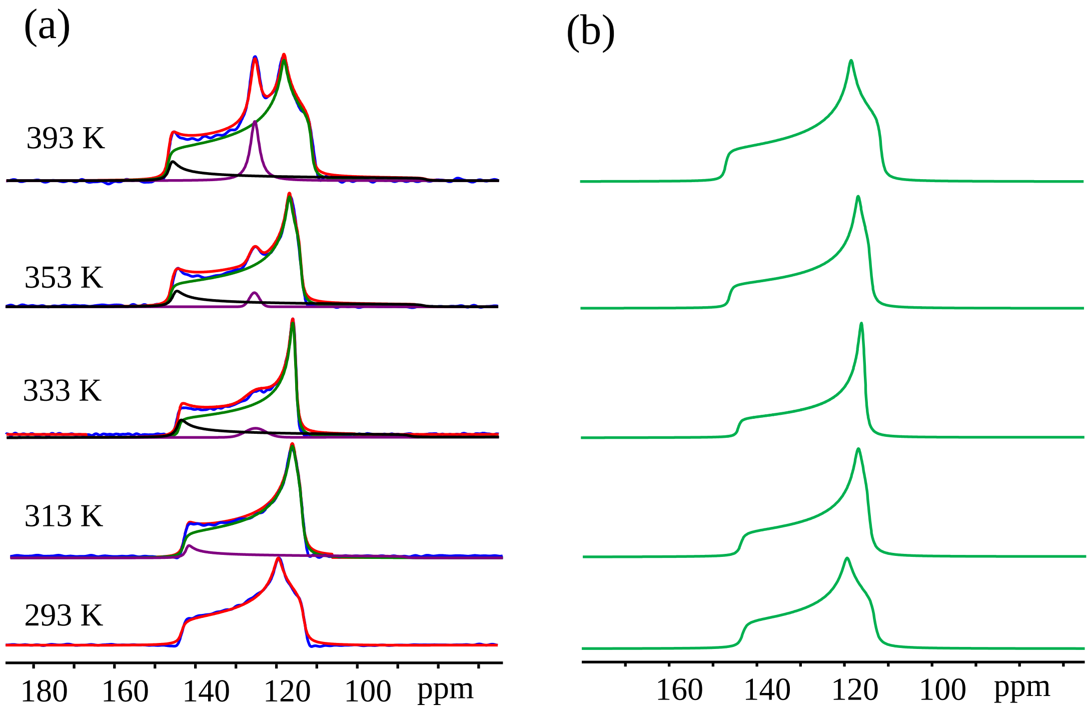

Figure 2.10 Three-sites deconvolution of HT ^{13}C spectra of $^{13}CO_2$ loaded in α-Mg formate(a) and derived site 1 spectra (b). Color cold is the same with Figure 2.9.

Table 2-3 Weight analysis of site 1, 2 and 3 in ^{13}C HT spectra of $^{13}CO_2$ loaded α-Mg formate

	313 K	**333 K**	**353 K**	**393 K**
Site 1 %	94(1)	91(1)	88(1)	85(1)
Site 2 %	-	2(1)	3(1)	8(1)
Site 3 %	6(1)	7(1)	9(1)	7(1)

Throughout the whole HT experiments, site 1 is the dominant composition in each spectrum. Due to the emergence of site 2 and 3, the population of site 1 decreases as temperature increases. Site 2 does not appear until 333 K and it keeps getting more significant. Site 3 gets larger until

353 K and experiences a bit decrease from 353 K to 393 K.

The derived CS parameters of site 1 during HT experiments are shown in Table 2-4. δ_{iso} remains constant at 125 ppm from 293 K to 393 K, which is consistent with the LT experiment result. The derived Ω values have confirmed the broadening of NMR line shape at higher temperature. The values of κ also show similar result, which keep decreasing from -0.83 to almost -1 at 333 K and then increasing back to -0.61 at 393 K. These results suggest that the mobility of CO_2 molecules is slightly more restricted at temperatures above 333 K than they are at room temperature.

Table 2-4 CS parameters of site 1 evolved from HT experiments

	313 K	**333 K**	**353 K**	**393 K**
δ_{iso}	125(1)	125(1)	125(1)	125(1)
Ω	29(1)	29(1)	32(1)	35(1)
κ	-0.83(1)	-0.95(1)	-0.82(1)	-0.61(1)

Similar results are also found for site 3. The derived CS parameters for site 3 are summarized in Table 2-5. δ_{iso} remains at 125 ppm, confirming site 3 results from the adsorbed CO_2 molecules. The value of **Ω** becomes greater as temperature increases, indicating a similar broadening trend that is also observed in site 1. It is worth mentioning that the **Ω** values for site 3 are almost two times greater than site 1, suggesting the degree of CO_2 mobility associated with site 3 is significantly less mobile than that of site 1. The value of κ remains constant at 1, resulting in an axially symmetric powder pattern for all HT results of site 3.

Table 2-5 CS parameters of site 3 during HT experiments

Site 3	**313 K**	**333 K**	**353 K**	**393 K**
δ_{iso} (ppm)	125(1)	125(1)	125(1)	125(1)
Ω (ppm)	54(1)	59(1)	62(1)	63(1)
κ	1.00(1)	1.00 (1)	1.00(1)	1.00(1)

To sum up the analysis on CSA parameters for site 1 and 3, the line widths of both sites get abnormally broad at higher temperatures. These results are contradictory to common knowledge that at higher temperature, gas molecules possess a higher degree of mobility, leading to significantly narrower NMR line shape. In addition, the population analysis shows that site 3 is a very small composition in HT spectra. We cannot rule out the possibility that experimental errors are responsible for this additional resonance and the abnormal line broadening at high temperature. Therefore, verifying the validity of the three sites deconvolution is necessary.

Verifying the validity of three sites spectrum

A series of examinations were conducted to examine this issue. Firstly, we suspected there was a problem with the pulse sequence we use. The use of depth sequence would sometimes cause the missing of the first few points in FID containing important information if the decay occurs too rapidly. As a result, NMR line shape distortion is sometime discovered along the use of depth pulse sequence. Therefore, echo pulse was employed to test the exact same sample due to its advantage of dealing with samples during rapid relaxation, and the results are shown in Figure 2.12.

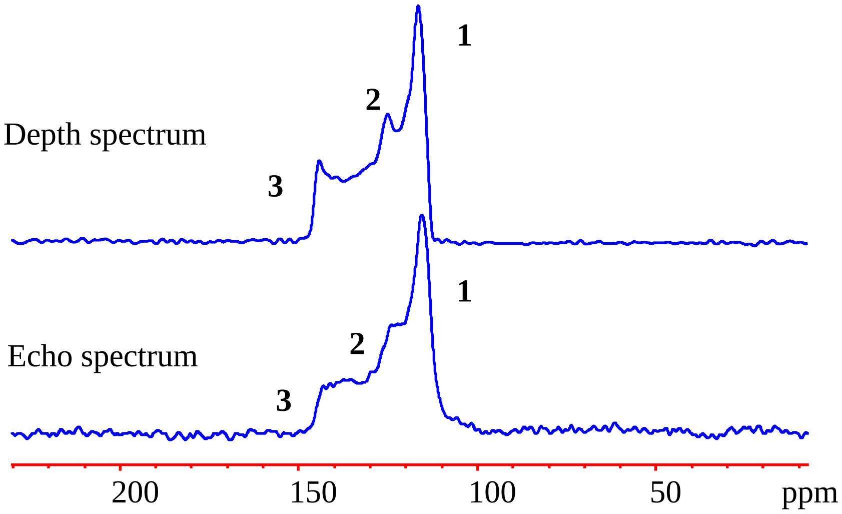

Figure 2.11 - Comparison between ^{13}C depth and echo spectrum of $^{13}CO_2$ adsorbed in α-Mg formate obtained at 353 K.

Even though the NMR spectrum obtained by echo sequence is slight different than the depth one, which is due to the line broadening added to the spectrum because of the poor signal to noise ratio coming along this pulse sequence, three distinct sites right around the same frequencies are still clearly detectable. These results have confirmed the reliability of three sites deconvolution based on the experimental spectra. Hence, the influence of pulse sequence is ruled out in this case.

Secondly, we considered the possibility that α-Mg formate might undergo short term decomposition under high temperature, causing abnormal NMR line shape. Hence, we repeated the acquisition at room temperature after the sample was completely cooled down from HT experiments. The results are shown in Figure 2.12.

The results shown in Figure 2.12 confirm that the spectra acquired before and after the HT experiments are identical. Therefore, no irreversible change of the framework should have occurred during the heating process.

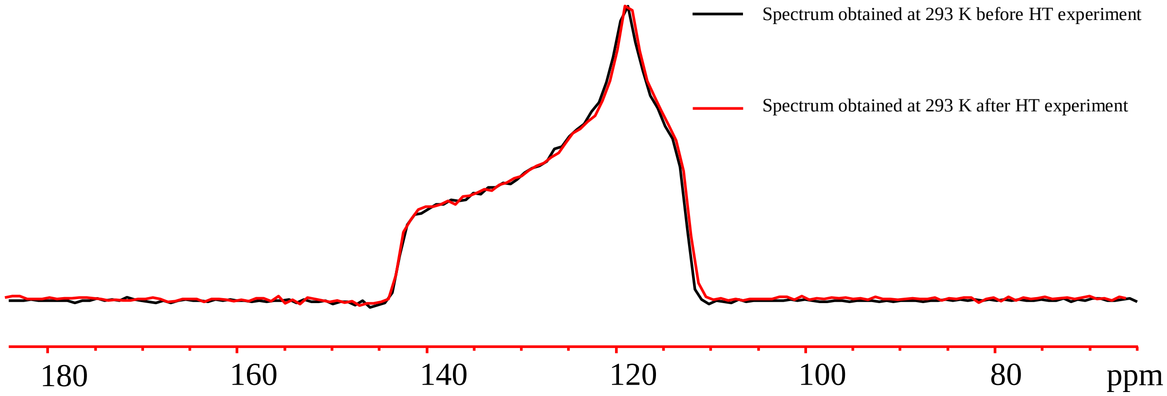

Figure 2.12 – ^{13}C spectrum obtained at 293 K of CO_2 adsorbed α-Mg formate before and after HT experiments.

CP experiments were also conducted upon the activated α-Mg formate at 353 K in order to examine the possibility of a reversible structural change. The results are shown in Figure 2.13. The CP spectra of activated α-Mg formate collected at 173 K and 293 K are stacked in Figure 2.14b (bottom) for comparison purposes. It is clear that the CP spectra obtained at 173 K and 293 K are identical, indicating no change in structure occurred in this temperature range, as already discussed in LT experiments section. However, the CP spectrum obtained at 353 K shows slight difference in comparison with the 293 K one: The strongest resonance near 173 ppm has shown a flat top; the left side of the volcano-shape spectrum at 226 ppm shifts to lower frequency side; the right side of the volcano-shape spectrum moves to the higher frequency side. The observed difference might have been the result of a subtle structural change taking place at high temperature.

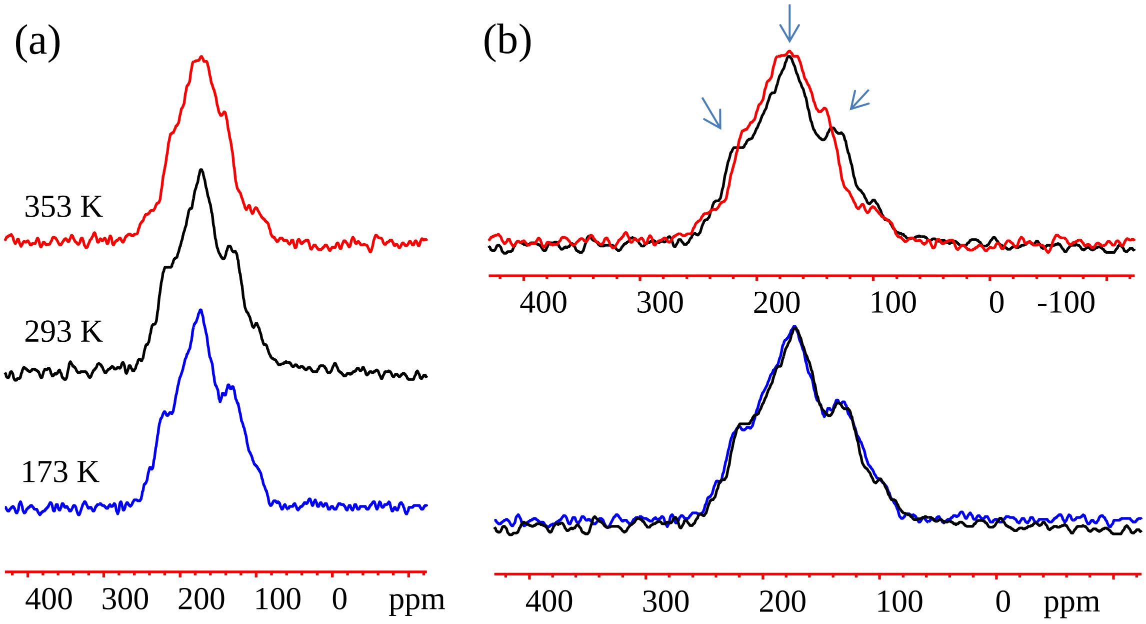

Figure 2.13 - ^{13}C CP static spectra of the activated α-Mg formate obtained with 0.5 ms CT at three temperatures (a). Blue, black and red spectra are obtained at 173 K, 293 K and 353 K. Overlaid spectra of different temperatures are also present in (b) and (c) for comparison.

Unfortunately, no previous reports have demonstrated a phase change occurring at higher temperature in this type of MOF, or any of its analogues. Accordingly, further work such as single crystal XRD would be performed as a complementary examination to confirm the structural change at high temperature for α-Mg formate.

Based on the results obtained so far, we rule out the likelihood of experimental errors, and assume that the line broadening of site 1 and the emergence of site 3 during HT experiment is the result of subtle structural change of α-Mg formate MOF at high temperature, and this change is reversible.

Dynamic analysis of adsorbed CO_2 molecules using EXPRESS simulation

EXPRESS simulation was conducted to provide insights for motional change of CO_2 molecules during HT experiments. Site 1, as with LT experiments, results from a combined motion consisting of a localized rotation, which can be modeled by a C_6 exchange, and a simultaneous twofold inter-sites hopping, shown in Figure 2.14a and b. The simulated uniaxial rotation angle θ and inter-site hopping angle γ are summarized in Table 2.6. The EXPRESS simulations using only C_6 or C_2 motion were also performed, and the results deviate from experimental spectra greatly, as shown in Figure 2. 14c and d.

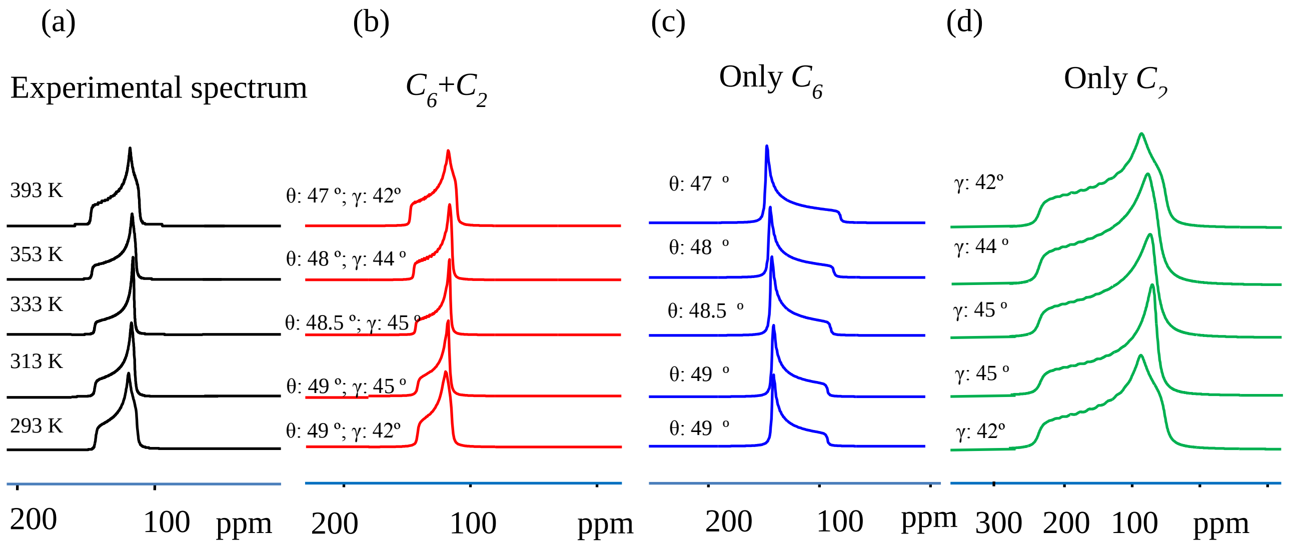

Figure 2.14 - LT experimental spectra (a), EXPRESS simulation using the combined motion modeled by C_6 localized rotation and C_2 inter-sites hopping (b), only C_6 localized rotation (c) and only C_2 inter-sites hopping (d).

Table 2-6 EXPRESS simulation derived localized rotation angles θ and non-localized hopping angles γ for site 1 from HT ^{13}C spectra of $^{13}CO_2$ loaded in α-Mg formate

	293 K	**313 K**	**333 K**	**353 K**	**393K**
θ (°)	49(0.5)	49(0.5)	48.5(0.5)	48(0.5)	47(0.5)
γ (°)	42(1)	45(1)	45(1)	44(1)	42(1)

θ remains at 49 ° for both 293 K and 313 K, while γ increases from 42 ° to 45 °. Above 313 K, both θ and γ show a decreasing trend, and the decrease of γ is more severe than θ. The smaller values of θ and γ along with the increased Ω values at higher temperature all indicate that both the localized rotation and twofold hopping of CO_2 molecules get restricted at higher temperatures.

EXPRESS simulation was also performed for site 3, and the results are summarized in Figure 2.15 and Table 2-7.

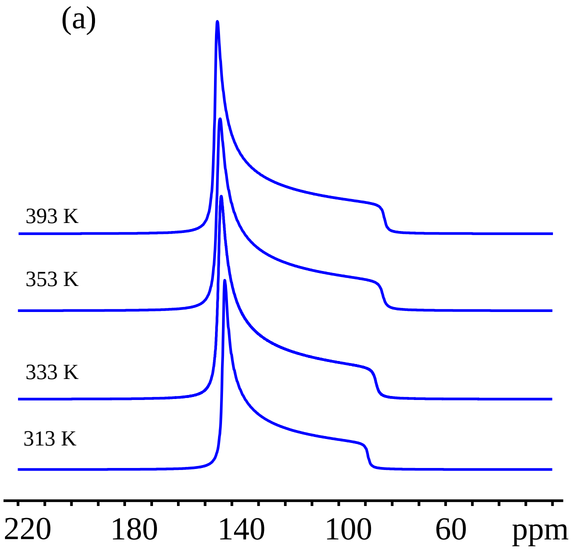

Figure 2.15 – Derived site 3 from ^{13}C experimental HT spectra of $^{13}CO_2$ loaded α-Mg formate (a)

and EXPRESS simulation (b).

Table 2-7 EXPRESS simulation derived localized rotation angle θ for site 3 from HT ^{13}C spectra of $^{13}CO_2$ loaded in α-Mg formate

	313 K	**333 K**	**353 K**	**393K**
θ (°)	48.5(0.5)	48 (0.5)	47.5(0.5)	47.5(0.5)

Unlike site 1, site 3 cannot be simulated using a combined motion. Instead, the site 3 spectra are the result of only a localized rotation, which can be modeled by a C_6 exchange during EXPRESS simulation. No inter-sites hopping is observed based on the simulation. Interestingly, the values of rotation angles θ of this site are very close to the θ values from site 1, and also show a slight decreasing trend as temperature increases. Combined with the percentage analysis of the three sites, these results suggest that the structural change occur at higher temperature influence a small portion of CO_2 greatly. The localized rotation of these CO_2 molecules is slightly restricted, resulting in the observed line broadening of the spectra. The inter-sites hopping on the other hand, has been completely removed, which suggests that the channels in the framework may be more confined during the HT experiments. Therefore, a subtle shrinkage of the framework might occur at higher temperature, also known as negative thermal expansion. This effect has long been studied for MOF-5 and HKUST-1,[27,28] where the unit cells of the materials shrink at higher temperatures. Conducting single crystal X-ray analysis of α-Mg formate at high temperature would be useful to confirm this hypothesis.

To sum up the EXPRESS simulation for the whole VT experiments, Figure 2.16 summarizes how the localized rotation angle θ and non-localized twofold hopping angle γ of site 1 and 3 change as a function of temperature from 173 K to 393 K.

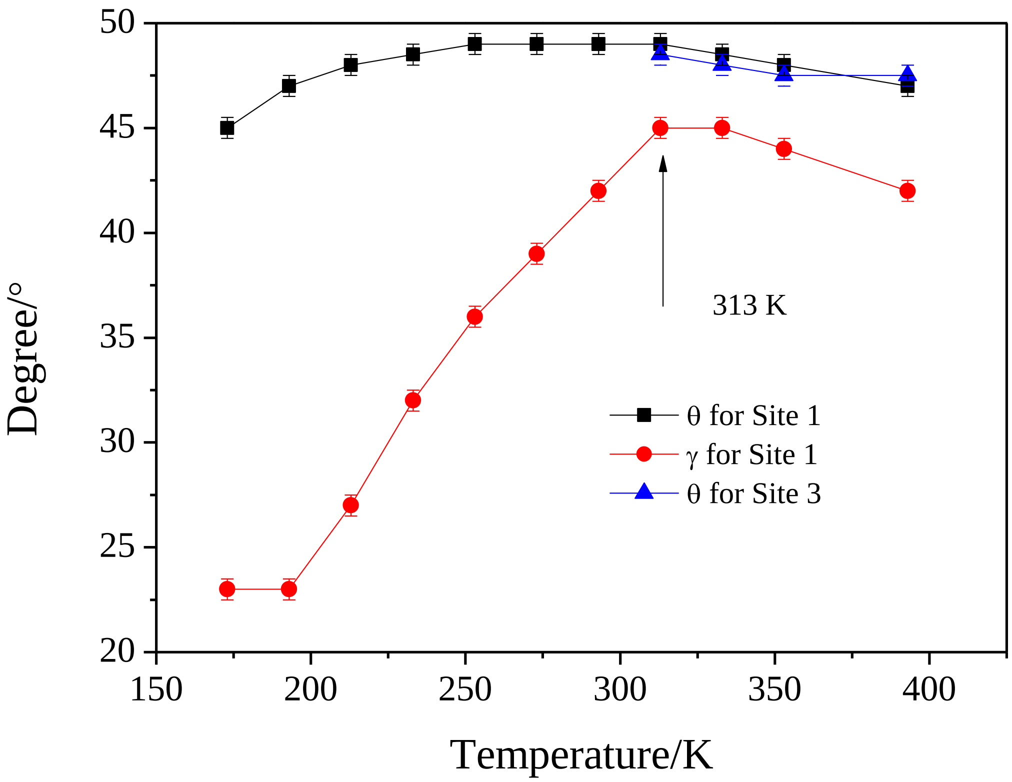

Figure 2.16 – Localized rotation angle θ and non-localized twofold hopping angle γ of $^{13}CO_2$ loaded in α-Mg formate for site 1 and 3 as a function of temperature.

Site 1 represents a combined motion of a localized rotation with angle θ and a simultaneous two-sites hopping with angle γ. All CO_2 molecules undergo this type of motion during LT experiments. On the other hand, during HT experiments, there are three types of motion followed by CO_2, as indicated by the three sites derived from HT spectra, though most CO_2 molecules still possess this combined motion. Both θ and γ for site 1 increase as temperature gets up till 313 K, and both decrease from 333 K to 393 K. Site 3 appears from 313 K and is associated with a simple localized rotation with angle θ, which is proven to be inversely related to temperature. Both sites are more restricted at 393 K compared to 313K, reflected by the smaller values of the angles, indicating the structural change is more severe and have a stronger impact on the adsorbed CO_2 molecules at higher temperatures.

Combined with CP results, a conclusion can be made based on the analysis so far: From 293 K and below, all CO_2 molecules possess the combined motion. Whereas at temperature 313 K and above, a subtle shrinkage of the channels take place, which not only dampers the combined motion, but also gives rise to a new resonance associated with CO_2 molecules that only possess localized rotation. Though the majority of CO_2 molecules still possess the combined motion other than the simple localized rotation.

2.3.3 Discussion of possible CO_2 adsorption sites within α-Mg formate framework based on MD simulation

Molecular dynamic simulation was carried out to locate CO_2 position in the porous structure. Figure 2.17 shows the carbon atom distribution near the minimum energy configuration within α-Mg formate at 253 K along three crystallographic axes. It is clear that two minimum energy configurations in the channels are observed. In the structure of α-Mg formate, a twofold screw axis sits at the centre of the channel along b axis. And those two minimum energy configurations are also related by the twofold screw axis. Therefore, the twofold non-localized hopping of CO_2 based on EXPRESS simulation might occur between the two minimum configurations when certain conditions are met.

MD simulations at different temperatures were also conducted to provide a better understanding of how carbon distribution changes with respect to temperature. The results are shown in Figure 2.18. It is worth mentioning that the cone-shape distribution of carbon atoms might be owing to a cone shape rotation of CO_2 molecules upon the adsorption sites, which is consistent with the end-on adsorption behavior we assumed earlier in this chapter.

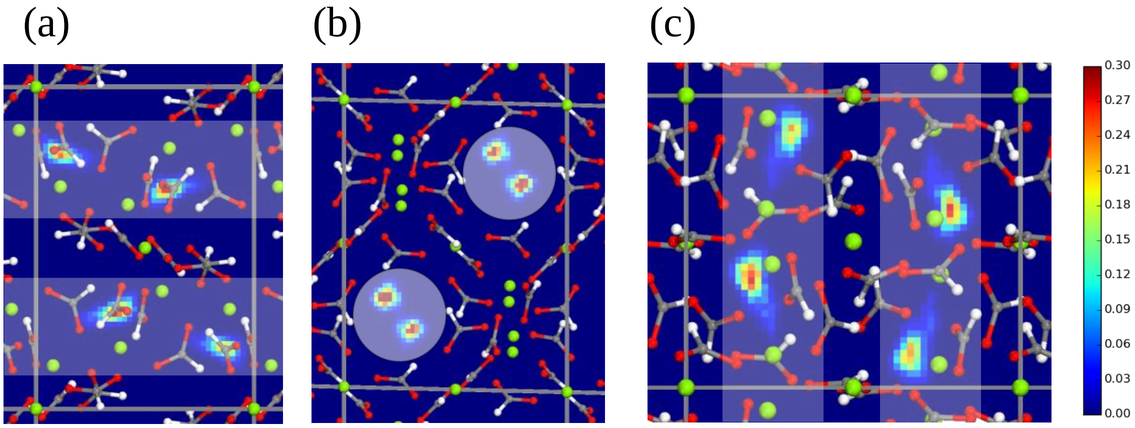

Figure 2.17 - The distribution of carbon atoms of CO_2 in α-Mg formate at 253K, projected on plane yz (a), xz (b) and xy (c). The gray area represents the channels. The color of C, H, O, Mg are in gray, white, red and green, respectively.

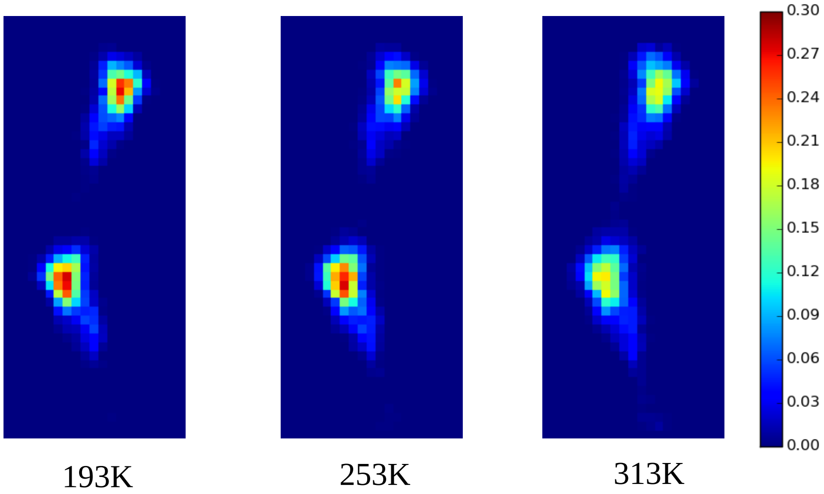

Figure 2.18 - The distribution of carbon atom of CO_2 in α-Mg formate projected on xy plane at different temperatures. (The structure of the framework is fixed at all temperatures during MD simulation)

As temperature increases from 193 K to 313 K, the distribution of carbon atoms appears to be more delocalized, owing to CO_2 molecules possessing higher degree of mobility therefore travelling in a larger area. This result is in accordance with EXPRESS simulation results, which has confirmed that the localized rotation angle θ gets bigger at higher temperature. Radial distribution function also directly confirms this by showing the distance between carbon/oxygen atoms in CO_2 and hydrogen atoms from the framework at different temperatures, as shown in Figure 2.19.

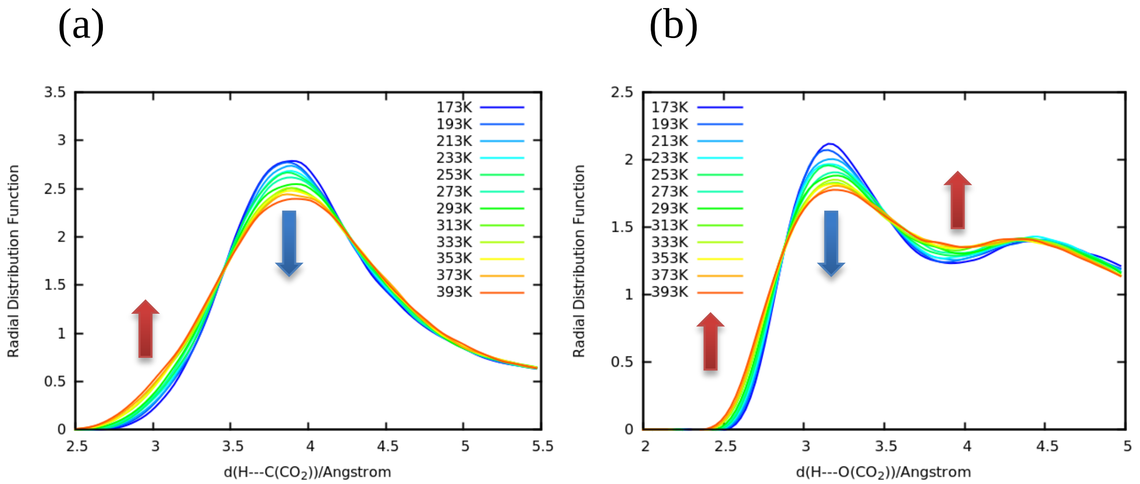

Figure 2.19 - The radial distribution function (RDF) of carbon (a) and oxygen (b) atoms in the adsorbed CO_2 and framework H.

The largest distribution of carbon and oxygen atoms is found to be at 3.8 Å and 3.2 Å respectively throughout the whole temperature range. For carbon atom, at higher temperature, the distribution at 3.8 Å decreases, while it increases at the area within close proximity (3 Å to 5 Å). A similar result is also observed for oxygen atoms, confirming that CO_2 movements take place in a larger area at higher temperature.

Combined with EXPRESS simulation discussed earlier in this chapter, a full picture of CO_2 movements inside the α-Mg formate for a wide temperature range is unveiled. In the structure of α-Mg formate, only three types of hydrogen atoms (H1, H5 and H6) are pointing toward the pore and accessible to CO_2 molecules, and the hydrogen atoms "hidden" within the zigzag chains are not taken into account (H2, H3 and H4) in this work. The two minimum energy configurations related by a twofold screw axis are labeled as position A and B in Figure 2.20, which are both in close proximity to two hydrogen groups consisting of H1, H5 and H6. The two sets of hydrogen atoms also related by a twofold screw axis. The distances between two hydrogen atoms among H1, H5 and H6 observed at each minimum configuration are shown as the followings: H1-H5: 3.94 Å; H1-H6: 3.37 Å; H5-H6: 3.78 Å. During LT experiment, the hopping motion of CO_2 molecules tend to take place in a small area, reflected by the relatively small inter-sites hopping angles based on EXPRESS simulation, suggesting a small active area for CO_2 molecules. Therefore under such circumstances, the two-sites hopping of CO_2 molecules are most likely to occur between H1 and H5, H5 and H6 or H1 and H6 within one minimum energy configuration. Whereas at higher temperature, the hopping angle is as high as 45 °, indicating the hopping motion takes place between two hydrogen sites more distant from each other. Considering the kinetic size of CO_2 is about 3.3 Å along with the narrow pore size of α-Mg formate,[29] geometrically, the distance between any two hydrogen sites within one minimum configuration is too small for CO_2 molecules to perform a large angle inter-sites hopping like this. Therefore, we considered the possibility that at higher temperature, the inter-sites hopping happens between two hydrogen sites that belong to different configurations. The distances of the same type of hydrogen sites, but belong to two configurations are shown as following: H1- H1: 7.117 Å, H5-H5: 7.320 Å, and H6-H6: 7.882 Å, which are significantly larger than the distances between hydrogen atoms within one configuration. Hence, we propose that under this condition, CO_2 molecules are more dynamic and the twofold hopping is more likely to take place down the 1D channel from position A to position B. The CO_2 movement is summarized in Figure 2.20 and Figure 2.21, which are viewing down crystallographic b axis and the diagonal direction of a and c axes.

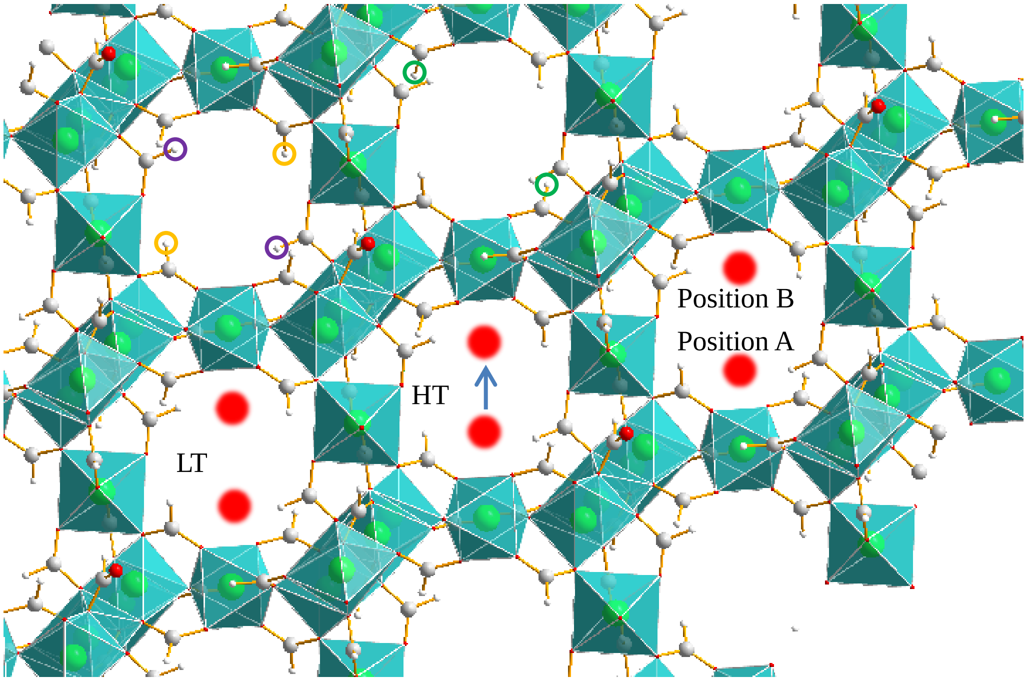

Figure 2.20 - Enlarged framework structure of α-Mg formate viewed down crystallographic b axis. Hydrogen 1 (H1) are labeled by purple circles, H5 and H6 are labeled by yellow and green circles. For the sake of clarification, the three types of hydrogen atoms are not labeled within one channel. The red area is the minimum energy configuration confirmed by MD simulation. The proposed CO_2 motion of LT and HT are also shown in separate channels for clarification. During LT experiments, CO_2 molecules follow the combined motion upon the hydrogen atoms at position A **or** B; during HT experiment, the twofold non-localized hopping occur between hydrogen atoms at position A **and** B.

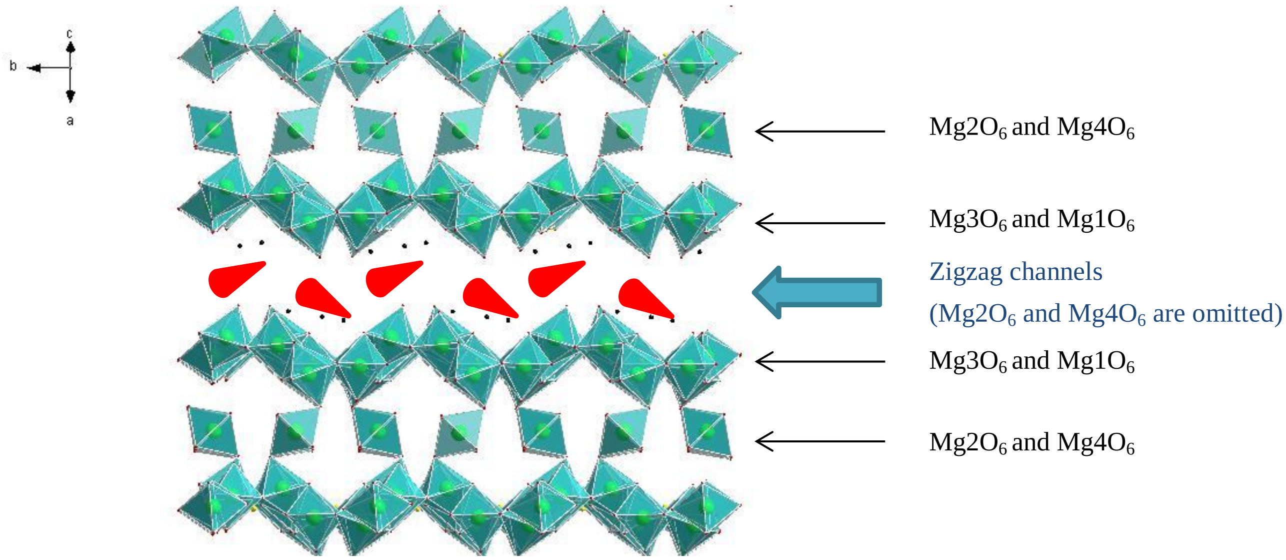

Figure 2.21 - Crystal structure of α-Mg formate viewed down the diagonal direction between a and c axes. To show the shape of the channels, Mg_2O_6 and Mg_4O_6 octahedra are omitted for the middle part. For the sake of clarification, only hydrogen atoms that have direct access to guest species are drawn in this structure (H1, H5 and H6), as the black atoms in the channels. The carbon distribution is shown as the red cones in the channels.

2.4 Conclusion

In this chapter, ^{13}C SSNMR along with complementary molecular dynamic simulation have been employed to investigate CO_2 adsorption behavior within α-Mg formate. Up to 313 K, CO_2 molecules obey a combined motion consisting of a localized rotation and a simultaneous two-sites hopping. Above 313K, a small portion of CO_2 molecules undergo a single localized rotation, resulting from possible framework shrinkage. ^{1}H-^{13}C CP experiments suggest the adsorption sites are the hydrogen atoms from the framework, and the follow-up MD simulation has unveiled the spatial distribution of carbon/oxygen atoms in CO_2 within the porous framework: (1) Within the porous structure of α-Mg formate, two minimum configurations (position A and B) of carbon atoms related by a two-fold screw axis are discovered, and each configuration is within close proximity with three proton sites, H1, H5 and H6; (2) carbon atoms are more delocalized at higher temperature; (3) an end-on adsorption of CO_2 molecules is anticipated based on the cone-shape distribution. During LT experiments, CO_2 molecules primarily adsorb on either H1, H5 or H6 at position A OR B, and two-sites non-localized hopping is likely to take place between two hydrogen sites within one minimum configuration. Whereas at higher temperature, CO_2 molecules become more mobile, and the two hydrogen sites where twofold hopping takes place might belong to different configurations (i.e. one hydrogen site is one of the H1, H5 and H6 from position A, the other hydrogen site is one of the H1, H5 and H6 from position B).

2.5 Bibliography

(1) Reger, D. L.; Leitner, A. P.; Smith, M. D. *Inorganic Chemistry* **2012**, *51*, 10071.

(2) Plonka, A. M.; Banerjee, D.; Woerner, W. R.; Zhang, Z.; Nijem, N.; Chabal, Y. J.; Li, J.; Parise, J. B. *Angewandte Chemie International Edition* **2013**, *52*, 1692.

(3) Mallick, A.; Saha, S.; Pachfule, P.; Roy, S.; Banerjee, R. *Inorganic Chemistry* **2011**, *50*, 1392.

(4) Rood, J. A.; Noll, B. C.; Henderson, K. W. *Inorganic Chemistry* **2006**, *45*, 5521.

(5) Viertelhaus, M.; Adler, P.; Clérac, R.; Anson, Christopher E.; Powell, Annie K. *European Journal of Inorganic Chemistry* **2005**, *2005*, 692.

(6) Samsonenko, D. G.; Kim, H.; Sun, Y.; Kim, G.-H.; Lee, H.-S.; Kim, K. *Chemistry – An Asian Journal* **2007**, *2*, 484.

(7) He, P.; Xu, J.; Terskikh, V. V.; Sutrisno, A.; Nie, H.-Y.; Huang, Y. *The Journal of Physical Chemistry C* **2013**, *117*, 16953.

(8) Xu, J.; Terskikh, V. V.; Huang, Y. *Chemistry – A European Journal* **2013**, *19*, 4432.

(9) Mason, J. A.; Sumida, K.; Herm, Z. R.; Krishna, R.; Long, J. R. *Energy & Environmental Science* **2011**, *4*, 3030.

(10) McDonald, T. M.; Lee, W. R.; Mason, J. A.; Wiers, B. M.; Hong, C. S.; Long, J. R. *Journal of the American Chemical Society* **2012**, *134*, 7056.

(11) Deng, H.; Grunder, S.; Cordova, K. E.; Valente, C.; Furukawa, H.; Hmadeh, M.; Gándara, F.; Whalley, A. C.; Liu, Z.; Asahina, S.; Kazumori, H.; O'Keeffe, M.; Terasaki, O.; Stoddart, J. F.; Yaghi, O. M. *Science* **2012**, *336*, 1018.

(12) Mao, H.; Xu, J.; Hu, Y.; Huang, Y.; Song, Y. *Journal of Materials Chemistry A* **2015**, *3*, 11976.

(13) Xu, J.; Terskikh, V. V.; Chu, Y.; Zheng, A.; Huang, Y. *Chemistry of Materials* **2015**, *27*, 3306.

(14) Lopez, M. G.; Canepa, P.; Thonhauser, T. *The Journal of Chemical Physics* **2013**, *138*, 154704.

(15) Gul-E-Noor, F.; Mendt, M.; Michel, D.; Pöppl, A.; Krautscheid, H.; Haase, J.; Bertmer, M. *The Journal of Physical Chemistry C* **2013**, *117*, 7703.

(16) Wang, W. D.; Lucier, B. E. G.; Terskikh, V. V.; Wang, W.; Huang, Y. *The Journal of Physical Chemistry Letters* **2014**, *5*, 3360.

(17) Lin, L.-C.; Kim, J.; Kong, X.; Scott, E.; McDonald, T. M.; Long, J. R.; Reimer, J. A.; Smit, B. *Angewandte Chemie International Edition* **2013**, *52*, 4410.

(18) Kong, X.; Scott, E.; Ding, W.; Mason, J. A.; Long, J. R.; Reimer, J. A. *Journal of the American Chemical Society* **2012**, *134*, 14341.

(19) Beeler, A. J.; Orendt, A. M.; Grant, D. M.; Cutts, P. W.; Michl, J.; Zilm, K. W.; Downing, J. W.; Facelli, J. C.; Schindler, M. S.; Kutzelnigg, W. *Journal of the American Chemical Society* **1984**, *106*, 7672.

(20) Macho, V.; Brombacher, L.; Spiess, H. W. *Appl. Magn. Reson.* **2001**, *20*, 405.

(21) Vold, R. L.; Hoatson, G. L. *Journal of Magnetic Resonance* **2009**, *198*, 57.

(22) *Acorn NMR Inc. http://www.acornnmr.com (accessed July 17, 2015).*

(23) *Eberhard Karls Universität Tübingen, Homepage Klaus Eichele. http://anorganik.uni-tuebingen.de/klaus/soft/index.php (Accessed July 17, 2015).*

(24) *NMR@CEMHTI. http://nmr.cemhti.cnrs-orleans.fr/Default.aspx (Accessed July 17, 2015).*

(25) Huang, Y.; Demko, B. A.; Kirby, C. W. *Chemistry of Materials* **2003**, *15*, 2437.

(26) Dietzel, P. D. C.; Johnsen, R. E.; Fjellvag, H.; Bordiga, S.; Groppo, E.; Chavan, S.; Blom, R. *Chemical Communications* **2008**, 5125.

(27) Lock, N.; Wu, Y.; Christensen, M.; Cameron, L. J.; Peterson, V. K.; Bridgeman, A. J.; Kepert, C. J.; Iversen, B. B. *The Journal of Physical Chemistry C* **2010**, *114*, 16181.

(28) Tafipolsky, M.; Amirjalayer, S.; Schmid, R. *The Journal of Physical Chemistry C* **2010**, *114*, 14402.

(29) Duan, J.; Higuchi, M.; Krishna, R.; Kiyonaga, T.; Tsutsumi, Y.; Sato, Y.; Kubota, Y.; Takata, M.; Kitagawa, S. *Chemical Science* **2014**, *5*, 660.

2.6 Appendix

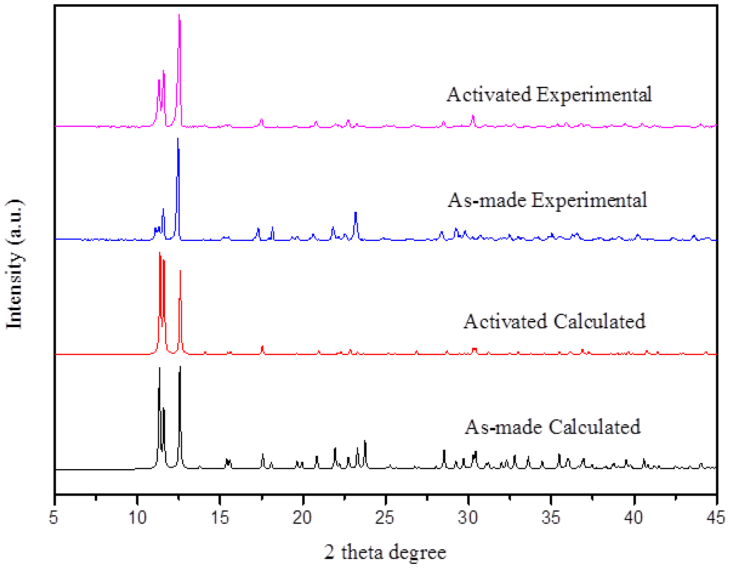

Figure S2.1 - Calculated and experimental PXRD results of as-made and activated α-Mg formate.

Chapter 3 Dynamic study of C_2D_4 in α-Mg formate and CPO-27-M (M = Mg and Zn) using ^{2}H SSNMR

3.1 Introduction

Ethylene, as the simplest alkene, is widely involved in multiple important industrial processes including the production of polyethylene,[1] ethylene glycol, and ethylene oxide.[2] It is also extensively studied as a ripening agent which can be naturally emitted by many fruits including bananas, apples, peaches etc.[3] Currently, the industrial production of ethylene is mostly hydrocracking of fossil fuels. As a result, the product is always a mixture of ethylene and other hydrocarbons such as ethane and propane, which has made the separation and storage of ethylene a popular research interest in recent years.[4,5] The merits of MOFs such as high porosity, light weight, and structural stability have made them especially interesting regarding this issue.[6-9] In this chapter, ethylene adsorption behaviors in α-Mg formate, CPO-27-Mg and -Zn are studied using ^{13}C and ^{2}H SSNMR as well as single crystal X-ray diffraction.

To the best of our knowledge, no previous study has thoroughly explained the ethylene adsorption behaviors in α-Mg formate. However, an interesting experiment regarding this guest-host system caught our attention.[10] This experiment qualitatively examined the adsorption of ethylene (naturally emitted by bananas) with the use of commercially available Basolite M050, i.e. α-Mg formate. In this experiment, two 600g bundles of bananas were sealed in two containers. One had the α-Mg formate in the container and the other did not. After twelve days, the bananas with MOF still "looked fresh, smelled sweet, and were edible without mold on the surface." Meanwhile control samples without MOF in the container were smelly, moldy and inedible, indicating the excess C_2H_4 emitted by bananas were indeed adsorbed by α-Mg formate. However, no further quantitative analysis was done during this experiment therefore the details of ethylene adsorption behavior in this type of MOF still remains unknown. Previously reported

C_2H_2 adsorbed in α-Mg formate might be useful in understanding this mystery.[11,12] In Fischer's work, C_2H_2/CO_2 selectivity in α-Mg formate was studied.[11] Due to the van der Waals interaction between the hydrogen atoms in C_2H_2 and the oxygen atoms on the formate anions in the structure, α-Mg formate shows outstanding preferential adsorption towards C_2H_2 over CO_2. In addition, the adsorbed C_2H_2 molecules occupy two independent positions in the zigzag channels with a population 0.75:0.25. Due to the structural similarity between ethylene and acetylene, a similar adsorption behavior is anticipated for ethylene.

Compared to α-Mg formate, CPO-27-M is better studied both experimentally and computationally in terms of gas adsorption and separation due to its high porosity and high density of unsaturated metal sites which could serve as strong adsorption sites in the structures.[13-16] CPO-27-M features of family of isostructural MOFs with a chemical formula of $C_4H_{11}O_8M$, which is also often referred to as M-MOF-74 and M_2(dobdc) (M = Fe, Mn, Mg, Co, Cu, Zn, Ni; dobdc^{4-} = 2,5-dioxido-1,4-benzenedicarboxylate). This type of MOF crystalizes in trigonal R-3 space group with a = b = 25.87 Å, and c = 6.628 Å. The crystal structure is shown in Figure 3.1.

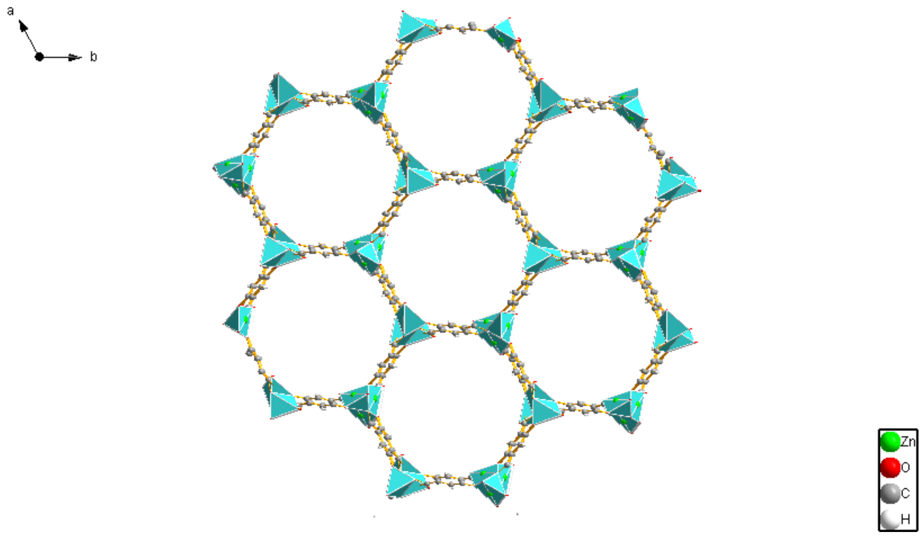

Figure 3.1 - Crystal structure of CPO-27-Zn viewed down crystallographic c axis.

CPO-27-M with various metal centres have been successfully synthesized and structurally resolved by means of single crystal X-ray diffraction and neutron diffraction.[17-20] In the structure of CPO-27-M, the metal centres are octahedrally coordinated to six oxygen atoms, five of which are from four surrounding dobdc linkers, and the sixth one belonging to the adsorbed water molecule. Upon dehydration, the adsorbed water molecules are removed and the metal sites become five-coordinated and carry two positive charges, also known as the unsaturated/open metal sites. The square pyramids created by M^{2+} and their five coordinated oxygen atoms are interconnected with each other in an edge-share fashion and related by a three-fold screw axis, creating helical chains down crystallographic c axis. The chains are interconnected by the dobdc linkers, creating one dimensional honeycomb-shape channels along c axis with a diameter about 12 Å.

The unsaturated metal sites in CPO-27-M are able to strongly bound to guest species through the electron donating and accepting interaction.[21] In Z. Bao's recent work,[21] the adsorption behavior of ethane, ethylene, propane and propylene within CPO-27-Mg were predicted by Monte Carlo simulation. Among these hydrocarbons, propylene showed the strongest affinity to the Mg^{2+} sites due to its large dipole moment. Both ethylene and ethane do not possess dipole moments, but the π bond in ethylene resulted in higher binding strength with the open metal sites in comparison with ethane. Similar results were also found in another study regarding hydrocarbon adsorption in CPO-27-Fe,[22] which showed an affinity to guest species of acetylene > ethylene > propylene > propane > ethane > methane in this type of MOF.

Although the CPO-27-M MOFs with different metal centres are isostructural, the observed affinities between the guest molecules and host MOFs differ greatly due to the dissimilar electronic environments of the different unsaturated metal sites. In terms of ethylene adsorption, a previous study reported the affinity of C_2H_4 and CPO-27-M with different metal centres to be CPO-27-Fe > Mn > Mg > Co > Zn.[23] In E. Bloch's work, the use of neutron diffraction accurately pinpoints the location of ethylene molecules to be upon the Fe^{2+} sites in CPO-27-Fe with a side-on adsorption manner.[22] Similar result was also observed in CPO-27-Co.[23] Interestingly, in Bao's work,[21] the grand canonical Monte Carlo simulation suggested that there might be an additional adsorption site in the middle of the honeycomb channels of CPO-27-Mg. Further experimental proof is needed to confirm this simulation.

The adsorption behavior of ethylene in different MOFs is studied by means of deuterium NMR upon the deuterated ethylene loaded MOFs, which is able to clearly pinpoint the type of nuclear reorientation such as twofold and sixfold exchange, as well as the rate of the reorientation. The slow ($< 10^3$ Hz), intermediate ($10^3 <$ rate $< 10^7$ Hz), and fast limit regimes (rate $> 10^7$ Hz) are generally used to differentiate how rapid the reorientation process is.[24] The ultrahigh sensitivity of ^{2}H NMR originates from the relatively small quadrupolar coupling constant C_Q of deuterium nuclei.[25] As a result, the produced Pake doublet spectrum changes drastically when the dynamic of ^{2}H nucleus changes.

To the best of our knowledge, very few reports have focused on using ^{2}H SSNMR to study the ethylene dynamics in porous materials, most of which are with regard to zeolites. NaX is a well-studied X type zeolite that possesses typical faujasite structure.[26] The framework consists of sodalite cages (or β-cage) connected through hexagonal prisms, giving rise to supercage (or α-cage) with size of 12 Å. Burmeister et al studied dynamics of ethylene molecules in this type of zeolite using ^{2}H SSNMR,[27] which has shown that the C_2D_4 molecules undergo fast isotropic reorientation, giving rise to a featureless Lorentzian-shape spectrum even at 77 K. With a replacement of 20% of the Na^+ cations with Ag^+, C_2D_4 molecules undergo a 180 ° flip from 167 K and below, resulting in a very well-defined Pake doublet spectrum. These results indicated that the exchanged Ag^+ cations in the structure were accounted for the enhancement in C_2D_4 affinity. Another work using Monte Carlo lattice dynamics simulation studied the C_2D_4 adsorption behavior in NaA zeolite.[28] The structure of NaA is very similar to NaX except slight variation in the β-cages and pore size.[29] Their work indicates that ethylene molecules are able to hop between six sites in the α-cage of zeolite NaA; no inter-sites jumping between the cages are observed.

Nevertheless, the use of ^{2}H SSNMR and the associated simulation methods in studying the guest-host interactions between ethylene and MOFs is still fairly rare.

In this chapter, ^{13}C NMR results on the $^{13}C_2H_4$ loaded α-Mg formate are discussed first. Due to the difficulty in deriving motional information arising from severe line broadening, ^{2}H NMR and the subsequent EXPRESS simulation were then performed to analyze the dynamics of ethylene molecules in two types of MOFs: α-Mg formate and CPO-27-M (M = Zn and Mg). At the end of this chapter, the results of CO_2 and C_2D_4 adsorbed in α-Mg formate will be compared, as well as the results of C_2D_4 loaded in different types of MOFs.

3.2 Experimental

The synthesis of α-Mg formate was described in chapter 2 already. Therefore, only the synthesis route of CPO-27-M will be introduced in this chapter. In addition, the gas adsorption apparatus and procedures were already described in chapter 2. For the sake of simplicity, it is not reintroduced in this chapter.

3.2.1 Synthesis of CPO-27-M

The preparation of CPO-27-M was achieved by a simple solvothermal synthesis following previous literature.[30] First, 0.75 mmol 2,5-dioxido-1,4-benzenedicarboxylate (dobdc, Sigma-Aldrich) was dissolved in 10 ml tetrahydrofuran (THF, reagent grade, Caledon) in a 23 ml Teflon-lined inlet. Next, 3 ml of 1M NaOH solution was slowly added into the inlet with continuous magnetic stirring. 1.5 mmol magnesium/zinc nitrate hexahydrate ($Mg(NO_3)_2$ $6H_2O$ and $Zn(NO_3)_2$ $6H_2O$, Sigma-Aldrich, 99%) was dissolved in 5 ml of deionized water and also added into reaction system. The Teflon inlet was then put into a stainless steel autoclave, sealed and placed in an oven under 110 ℃ for 3 days. After filtration, the light yellow powder was collected, denoted as the as-made samples. In order to obtain dehydrated samples, both CPO-27-Mg and CPO-27-Zn underwent an activation procedure after synthesis. For CPO-27-Zn, the activation process was simply placing the sample under dynamic vacuum for 10 hours at 150 ℃. In the case of CPO-27-Mg, a relatively complicated methanol exchange prior to heating was needed. Methanol was added into the Teflon inlet along with 0.2 g of the as-made CPO-27-Mg. The inlet was then sealed in an autoclave and placed in the oven at 200 ℃. After 24 hours, the autoclave was taken out from the oven and cooled down to room temperature. The mixture was then decanted, and another 10 ml of "fresh" methanol was added into the inlet. This whole process including mixing, heating and decanting was repeated 3 times before filtration. The obtained powder sample was then placed under dynamic vacuum and activated at 250 ℃ for 8 hours. The product of this step was once again, mixed with methanol, and put in a Teflon inlet. After another four times of methanol exchange, an activation at 250 ℃ for 8 hours under dynamic vacuum took place until the final product was collected, denoted as the activated sample.

3.2.2 SSNMR characterization

^{13}C VT experiments were conducted upon the $^{13}C_2H_4$ loaded α-Mg formate from 173 K to 393 K. All ^{13}C spectra were referenced in the same way as mentioned in chapter 2. Depth decoupling pulse sequence was used to eliminate the influence of H-C dipolar coupling and the background signal from the NMR probe. The optimized 90° pulse length and pulse delay were 2.5 μs and 7 s. The acquisition number was 256.

^{2}H SSNMR was performed to study the adsorption behavior of C_2D_4 in α-Mg formate, CPO-27-Mg and Zn. Before acquiring spectrum from the MOFs samples, echo pulse was firstly applied to D_2O sample for referencing purpose. The chemical shift of D_2O was set to 4.8 ppm from Tetramethylsilane (TMS-d_{12}),[31] of which δ_{iso} is 0 ppm by convention. Secondly, deuterium enriched hexamethylbenzene (HMB) spectrum was then collected to provide a rough guideline of the 90 ° pulse length of solid material. The adopted 90 ° pulse lengths were 1.9 μs, 4.0 μs and 3.7 μs for CPO-27-Mg, CPO-27-Zn and α-Mg formate. A pulse delay of 3 s was used upon all three samples. The acquisition numbers was 1600 for CPO-27-M samples and 800 for α-Mg formate. As mentioned in chapter 2, NUTs software was used to process NMR spectrum. WSolids was used to derive the NMR parameters such as quadrupolar coupling constant C_Q, asymmetry η_Q, and dipolar coupling constant D. EXPRESS simulation was conducted to derive the molecular motion of guest species in MOFs. The motions are sometimes abbreviated as C_n, standing for either n fold rotation upon an adsorption site or n fold hopping between sites. The rate of all motions of C_2D_4 molecule in α-Mg formate is considered in the fast regime, whereas in CPO-27-M, the rate changes as a function of temperature. Details will be provided in the discussion section. The adopted values of C_Q and η_Q for stationary C_2D_4 is 230 kHz and 0 according to literature.[32]

3.2.3 Single crystal X-ray analysis

The single crystal X-ray analysis was performed upon C_2D_4 loaded α-Mg formate. The sample was mounted on a Mitegen polyimide micromount with a small amount of Paratone N oil. All X-ray measurements were made on a Bruker Kappa Axis Apex2 diffractometer at a temperature of 110 K. The unit cell dimensions were determined from a symmetry constrained fit of 9898 reflections with $5.02° < 2\theta < 63.04°$. The data collection strategy was a number of scans which collected data up to 63.536° (2θ). The frame integration was performed using SAINT.[33] The resulting raw data was scaled and absorption corrected using a multi-scan averaging of symmetry equivalent data using SADABS.[34] The details of the single crystal analysis are included in the Appendix at the end of this chapter.

The structure was solved by using the coordinates from the isomorphous structure of the activated framework.[35] The ethylene atomic positions were derived from two predominant peaks in a difference Fourier of approximately 2 $e^-/Å^3$ in height. The framework hydrogen atoms were introduced at idealized positions and were allowed to ride on the parent atom. The ethylene deuterium atom positions were obtained in the following way: One peak in the difference map was located at approximately the correct distance from C1X. This position was used to calculate the idealized positions of the remaining three hydrogen atom positions. These deuterium atom positions were allowed to ride on the parent carbon atom. The structural model was fit to the data using full matrix least-squares based on F^2. The calculated structure factors included corrections for anomalous dispersion from the usual tabulation. The structure was refined using the SHELXL-2014 program from the SHELX suite of crystallographic software.[36] Graphic plots were produced using the NRCVAX program suite.[37]

3.3 Results and discussion

3.3.1 $^{13}C_2H_4$ in α-Mg formate

Figure 3.2 shows the ^{13}C spectra from 173 K to 393 K of the $^{13}C_2H_4$ loaded α-Mg formate. The sharp resonance that appears from 313 K near 122 ppm is associated with free ethylene signal, which gets more evident during the heating process. The observed NMR line shape is originated from the strong ^{13}C-^{13}C dipolar coupling interaction characterized by dipolar coupling constant D as well as CSA. The calculated D value for completely stationary $^{13}C_2H_4$ using equation 3 in chapter 1 is 3165 Hz. Ethylene molecules are more dynamic as temperature increases, resulting in much more averaged dipolar interaction and therefore much smaller D values at higher temperature. The biggest D value of 1900 Hz is derived from the spectrum obtained at 233 K, which is much smaller than the aforementioned value for stationary $^{13}C_2H_4$, indicating that the adsorbed ethylene molecules were not nearly stationary at 233 K. As temperature increases, the derived D value continuously becomes smaller and the smallest D value of 1350 Hz is observed at 393 K. It is worth mentioning that due to the severe line broadening present in the spectrum of 213

K and below, the D values cannot be successfully derived by WSolids simulation. The derived CS parameters, weight analysis of the adsorbed and free ethylene, and derived D values are summarized in Table 3-1.

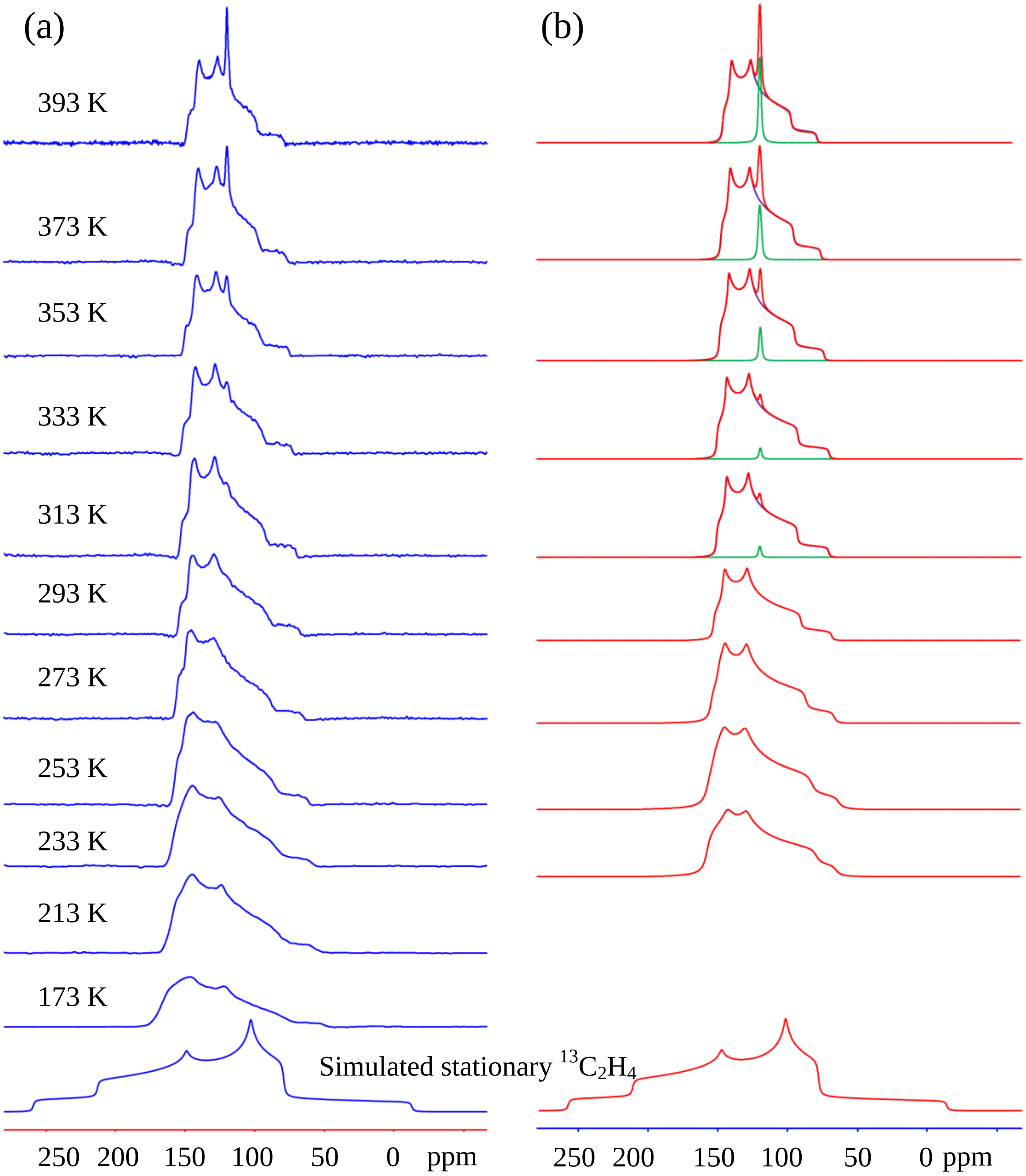

Figure 3.2 - VT ^{13}C experimental (a) and simulated (b) spectra of $^{13}C_2H_4$ loaded in α-Mg formate. Green line spectra in (b) are the derived free ethylene signal.

One of the most important subjects of this study is to understand the dynamics of ethylene in different types of MOFs. However, EXPRESS package does not support the dynamic studies when strong dipolar coupling is present. Therefore, deuterium NMR on C_2D_4 loaded α-Mg formate was proceeded since ^{13}C SSNMR study on $^{13}C_2H_4$ loaded α-Mg formate would only provide limited information.

Table 3-1. Derived CS parameters and D value of ^{13}C VT experimental spectra of $^{13}C_2H_4$ adsorbed in α-Mg formate

	δ_{iso} (ppm)	**Ω (ppm)**	**κ**	**D (Hz)**	**Weight of the adsorbed $^{13}C_2H_4$ (%)**	**Weight of the free $^{13}C_2H_4$ (%)**
393 K	122(1)	44(1.5)	1.00(1)	1350(50)	92(1)	8(1)
373 K	122(1)	47(1.5)	1.00(1)	1400(50)	94(1)	6(1)
353 K	122(1)	49(1.5)	1.00(1)	1450(50)	97(1)	3(1)
333 K	122(1)	51(1.5)	1.00(1)	1500(50)	98(1)	2(1)
313 K	122(1)	54(1.5)	1.00(1)	1550(50)	99(1)	1(1)
293 K	122(1)	57(1.5)	1.00(1)	1650(50)		
273 K	122(1)	60(1.5)	1.00(1)	1700(50)		
253 K	122(1)	65(1.5)	1.00(1)	1800(50)		
233 K	122(1)	67(1.5)	1.00(1)	1900(50)		

3.3.2 C_2D_4 adsorption behavior within α-Mg formate

Figure 3.3 shows the experimental and WSolids simulated ^2H spectra of C_2D_4 loaded α-Mg formate from 173 K to 373 K.

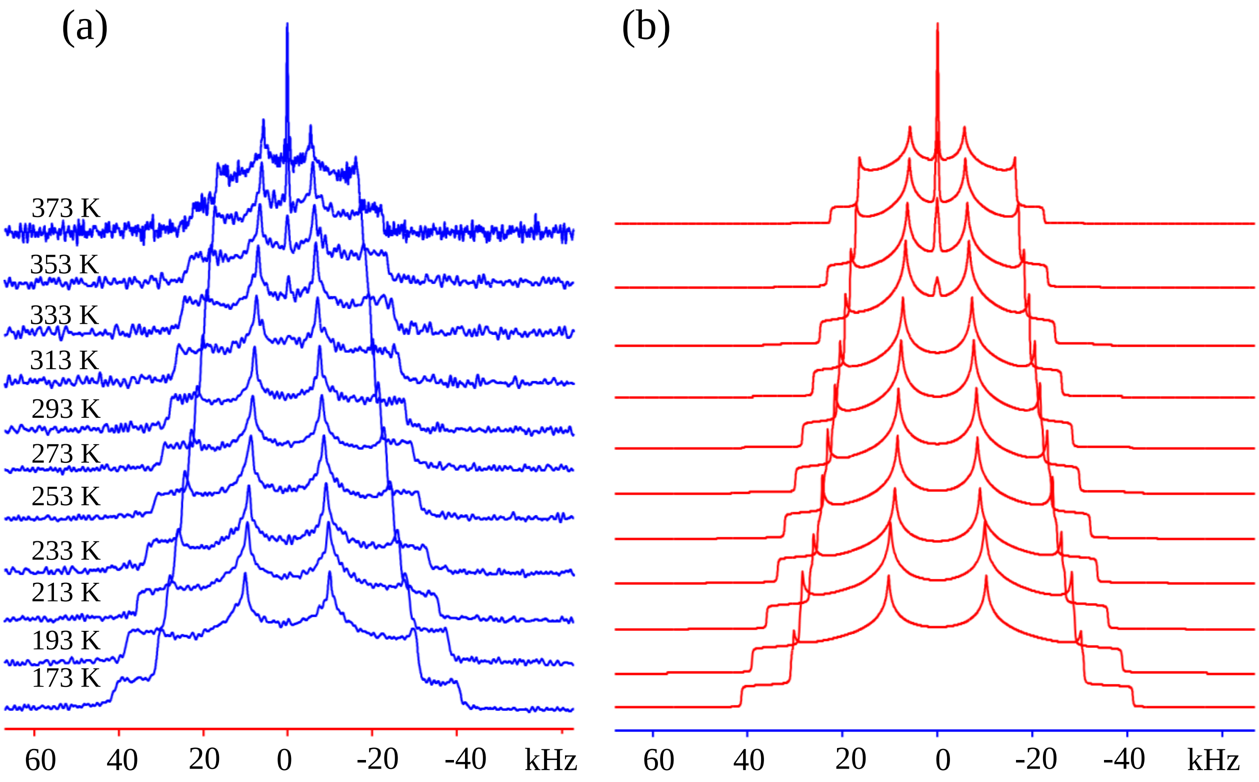

Figure 3.3 - ^{2}H NMR VT experimental (a) and simulated (b) of C_2D_4 loaded α-Mg formate.

As temperature increases, the linewidth of the spectrum gradually gets narrower, resulting from higher degree of mobility that ethylene molecules possess at higher temperature. From 313 K, a sharp resonance at 0 ppm associated with free C_2D_4 signal starts to emerge and becomes more significant during the heating process, suggesting that more C_2D_4 undergo free molecular tumbling without interacting with the framework. Two well-defined powder patterns can be deconvoluted from the experimental spectrum at each temperature based on WSolids simulations, marked as site 1 and 2. The spectrum obtained at 353 K shown in Figure 3.4 is used as an example to demonstrate the three sites deconvolution, and the derived site 1 and site 2 of the whole VT results are stacked in Figure 3.5.

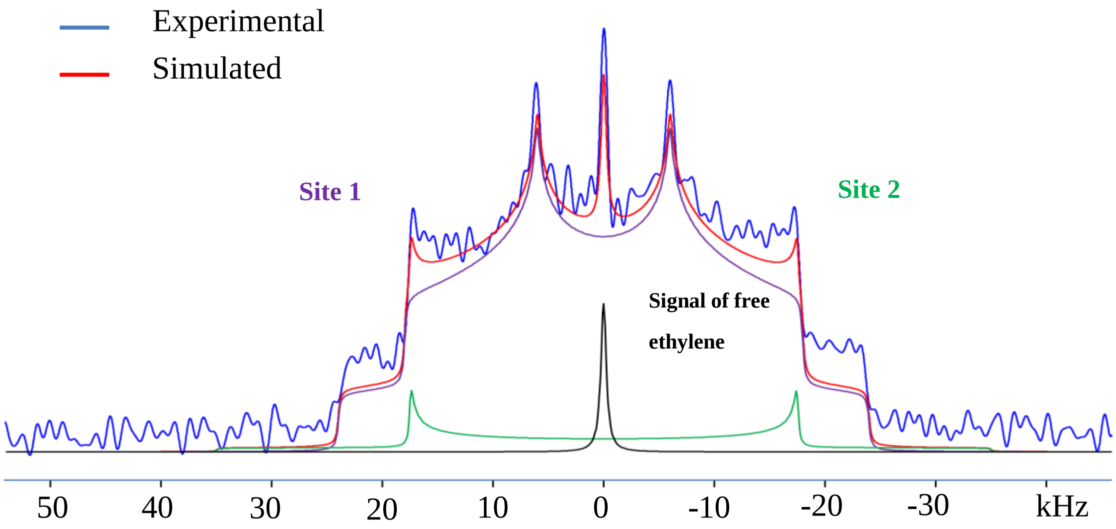

Figure 3.4 – Three sites deconvolution of the ^{2}H spectrum obtained at 353 K of the C_2D_4 loaded in α-Mg formate. Site 1, 2 and the signal of free ethylene are shown as green, purple, and black subspectrum in this figure.

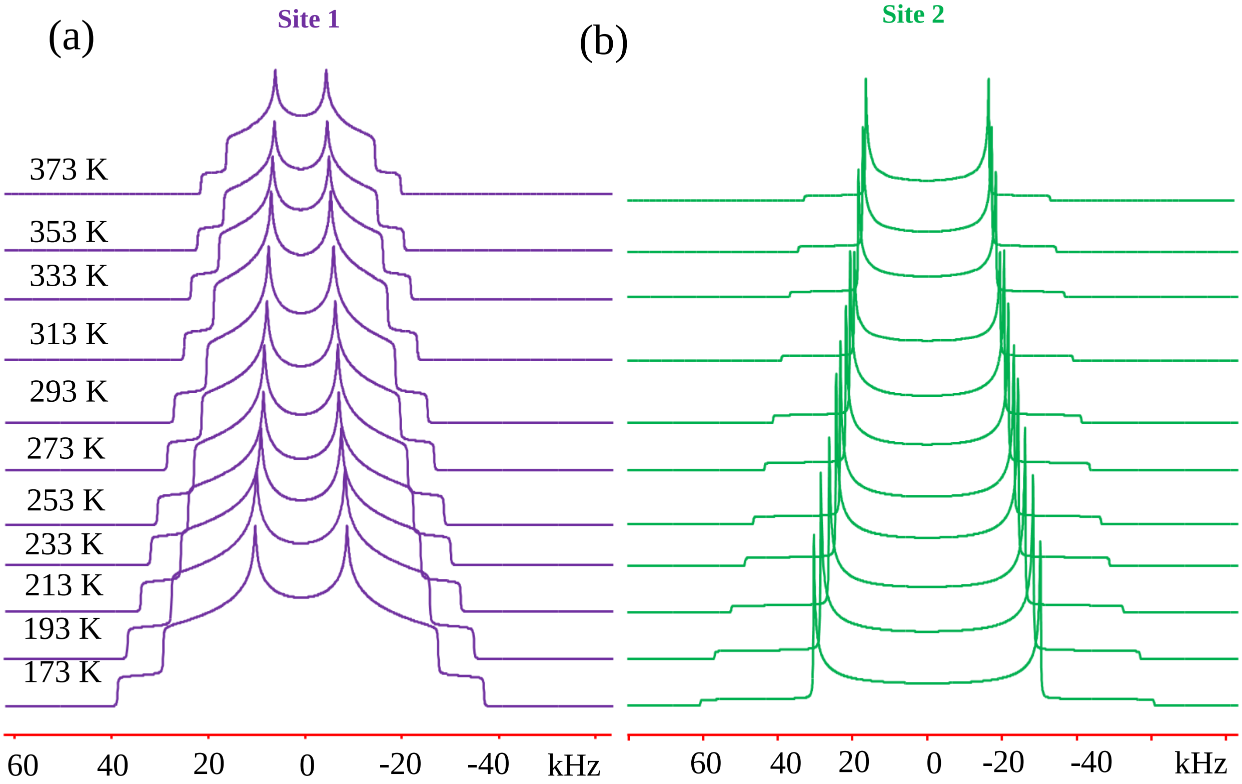

Figure 3.5 - Derived site 1 (a) and site 2 (b) VT spectra of C_2D_4 loaded in α-Mg formate

Table 3-2 Derived quadrupolar parameters of C_2D_4 loaded α-Mg fomrate

	Site 1 C_Q (kHz)	**Site 1 η_Q**	**Site 2 C_Q (kHz)**	**Site 2 η_Q**	**Population of Site 1 (%)**	**Population of Site 2 (%)**	**Population of free C_2D_4 (%)**
173 K	55(1)	0.50(1)	81(1)	0.00(1)	94(1)	6(1)	-
193 K	52(1)	0.49(1)	76(1)	0.00(1)	91(1)	9(1)	-
213 K	48(1)	0.50(1)	70(1)	0.00(1)	91(1)	9(1)	-
233 K	45(1)	0.50(1)	65(1)	0.00(1)	89(1)	11(1)	-
253 K	43(1)	0.49(1)	62(1)	0.00(1)	89(1)	11(1)	-
273 K	40(1)	0.49(1)	58(1)	0.00(1)	89(1)	11(1)	-
293 K	38(1)	0.49(1)	55(1)	0.00(1)	89(1)	11(1)	-
313 K	35(1)	0.49(1)	52(1)	0.00(1)	89(1)	11(1)	1(1)
333 K	33(1)	0.49(1)	49(1)	0.00(1)	87(1)	11(1)	2(1)
353 K	31(1)	0.49(1)	46(1)	0.00(1)	88(1)	11(1)	2(1)
373 K	30(1)	0.49(1)	44(1)	0.00(1)	87(1)	10(1)	3(1)

Site 1 and 2 show distinct line shapes that give rise to different quadrupolar parameters. The simulated C_Q and η_Q of each site as well as the weight percentage are summarized in Table 3-2. The weight percentage analysis suggests that site 1 is the dominant site throughout the whole temperature range. Due to the emergence of site 2 and 3, its population decreases by 2 % from 233 K to 373 K. Site 2 starts out as a very small composition in the spectrum of 173 K, only 6 %. As temperature increases to 233 K, the population of this site has increased to 11% and remains at the same value during the rest of the VT experiments. The population of free ethylene signal increases from 0.5% to 3% from 313 K to 393 K. The C_Q values of both site 1 and 2 are inversely related to temperature, where the higher the experimental temperature is, the smaller the C_Q values are for both sites, which indicates that the QI between ^{2}H nuclei in ethylene and local EFG is more averaged due to the higher degree of mobility of the guest molecules.

EXPRESS simulation was conducted for both site 1 and 2 to analyze the dynamics of ethylene based on NMR line shape. The simulated spectra are shown in Figure 3.6, which suggests that site 1 is generated by C_2D_4 molecules undergoing localized rotation of and a simultaneous non-localized two-sites hopping. Site 2 on the other hand, is yielded by C_2D_4 molecules only possess localized rotation.

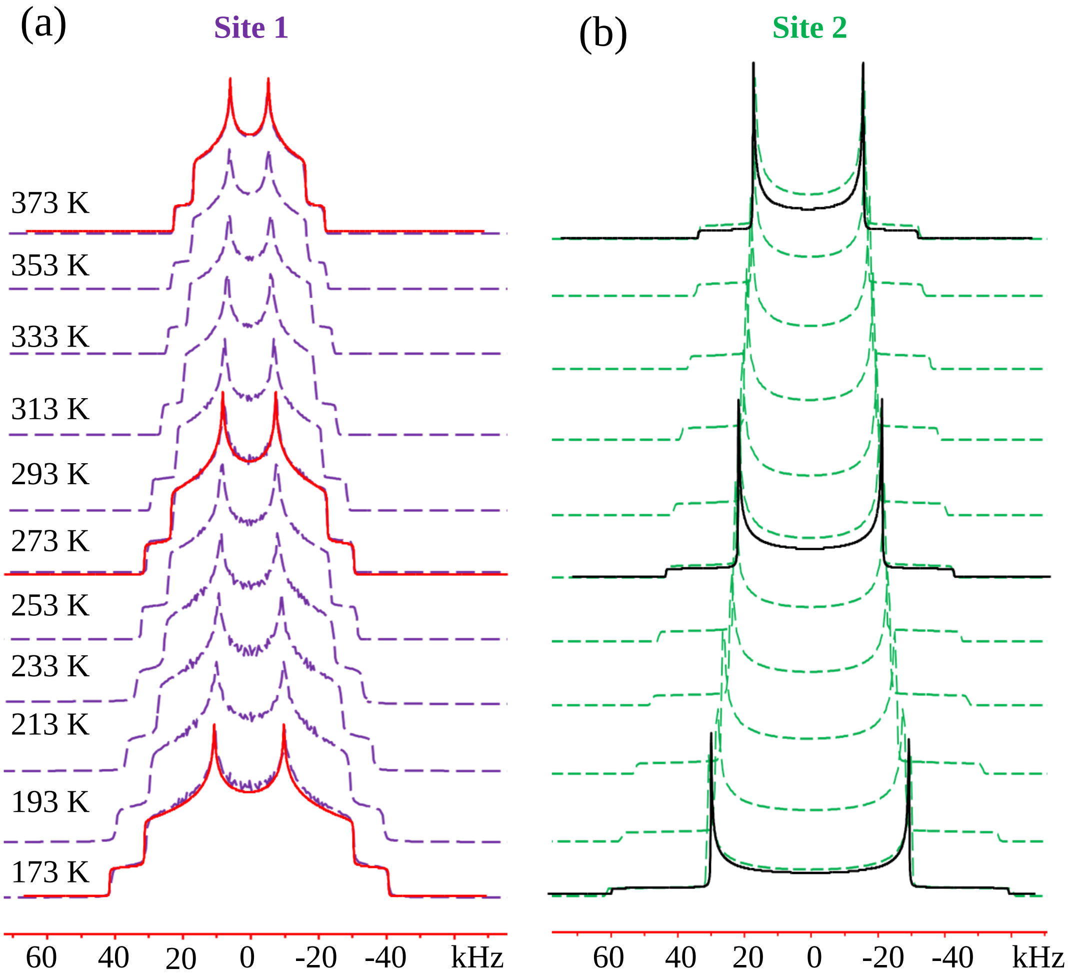

Figure 3.6 - EXPRESS simulation results of site 1 (a) and site 2 (b) of ^2H NMR VT spectra of C_2D_4 loaded α-Mg formate. The dash lines are the derived site 1 and 2 from experimental spectra. For simplicity, only EXPRESS simulated spectra of 173 K, 293 K and 373 K are overlaid as red (site 1) and black (site 2) spectra here.

The localized motion from both site 1 and 2 are characterized by rotation angle θ, and the non-localized two-sites hopping only found in site 1 is characterized by inter-sites hopping angle γ. The as-mentioned adsorption mechanism is depicted in Figure 3.7, and the derived rotation angle θ and hopping angle γ are summarized in Table 3-3. As mentioned in the Experimental section, the rate of the motions ethylene molecules possess in this system is considered to be in the fast regime.

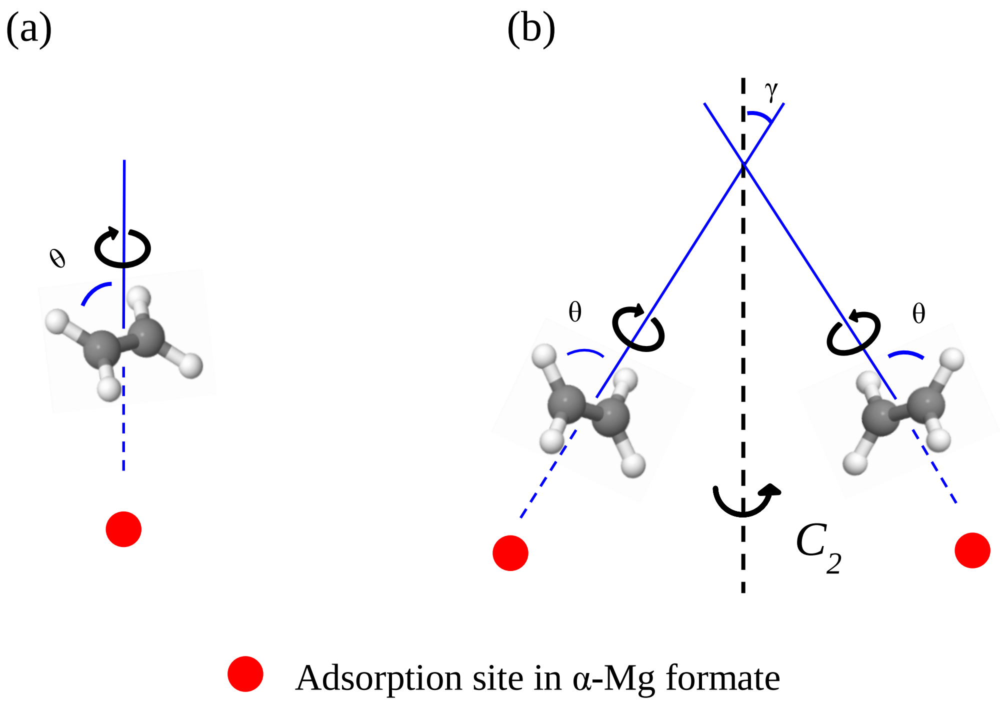

Figure 3.7 – Schematic of the localized rotation derived from site 2 (a), and the combined motion consisting of a localized rotation with an angle θ and non-localized two-sites hopping with an angle γ derived from site 1 (b). The adsorption site will be discussed later in this chapter.

As temperature increases from 173 K to 373 K, the θ values for both site 1 and 2 increase from 41 to 47 °. The inter-sites hopping angle γ of site 1 remains unchanged at 28 °throughout the VT experiment. The existence of two sites in NMR spectra suggests that two groups of ethylene molecules that obey the two distinct motions behind site 1 and 2 are present in the system. Additionally, the population analysis of the two sites in Table 3-2 indicates a majority of the adsorbed ethylene molecules undergo the combined motion instead of the single localized rotation. In order to understand these interesting results, the structure of α-Mg formate has to be taken into consideration. As mentioned earlier in chapter 1, the α-Mg formate possesses zigzag-shaped and very narrow channels with a size of 4.5 × 5.5Å. Considering the reported kinetic diameter of ethylene is about 4.16 Å,[4] it is possible that a small portion of ethylene molecules locating at certain parts of the channels do not have enough space to perform a twofold inter-sites hopping, whereas the majority of the adsorbed ethylene molecules locating at the slightly more spacious area in the framework are able to hop between two equivalent sites. As a result, two distinct Pake doublets are observed in ^{2}H NMR spectra.

Table 3-3 EXPRESS simulation derived localized rotation angle θ for site 1 and 2, and non-localized hopping angle γ for site 1.

	Site 1 θ (°)	**Site 1 γ (°)**	**Site 2 θ (°)**
173 K	41(0.5)	28(0.5)	41(0.5)
193 K	41.5(0.5)	28(0.5)	42(0.5)
213 K	42.5(0.5)	28(0.5)	43(0.5)
233 K	43.5(0.5)	28(0.5)	44(0.5)
253 K	44(0.5)	28(0.5)	44.5(0.5)
273 K	44.5(0.5)	28(0.5)	45(0.5)
293 K	45(0.5)	28(0.5)	45.5(0.5)
313 K	46(0.5)	28(0.5)	46(0.5)
333 K	46.5(0.5)	28(0.5)	46. 5(0.5)
353 K	47(0.5)	28(0.5)	47(0.5)
373 K	47(0.5)	28(0.5)	47(0.5)

Although EXPRESS simulation provides a clear picture of the type of motion that ethylene molecules follow, how ethylene interact with the framework and the adsorption sites still remain unclear. Therefore, single crystal analysis was performed to provide accurate structural information of this guest-host system.

Single crystal analysis of C_2D_4 loaded α-Mg formate

Single crystal X-ray diffraction was conducted upon the ethylene loaded α-Mg formate as a complementary analysis to SSNMR results. The refined structure is shown in Figure 3.8. It is clear that all ethylene molecules are located inside the zigzag channels.

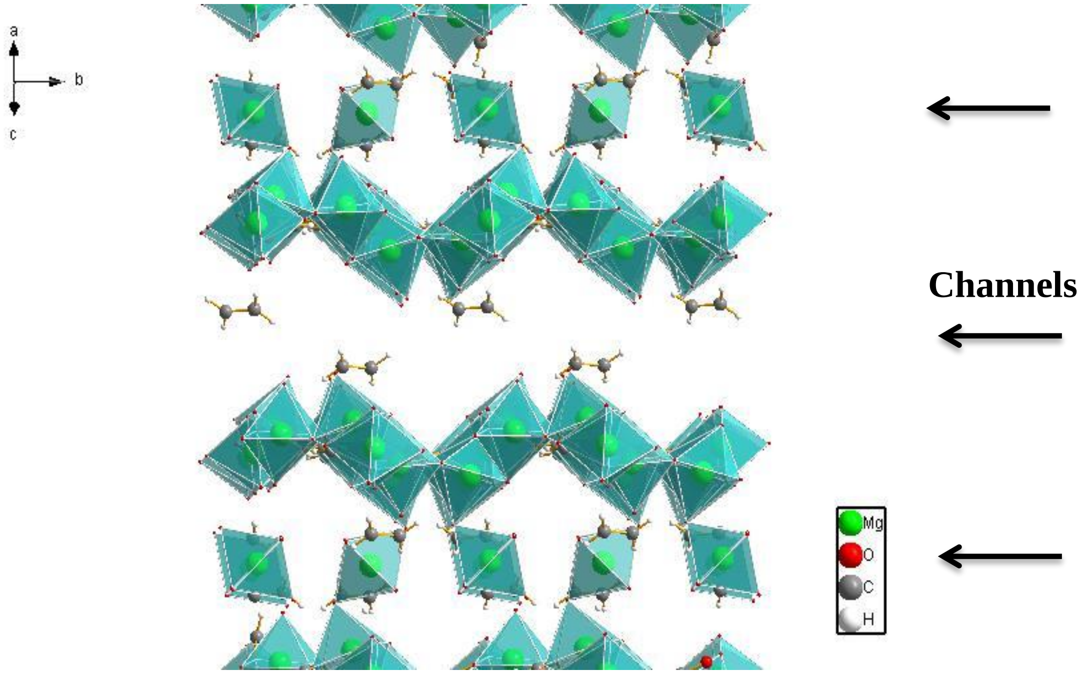

Figure 3.8 - Single crystal structure of C_2D_4 loaded α-Mg formate viewed along the diagonal direction of a and c axes. $Mg2O_6$ and $Mg4O_6$ octahedra and hydrogen atoms are omitted for the channel in the middle in order to have a better view for ethylene sites.

Discussion on the dynamics and adsorption sites of ethylene in α-Mg formate

EXPRESS simulation suggests that there are two types of ethylene molecules that undergo different motions: some follow a combined motion consisting of a localized rotation and a non-localized twofold hopping between the adsorption sites; others undergo a simple localized rotation. The weight analysis suggests that the number of ethylene molecules possessing a localized rotation is significantly less than those follow the combined motion, reflected by a population ratio of 1:9. However, only one type of ethylene molecules is picked up by single crystal X-ray analysis. The discrepancy between X-ray analysis and SSNMR results might be due to the small occupancy of the ethylene molecules possessing only localized rotation. As a result, this portion of ethylene molecules could only be observed by ^{2}H SSNMR due to its ultrahigh sensitivity. It is also possible that this small portion of ethylene reside at the narrower part of the zigzag channels, resulting in the failure of performing inter-sites hopping. However, this speculation needs further experimental proof.

In previously reported single crystal structure of C_2H_2 adsorbed in α-Mg formate, the adsorption site is claimed to be oxygen atoms on the formate anions, and van der Waals interaction between the oxygen and H in C_2H_2 is the reason behind this guest-host interaction.[12] In protein chemistry, a typical H-O hydrogen bond in C-H……O-C system is about 2.1-2.3 Å,[38] and the shortest distance between H in C_2H_2 and O on the framework is about 2.51-2.66 Å in the reported structure. In the case of C_2D_4 loaded α-Mg formate, the shortest C-H……O-C distance of 3.34 Å is observed between D4 (one of the hydrogen atoms in ethylene) and O2 from the framework. This result clearly falls out of the threshold of a typical H-O van der Waals interaction. Therefore, oxygen unlikely to be the adsorption site of C_2D_4 loaded in α-Mg formate.

Another possible adsorption mechanism is the interaction between hydrogen from the framework and the π electrons in ethylene. The H-π interactions between H and unsaturated hydrocarbons have been widely researched.[39] In the ethylene and acetylene matrix,[40] two types of complexes are formed: one is that ethylene being the proton donor to the π cloud in acetylene; the other is that acetylene being the proton donor to the π cloud in ethylene. This conclusion is supported by the discovery of new IR bands when the matrix of ethylene and acetylene was being measured, and those bands are absent when acetylene and ethylene were measured separately. A similar result is also observed in ethylene-benzene matrix.[41]

The above mentioned systems are all in liquid or gaseous phase, and most H-π interaction studied in solid forms focus on the interaction methyl hydrogen and aromatic rings in proteins. In Boisbouvier's recent work, direct interactions between the methyl H and π electrons from the aromatic rings in a number of proteins were identified by ^{1}H-^{13}C heteronuclear multiple quantum coherence (HMQC) NMR experiments.[42] Three criteria must be satisfied to form methyl H and π interaction in these proteins: distance between methyl C and π electrons is less than 4.3 Å; The angle between the C-H and ring centre - H vectors (φ) is greater than 120°; the angle between the six-fold rotation axis sitting at the centre of the ring and a H - ring centre vector (θ) is less than 25°; shown in Figure 3.9a.

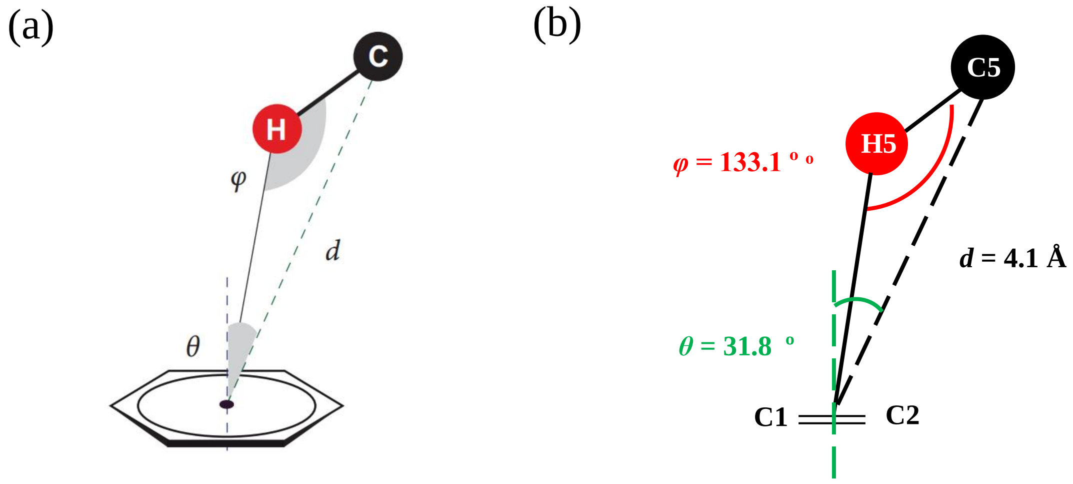

Figure 3.9 - Schematic showing the three parameters (d, φ and θ) used to describe methyl H/π interactions (a), and d, φ and θ values of C_2D_4 loaded α-Mg formate (b).

In the structure of C_2D_4 loaded α-Mg formate, H1 on the framework shows the shortest distances to both carbon atoms in ethylene, which are 3.198 Å to C1X and 3.631 Å to C2X. This geometry of H1 and two carbon atoms in ethylene gives rise to d = 4.1 Å, φ = 133.1 °, and θ = 31.8 °, shown in Figure 3.9b. Both d and φ values met the criteria as they are within the acceptable range. θ is slightly larger than the reported upper limit, which is the result of an off-centered position of H1 upon the plane of ethylene molecule. Although, a ubiquitin protein reported previously shows a θ value of 50.3 °,[42] and it is considered to have possible H-π interaction. Therefore, the possible adsorption mechanism might be the interaction between hydrogen from the frameworks and the π electrons present in ethylene, shown in Figure 3.10.

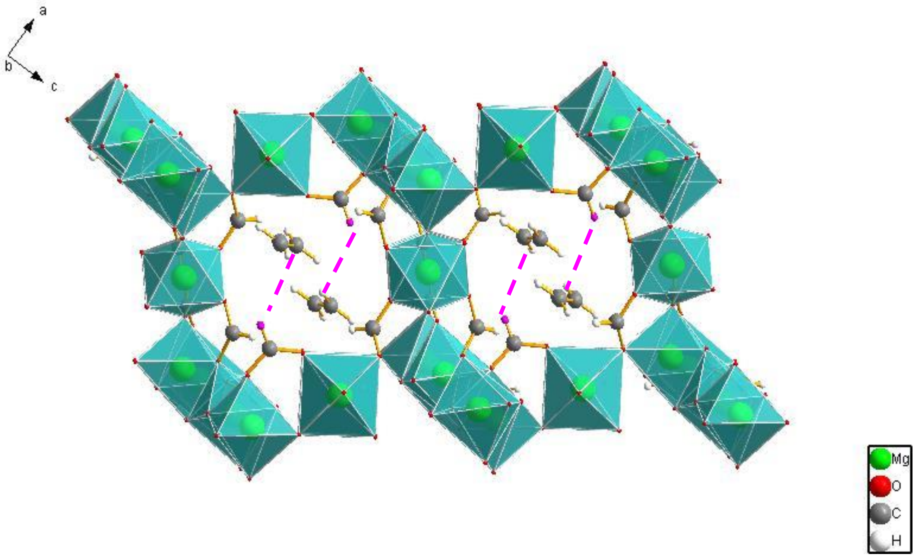

Figure 3.10 - Single crystal structure of ethylene loaded α-Mg formate viewed along b axis. H1 are marked as pink in the structure, and the weak H-π interaction between H1 and adsorbed ethylene is marked as pink dash lines.

3.3.3 C_2D_4 adsorption behavior within CPO-27-M (M = Mg and Zn)

The pXRD results of CPO-27-Mg and Zn before and after activation are shown in Appendix

Figure S3.1 and S3.2 by the end of this chapter, which are all in good agreements with the calculated powder patterns based previously reported structures.[17,19]

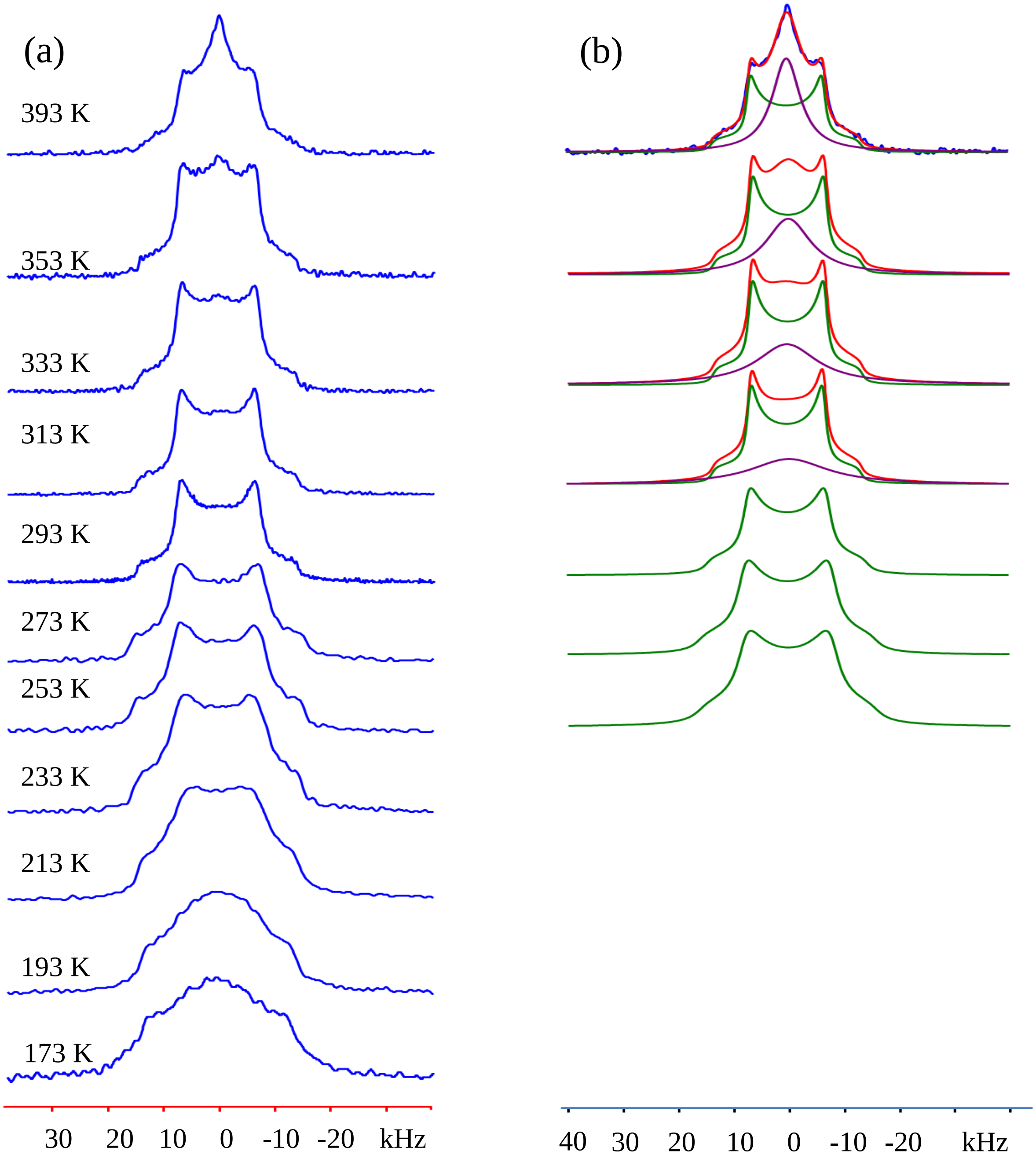

Figure 3.11 - ^{2}H VT experimental (a) and simulated NMR spectra (b) of C_2D_4 loaded in CPO-27-Mg. Green, purple and red spectrum in (b) represent the adsorbed C_2D_4 signal, free C_2D_4 signal, and the summation of the two.

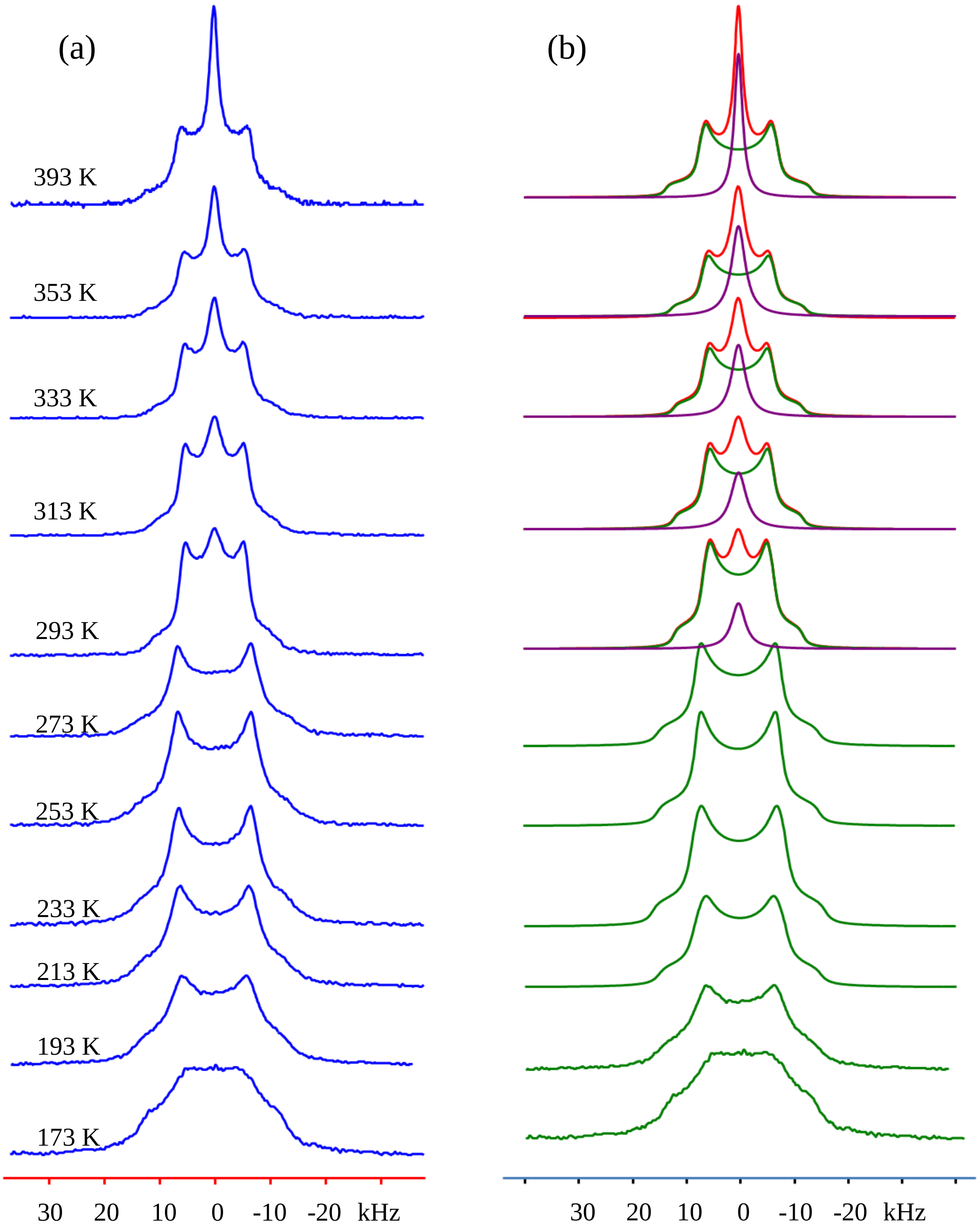

Figure 3.12 - ^{2}H VT experimental (a) and simulated NMR spectra (b) of C_2D_4 loaded in CPO-27-Zn. Green, purple and red spectrum in (b) represent the adsorbed C_2D_4 signal, free C_2D_4 signal, and the summation of these two.

Due to the structural similarity between CPO-27-Mg and Zn, their results are compared and discussed together in this section. The experimental spectra of CPO-27-Mg and Zn are shown in Figure 3.11 and 3.12.

The severe line broadening observed at low temperature in both cases causes difficulty in deriving quadrupolar interaction parameters C_Q and η_Q. Below 233 K for Mg sample and 193 K for Zn sample, typical Pake doublets of ^{2}H NMR are no longer present. Instead, broad featureless spectra take over. Therefore, the lowest temperature from which C_Q values can be derived is at 193 K for CPO-27-Zn, and 233 K for CPO-27-Mg, as summarized in Table 3-4. Above 293 K for Mg sample and 273 K for Zn sample, sharp resonances near 0 ppm appear and become more evident as temperature increases, which are associated with the free ethylene signal.

Table 3-4 Derived QI parameters of C_2D_4 loaded in CPO-27-Mg and CPO-27-Zn

	C_Q of C_2D_4 in Mg sample (kHz)	**η_Q of C_2D_4 in Mg sample**	**C_Q of C_2D_4 in Zn sample (kHz)**	**η_Q of C_2D_4 in Zn sample**
173 K	-	-	-	-
193 K	-	-	20(1)	0.00(1)
213 K	-	-	20(1)	0.00(1)
233 K	21(1)	0.00(1)	21(1)	0.00(1)
253 K	21(1)	0.00(1)	21(1)	0.00(1)
273 K	21(1)	0.00(1)	21(1)	0.00(1)
293 K	19(1)	0.00(1)	16(1)	0.00(1)
313 K	19(1)	0.00(1)	16(1)	0.00(1)
333 K	19(1)	0.00(1)	16(1)	0.00(1)
353 K	19(1)	0.00(1)	16(1)	0.00(1)
393 K	17(1)	0.00(1)	17(1)	0.00(1)

The derived C_Q values for both Mg and Zn spectra are significantly smaller than the reported value for stationary ethylene, which is 230 kHz, indicating that even though the ethylene molecules are less dynamic at low temperature, significant degrees of motion are still present. From room temperature and above, the derived C_Q values for Mg samples are all slightly larger than those of Zn sample, resulting in slightly broader NMR linewidth. In addition, the weight percentage analysis of both Mg and Zn samples from 293 K reveals that though the loading amount in CPO-27-Mg and CPO-27-Zn are the same (both 0.15 C_2D_4/M), the resonance corresponds to free ethylene in CPO-27-Zn weighs much more than in CPO-27-Mg at each temperature, which means that ethylene molecules are more dynamic in Zn sample than in Mg sample, as shown in Table 3-5. Figure 3.13 provides a clearer view of the line width difference by comparing the spectra of C_2D_4 in CPO-27-Mg and Zn obtained at 293 K.

Table 3-5 Weight analysis of the adsorbed and the free C_2D_4 loaded in CPO-27-Mg and Zn from 293 K to 393 K.

	Adsorbed C_2D_4 in CPO-27-Zn (%)	**Free C_2D_4 in CPO-27-Zn (%)**	**Adsorbed C_2D_4 in CPO-27-Mg (%)**	**Free C_2D_4 in CPO-27-Mg (%)**
293 K	91(1)	9(1)	100(1)	-
313 K	89(1)	11(1)	98(1)	2(1)
333 K	85(1)	15(1)	97(1)	3(1)
353 K	80(1)	20(1)	95(1)	5(1)
393 K	66(1)	34(1)	82(1)	18(1)

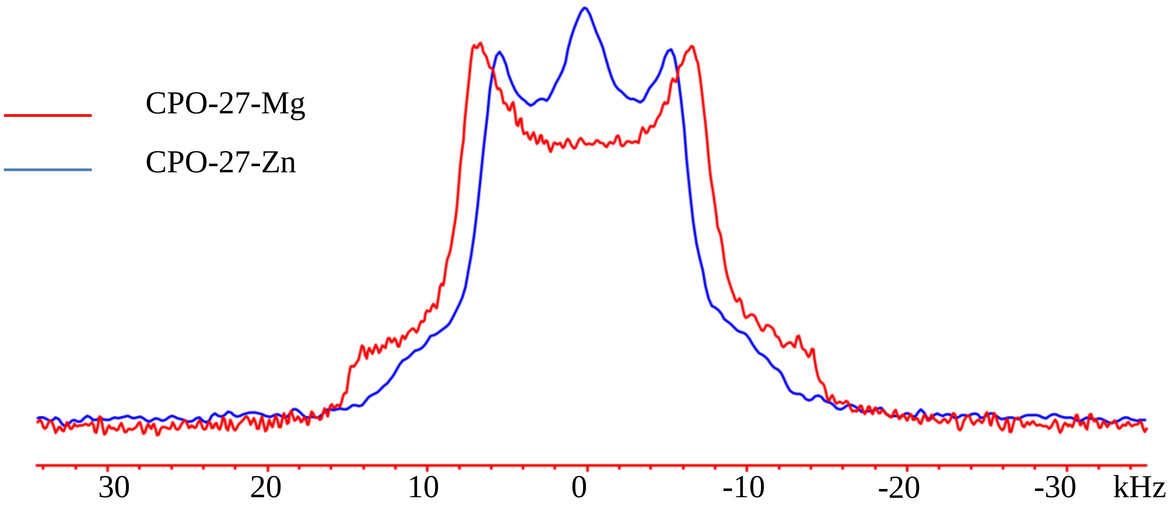

Figure 3.13 - Comparison between ^{2}H NMR spectra of CPO-27-Mg and CPO-27-Zn obtained at 293 K.

Previous studies also reported similar results. The isosteric heat adsorption Q_{st} is commonly used to describe the average enthalpy of the adsorption process for gas molecules.[43] The bigger the absolute value is, the stronger the affinity of the guest species to the host. In the case of ethylene adsorbed in CPO-27-M, the Q_{st} are -42 kJ/mol and -38 kJ/mol for CPO-27-Mg and CPO-27-Zn, indicating the binding strength/affinity between ethylene and the open metal site in weaker in CPO-27-Zn than CPO-27-Mg.[23]

EXPRESS simulation was conducted for both CPO-27-Mg and Zn. The results suggest that ethylene molecules in both CPO-27-Mg and Zn undergo a localized rotation characterized by an angle θ as well as a non-localized inter-sites hopping, characterized by a hopping angle γ. The inter-sites hopping is likely to take place between six open metal sites along the wall of the honeycomb channels in the ab plane. θ is the angle between C-D bond in ethylene and the localized rotation axis; γ is the angle between the localized rotation axis and the non-localized hopping axis. The proposed mechanism is depicted in Figure 3.14. It is worth mentioning that the C_2D_4 molecules are assumed to be adsorbed upon the open metal sites with a side-on fashion, which was previously confirmed by neutron diffraction in the case of CPO-27-Fe and Co.

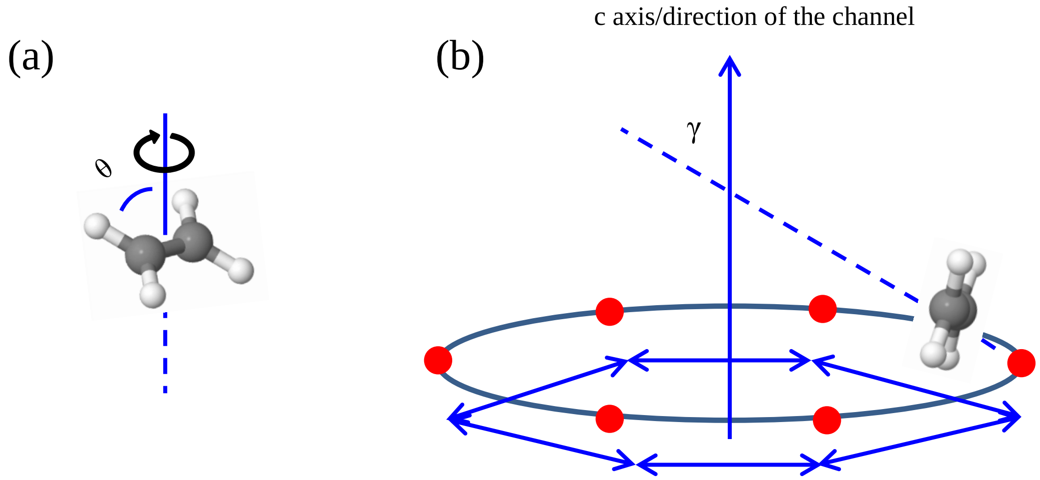

Localized rotation

Non-localized hopping between unsaturated metal sites

Figure 3.14 - Schematic of localized rotation (a) and six-sites hopping (b) of C_2D_4 in CPO-27-M. Red balls in (b) represent the unsaturated metal sites along the wall of the honeycomb channel. The schematic shown here is just an illustration of the inter-sites hopping angle γ. In real crystal structure of CPO-27-M, the six unsaturated metal sites are not in the same ab plane, which will be later discussed and shown in Figure 3.16 (a).

The simulated θ, γ as well as the rate of inter-sites hopping are summarized in Table 3-6. The type of inter-sites hopping is abbreviated as C_n, and n stands for n-sites hopping. Unlike in α-Mg formate, the inter-sites hopping rate of C_2D_4 in CPO-27-M actually falls into an intermediate regime at low temperatures. As the rate of the localized rotation remains in the fast regime throughout the whole VT experiments in both cases, it is not included in the table. The simulated spectra are shown in Figure 3.15a and b.

The rotation angle θ of ethylene adsorbed in both Mg and Zn sample only varies by 2° from 173 K to 393 K, indicating a relatively strong affinity between ethylene and the open metal site that is barely influenced by thermal condition. The inter-sites hopping angle γ in both Mg and Zn samples remains exactly at 72° throughout the VT experiments. The non-90° value of inter-sites hopping suggest that the ethylene molecules are not located right upon the metal centres but slightly tilted toward the centre of the channels in CPO-27-M, as shown in Figure 3.14b.

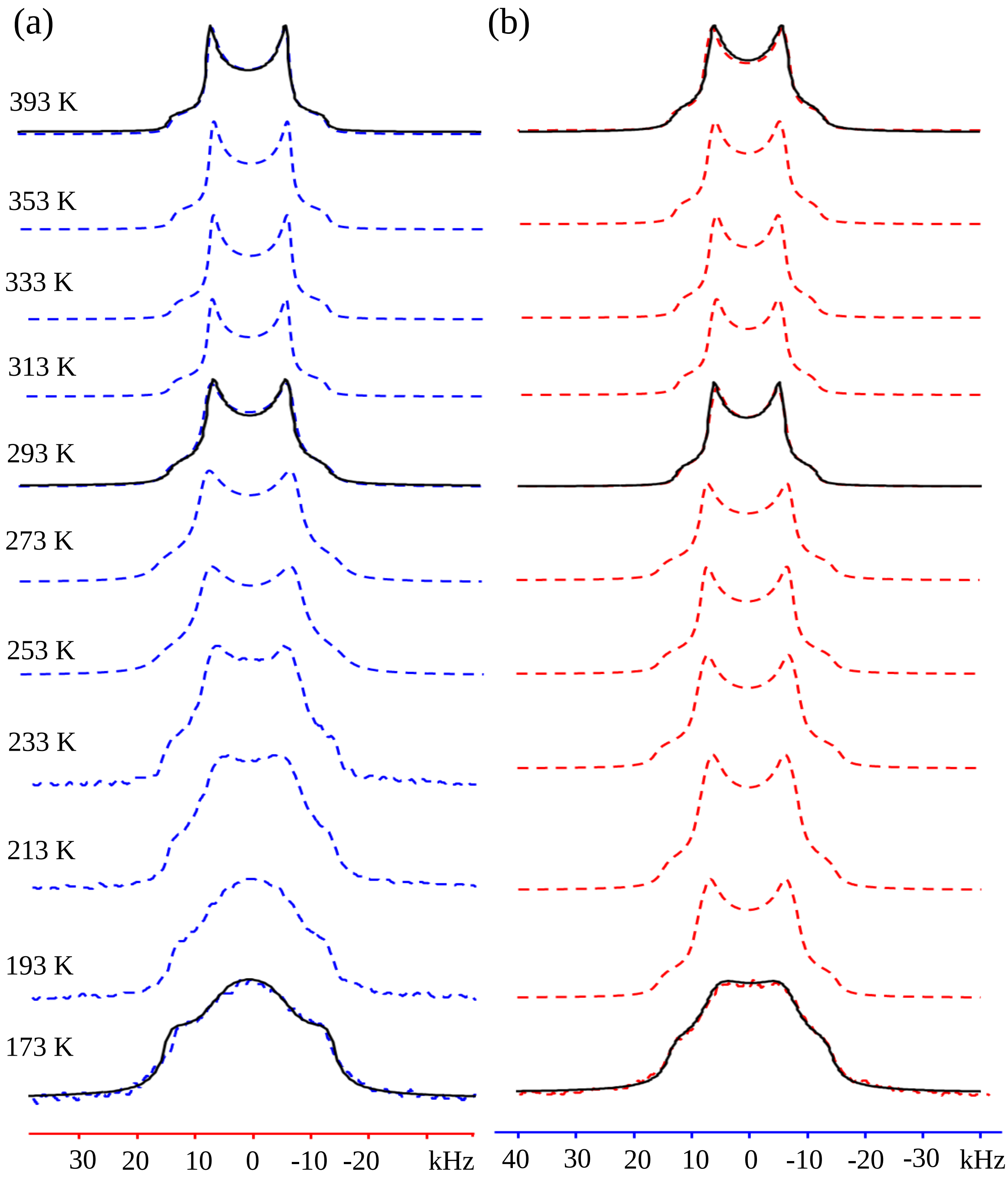

Figure 3.15 – EXPRESS simulation of ^{2}H NMR VT spectra of C_2D_4 loaded in CPO-27-Mg (a) and CPO-27-Zn (b). Blue and red dash spectra are the experimental spectra. For simplicity, only EXPRESS simulated spectra of 173 K, 293 K and 393 K are overlaid as black spectra here.

Table 3-6 EXPRESS simulation results for rotation angle θ, inter-sites hopping angle γ and the rate of the inter-sites hopping from 173 K to 393 K of C_2D_4 loaded in CPO-27-Mg and Zn.

	CPO-27-Zn θ (°)	**CPO-27-Zn γ (°)**	**Inter-sites hopping rate (Hz)**	**CPO-27-Mg θ (°)**	**CPO-27-Mg γ (°)**	**Inter-sites hopping rate (Hz)**
173 K	45(0.5)	72(0.5)	C_3: 5×10^5	46(0.5)	72(0.5)	C_3: 2×10^5
193 K	45(0.5)	72(0.5)	C_6: 5×10^8	46(0.5)	72(0.5)	C_3: 3×10^5
213 K	45(0.5)	72(0.5)	C_6: 5×10^8	46(0.5)	72(0.5)	C_3: 5×10^5
233 K	45(0.5)	72(0.5)	C_6: 5×10^8	46(0.5)	72(0.5)	C_3: 6×10^5
253 K	45(0.5)	72(0.5)	C_6: 5×10^8	45(0.5)	72(0.5)	C_6: 5×10^8
273 K	46(0.5)	72(0.5)	C_6: 5×10^8	45(0.5)	72(0.5)	C_6: 5×10^8
293 K	47(0.5)	72(0.5)	C_6: 5×10^8	45(0.5)	72(0.5)	C_6: 5×10^8
313 K	47(0.5)	72(0.5)	C_6: 5×10^8	45(0.5)	72(0.5)	C_6: 5×10^8
333 K	47(0.5)	72(0.5)	C_6: 5×10^8	46(0.5)	72(0.5)	C_6: 5×10^8
353 K	47(0.5)	72(0.5)	C_6: 5×10^8	46(0.5)	72(0.5)	C_6: 5×10^8
393 K	46.5(0.5)	72(0.5)	C_6: 5×10^8	47(0.5)	72(0.5)	C_6: 5×10^8

The most striking difference between the EXPRESS simulation results of Mg and Zn samples is the inter-sites hopping at low temperature. For CPO-27-Mg sample, from 233 K and below, the severe line broadening of the spectra has made EXPRESS simulation more complicated to perform. The best fit is obtained by a three-fold inter-sites hopping of C_2D_4 within the intermediate regime. Whereas in CPO-27-Zn, the inter-sites hopping of C_2D_4 within intermediate regime can only be obtained at 173 K. It should be noted that the intermediate motion of ethylene molecules is discovered at lower temperature in Zn sample compared to Mg sample, which is in accordance with the fact that ethylene molecules are more mobile in CPO-27-Zn than CPO-27-Mg. The threefold inter-sites hopping along with intermediate jumping rate observed in both samples results from the reduced mobility of C_2D_4 molecules at low temperature. Under this circumstance, the ethylene molecules may hop between the three unsaturated metal sites which are related by a C_3 symmetry element in the same ab plane. In other words, the adsorbed ethylene molecules bypass the adjacent unsaturated metal sites and hop between every other one. The above mentioned schemes are summarized in Figure 3.16.

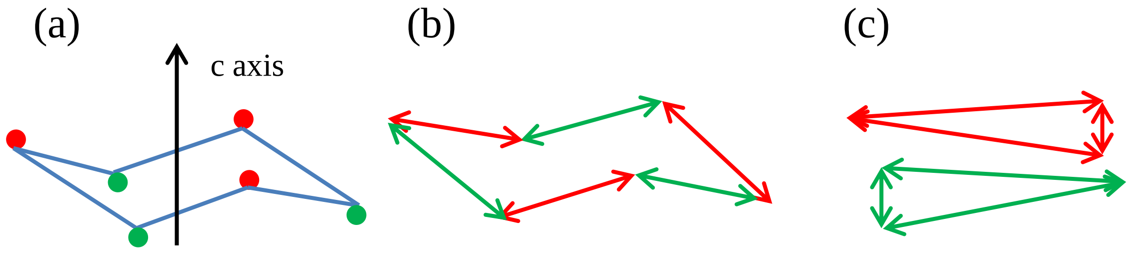

Figure 3.16 - Schematic of six unsaturated metal sites within close proximity in the crystal structure of CPO-27-M (a), non-localized six-sites hopping (b), and possible non-localized three-sites hopping (c). Red and green balls in (a) represent the metals sites in two planes. The six-sites hopping shown in (b) takes place between the six metal adjacent to each other. Therefore, the hopping motion is represented by green and red arrows alternating. The three-sites hopping might take place between three metal sites in the same plane, represented by green or red arrows in the same plane in (c).

3.3.4 Discussion of the different adsorption behaviors of C_2D_4 in α-Mg formate and CPO-27-M

The observed ^{2}H NMR line shapes for C_2D_4 loaded in α-Mg formate and CPO-27-M samples differ from each other greatly, which originates from the different adsorption mechanism in these two types of MOFs. First of all, two distinguished adsorption behaviors are deduced from the two well-defined Pake doublets from C_2D_4 loaded α-Mg formate as discussed earlier in this chapter. One is the combined motion that consists of a localized rotation and a non-localized hopping between the adsorption sites. The other is a simple localized rotation. Whereas in the case of C_2D_4 loaded CPO-27-M, only one adsorption behavior is discovered, which is a similar combined motion that consists of a localized rotation and a simultaneous non-localized hopping. This difference is attributed to the significant different shapes of the channels in these two types of MOFs. For CPO-27-M, the large honeycomb channels allow C_2D_4 molecules rotate upon, and hop between six unsaturated metal sites freely without significant restrictions from the framework. However in α-Mg formate, the very narrow and zigzag shape channels might limit the C_2D_4 molecules' movements to different parts of the channels, giving rise to two types of motions.

The localized rotation angle θ of C_2D_4 in α-Mg formate experiences a more dramatic increment from 173 K to 393 K than in CPO-27-M, which is undoubtedly attributed to the distinct adsorption site in the two MOFs. The electron donating and accepting interaction between the double bond in ethylene and unsaturated metal sites in CPO-27-M is much stronger than the proposed hydrogen-π interaction in α-Mg formate,[42,44] and less dependent on the thermal condition. As a result, the rotation angle of C_2D_4 in α-Mg formate changes from 41 ° to 47 ° during VT experiments, opposite to a 2 ° difference observed in CPO-27-M. In addition, the inter-sites hopping angle γ in these two types of MOFs show very different values as well. In α-Mg formate, ethylene molecules hop between two adsorption sites with an angle of 28 ° during the entire VT experiment, whereas in CPO-27-M, the hopping angle is as big as 72 °. In the structure of CPO-27-M, the unsaturated metal sites are all pointing towards the channels, and ethylene molecules locate slightly off-centered upon the metal sites, resulting in a large hopping angle, as shown in Figure 3.12 b. The small hopping angle of ethylene in α-Mg formate is most likely due to the restriction of the narrow and zigzag-shaped channels, which do not provide enough space for ethylene molecules to undergo inter-sites hopping between two adsorption sites further away from each other.

3.3.5 Discussion on the different adsorption behaviors of C_2D_4 and $^{13}CO_2$ in α-Mg formate.

As introduced in chapter 2, ^{13}C NMR was used to examine the CO_2 adsorption behavior in α-Mg formate. In this chapter, ^2H NMR instead of ^{13}C NMR was performed to examine the ethylene adsorption behavior in this type of MOF, which is due to the difficulty in interpreting ^{13}C spectra. According to EXPRESS simulation, the adsorbed C_2D_4 and $^{13}CO_2$ molecules in α-Mg formate both undergo two types of motion: 1. a combined motion consisting of a localized rotation and a non-localized inter-sites hopping; 2. a simple localized rotation. The difference between these two cases is the different thermal condition at which motion 2 appears. Among the adsorbed $^{13}CO_2$ molecules, motion 2 cannot be observed until 313 K, which can be ascribed to the structural change occurring at high temperature, as proposed in chapter 2; Among the adsorbed C_2D_4, motion 2 is present during the entire VT experiment from 173 K to 373 K, which is speculated to originate from two types of ethylene molecules that locate at different positions of the channels. The ethylene molecules that only obey a localized rotation might reside at the narrower part of the channel that does not have enough space to perform inter-sites hopping. Therefore those ethylene molecules only follow motion 2. On the other hand, the ethylene molecules observed by single crystal X-ray analysis all lie along the direction of the channels, which provide them plenty of space to perform the inter-sites hopping and undergo the combined motion (motion 1). Although both motion 1 and 2 and be derived from C_2D_4 and $^{13}CO_2$ adsorbed in α-Mg formate, their origins are different.

One confusing result is that the ^{13}C spectra of $^{13}CO_2$ adsorbed in α-Mg formate are abnormally broader from 333 K and above, but ^2H spectra of C_2D_4 are not. If the line broadening observed in ^{13}C spectra is associated with structural change as discussed in chapter 2, a similar line broadening at higher temperature is anticipated in the ^2H spectrum as well. So far, the experimental results seem to be contradictory to our speculation. Actually, the localized rotation angle θ of $^{13}CO_2$ and C_2D_4 at higher temperature might shed some light on this issue. At 293 K, the rotation angle θ is 49 ° and 45 ° for $^{13}CO_2$ and C_2D_4, respectively, indicating a larger active area for $^{13}CO_2$ molecules in comparison with ethylene. This is most likely due to the smaller kinetic size as well as the weaker affinity to the adsorption sites of $^{13}CO_2$ molecules. As temperature increases from 313 K to 373 K, the θ of $^{13}CO_2$ drops by 2 ° while increases by 1 ° for ethylene. Therefore, it is possible that the subtle structural change does not hinder the movement of ethylene molecules due to the smaller area the localized rotation takes place than that of $^{13}CO_2$.

Inter-sites hopping angle γ also shows interesting difference in the two cases. γ of $^{13}CO_2$ molecules adsorbed in α-Mg formate increases from 23 ° to 45 ° while the γ of ethylene remains at 28 ° during the entire VT experiments. As discussed in chapter 2, this increasing value of γ observed in $^{13}CO_2$ is due to the molecular hopping between two hydrogen sites more distant from each other. The inter-sites hopping of ethylene molecules is predicted to occur between two equivalent sites related by a twofold screw axis along b axis. There are two possible explanations regarding this issue. First, the binding strength between the framework and the adsorbed ethylene molecules is much stronger than that of $^{13}CO_2$, giving rise to an inter-sites hopping between two fixed adsorption sites. Secondly, due to the large kinetic size of ethylene and the zigzag shape of the channels, it is possible that the inter-sites hopping is restricted between two specific adsorption sites throughout the entire VT experiment. Consequently, the inter-sites hopping angle is fixed to 28 °.

3.4 Conclusion

The ethylene adsorption behaviors through a wide temperature range in CPO-27-M (M = Zn and Mg) and α-Mg formate were successfully resolved by means of ^{2}H SSNMR VT experiments.

In α-Mg formate, two independent adsorption behaviors are observed, reflected by two well-defined Pake doublets in NMR spectra. The majority of the ethylene molecules undergo a localized rotation and simultaneously non-localized twofold inter-sites hopping, while the minorities undergo a localized rotation, no inter-sites hopping is observed. The weight analysis of the NMR spectra reveals a ratio of 9:1 between the former and the latter adsorption behaviors. The single crystal X-ray analysis suggests only one type of ethylene present in the system, which might be due to the small amount of the second type of ethylene.

In CPO-27-M, both Mg and Zn samples exhibit only one type of motion: a rapid and localized rotation upon the unsaturated metal sites with a simultaneous inter-sites hopping between different metal centres. A three-sites hopping motion instead of six-sites within intermediate regime is deduced from 233 K and below for the Mg sample and only at 173 K for the Zn sample. These results are in accordance with the previously reported isosteric adsorption heat of CPO-27-Mg and Zn, confirming that the affinity between the Mg sample and ethylene molecules is strong than that of Zn sample.

The difference in adsorption behavior between the two types of MOFs is the result of their structural difference. The narrow and the zigzag shape channel in α-Mg formate is responsible for the two distinct adsorption behaviors. Whereas the large honeycomb channel in CPO-27-M give rise to a straightforward adsorption behavior.

3.5 Bibliography

(1) Xie, T.; McAuley, K. B.; Hsu, J. C. C.; Bacon, D. W. *Industrial & Engineering Chemistry Research* **1994**, *33*, 449.

(2) Rebsdat, S.; Mayer, D. In *Ullmann's Encyclopedia of Industrial Chemistry*; Wiley-VCH Verlag GmbH & Co. KGaA: 2000.

(3) Lelièvre, J.-M.; Latchè, A.; Jones, B.; Bouzayen, M.; Pech, J.-C. *Physiologia Plantarum* **1997**, *101*, 727.

(4) Aguado, S.; Bergeret, G.; Daniel, C.; Farrusseng, D. *Journal of the American Chemical Society* **2012**, *134*, 14635.

(5) Triebe, R. W.; Tezel, F. H.; Khulbe, K. C. *Gas Separation & Purification* **1996**, *10*, 81.

(6) Gücüyener, C.; van den Bergh, J.; Gascon, J.; Kapteijn, F. *Journal of the American Chemical Society* **2010**, *132*, 17704.

(7) Bux, H.; Chmelik, C.; Krishna, R.; Caro, J. *Journal of Membrane Science* **2011**, *369*, 284.

(8) Böhme, U.; Barth, B.; Paula, C.; Kuhnt, A.; Schwieger, W.; Mundstock, A.; Caro, J.; Hartmann, M. *Langmuir* **2013**, *29*, 8592.

(9) Herm, Z. R.; Bloch, E. D.; Long, J. R. *Chemistry of Materials* **2014**, *26*, 323.

(10) Czaja, A.; Leung, E.; Trukhan, N.; Müller, U. In *Metal-Organic Frameworks*; Wiley-VCH Verlag GmbH & Co. KGaA: 2011, p 337.

(11) Fischer, M.; Hoffmann, F.; Fröba, M. *ChemPhysChem* **2010**, *11*, 2220.

(12) Samsonenko, D. G.; Kim, H.; Sun, Y.; Kim, G.-H.; Lee, H.-S.; Kim, K. *Chemistry – An Asian Journal* **2007**, *2*, 484.

(13) Britt, D.; Furukawa, H.; Wang, B.; Glover, T. G.; Yaghi, O. M. *Proceedings of the National Academy of Sciences* **2009**, *106*, 20637.

(14) Valenzano, L.; Civalleri, B.; Chavan, S.; Palomino, G. T.; Areán, C. O.; Bordiga, S. *The Journal of Physical Chemistry C* **2010**, *114*, 11185.

(15) Grant Glover, T.; Peterson, G. W.; Schindler, B. J.; Britt, D.; Yaghi, O. *Chemical Engineering Science* **2011**, *66*, 163.

(16) Poloni, R.; Lee, K.; Berger, R. F.; Smit, B.; Neaton, J. B. *The Journal of Physical Chemistry Letters* **2014**, *5*, 861.

(17) Dietzel, P. D. C.; Blom, R.; Fjellvåg, H. *European Journal of Inorganic Chemistry* **2008**, *2008*, 3624.

(18) Dietzel, P. D. C.; Johnsen, R. E.; Fjellvag, H.; Bordiga, S.; Groppo, E.; Chavan, S.; Blom, R. *Chemical Communications* **2008**, 5125.

(19) Dietzel, P. D. C.; Johnsen, R. E.; Blom, R.; Fjellvåg, H. *Chemistry – A European Journal* **2008**, *14*, 2389.

(20) Rosnes, M. H.; Opitz, M.; Frontzek, M.; Lohstroh, W.; Embs, J. P.; Georgiev, P. A.; Dietzel, P. D. C. *Journal of Materials Chemistry A* **2015**, *3*, 4827.

(21) Bao, Z.; Alnemrat, S.; Yu, L.; Vasiliev, I.; Ren, Q.; Lu, X.; Deng, S. *Langmuir* **2011**, *27*, 13554.

(22) Bloch, E. D.; Queen, W. L.; Krishna, R.; Zadrozny, J. M.; Brown, C. M.; Long, J. R. *Science* **2012**, *335*, 1606.

(23) Geier, S. J.; Mason, J. A.; Bloch, E. D.; Queen, W. L.; Hudson, M. R.; Brown, C. M.; Long, J. R. *Chemical Science* **2013**, *4*, 2054.

(24) Vold, R. L.; Hoatson, G. L. *Journal of Magnetic Resonance* **2009**, *198*, 57.

(25) Kolokolov, D. I.; Stepanov, A. G.; Guillerm, V.; Serre, C.; Frick, B.; Jobic, H. *The Journal of Physical Chemistry C* **2012**, *116*, 12131.

(26) Balkus, K. J.; Ly, K. T. *Journal of Chemical Education* **1991**, *68*, 875.

(27) Boddenberg, B.; Burmeister, R. *Zeolites* **1988**, *8*, 480.

(28) Gladden, L. F.; Sousa-Gonçalves, J. A.; Alexander, P. *The Journal of Physical Chemistry B* **1997**, *101*, 10121.

(29) Bae, T.-H.; Hudson, M. R.; Mason, J. A.; Queen, W. L.; Dutton, J. J.; Sumida, K.; Micklash, K. J.; Kaye, S. S.; Brown, C. M.; Long, J. R. *Energy & Environmental Science* **2013**, *6*, 128.

(30) Wang, W. D.; Lucier, B. E. G.; Terskikh, V. V.; Wang, W.; Huang, Y. *The Journal of Physical Chemistry Letters* **2014**, *5*, 3360.

(31) *NMR Solvent Data Chart* *http://www2.chem.umd.edu/nmr/reference/isotope_solvent.pdf* *(Accessed on July 22, 2015.).*

(32) David R. Lide, J. In *critical evaluation of the chemical and physical structural information* The United States of America, 1973, p 577.

(33) Bruker-AXS, SAINT version 2013.8, 2013, Bruker-AXS, Madison, WI 53711, USA

(34) Bruker-AXS, SADABS version 2012.1, 2012, Bruker-AXS, Madison, WI 53711, USA

(35) Xu, J.; Terskikh, V. V.; Chu, Y.; Zheng, A.; Huang, Y. *Chemistry of Materials* **2015**, *27*, 3306.

(36) Sheldrick, G. *Acta Crystallographica Section A* **2015**, *71*, 3.

(37) Gabe, E. J.; Le Page, Y.; Charland, J.-P.; Lee, F. L.; White, P. S. *Journal of Applied Crystallography* **1989**, *22*, 384.

(38) Scheiner, S. *International Journal of Quantum Chemistry* **2010**, *110*, 2775.

(39) Nishio, M. *Crystengcomm* **2004**, *6*, 130.

(40) Sundararajan, K.; Sankaran, K.; Viswanathan, K. S.; Kulkarni, A. D.; Gadre, S. R. *The Journal of Physical Chemistry A* **2002**, *106*, 1504.

(41) Sundararajan, K.; Viswanathan, K. S.; Kulkarni, A. D.; Gadre, S. R. *Journal of Molecular Structure* **2002**, *613*, 209.

(42) Plevin, M. J.; Bryce, D. L.; Boisbouvier, J. *Nat Chem* **2010**, *2*, 466.

(43) Sumida, K.; Rogow, D. L.; Mason, J. A.; McDonald, T. M.; Bloch, E. D.; Herm, Z. R.; Bae, T.-H.; Long, J. R. *Chemical Reviews* **2011**, *112*, 724.

(44) Premkumar, J. R.; Vijay, D.; Sastry, G. N. *Dalton Transactions* **2012**, *41*, 4965.

3.6 Appendix

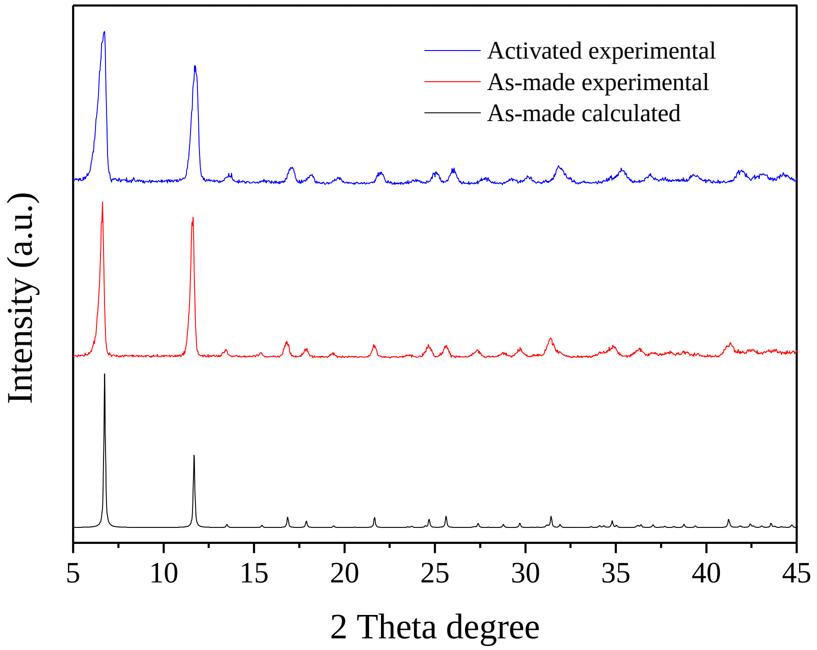

Figure S3.1 - Calculated and experimental pXRD results of as-made and activated CPO-27-Zn

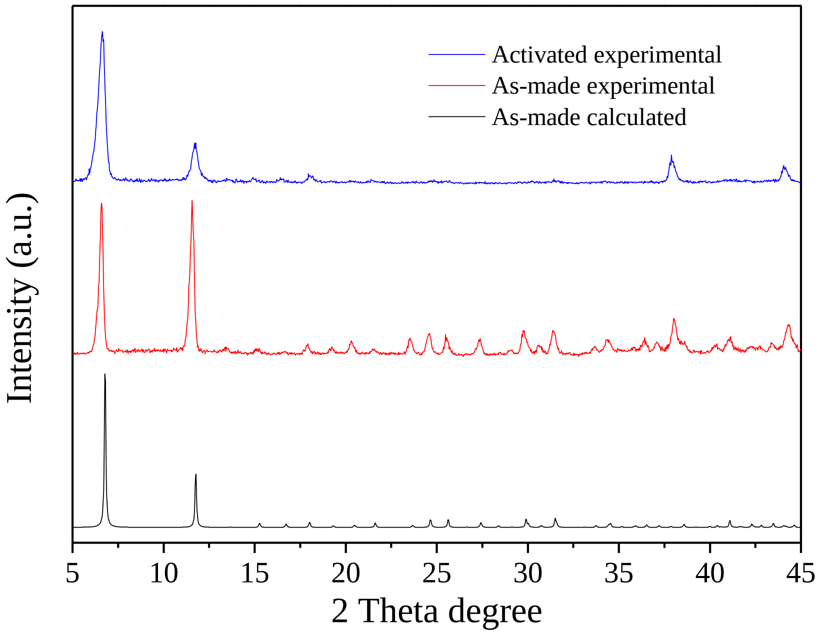

Figure S3.2 - Calculated and experimental pXRD results of as-made and activated CPO-27-Mg

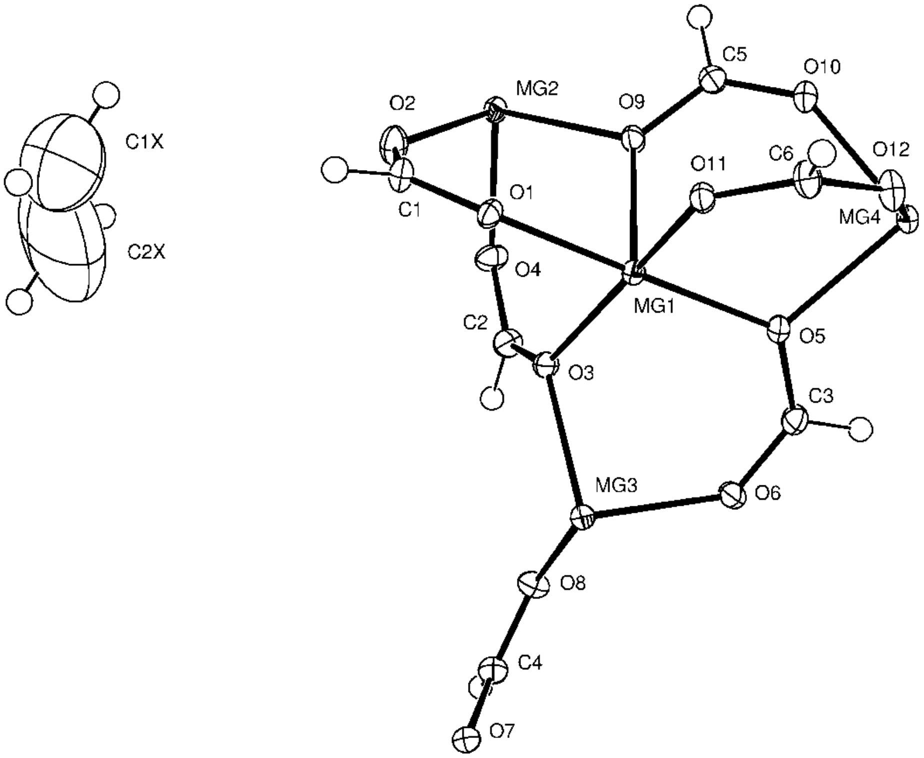

Figure S3.3 - ORTEP drawing of asymmetric unit showing naming and numbering scheme. Ellipsoids are at the 50% probability level and hydrogen and deuterium atoms were drawn with arbitrary radii for clarity.

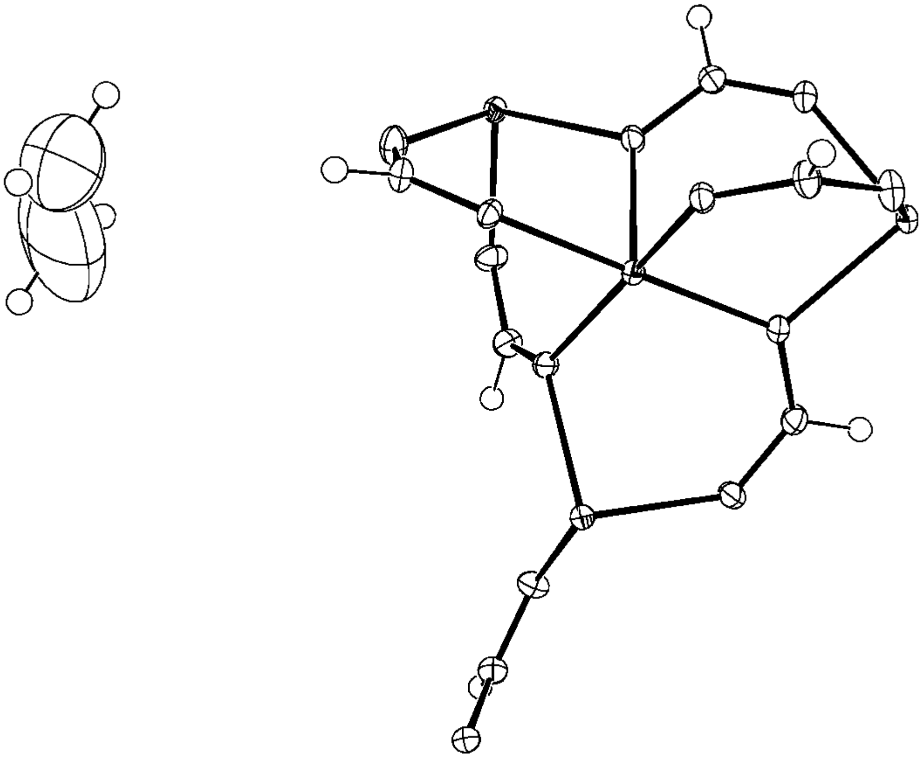

Figure S3.4 - ORTEP drawing of asymmetric unit. Ellipsoids are at the 50% probability level and hydrogen and deuterium atoms were drawn with arbitrary radii for clarity.

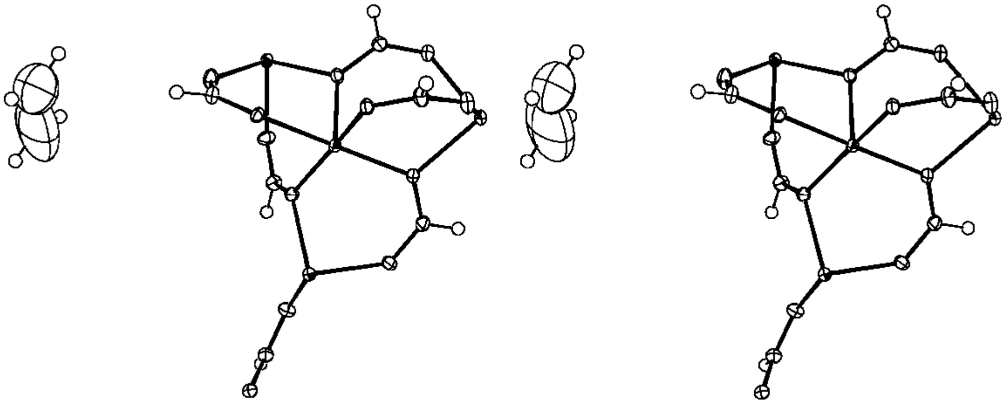

Figure S3.5 - Stereoscopic ORTEP drawing of C_2D_4 loaded α-Mg formate asymmetric unit. Ellipsoids are at the 50% probability level and hydrogen deuterium atoms were drawn with arbitrary radii for clarity.

Table S3.1 - Summary of crystal data for C_2D_4 loaded α-Mg formate

Formula	$C_8H_6D_4Mg_3O_{12}$
Formula Weight (*g/mol*)	375.11
Crystal Dimensions (*mm*)	0.163 × 0.103 × 0.041
Crystal Color and Habit	colourless plate
Crystal System	monoclinic
Space Group	$P\ 2_1/n$
Temperature, K	110
a, Å	11.310(4)
b, Å	9.801(4)
c, Å	14.518(6)
α, °	90
β, °	91.264(16)
γ, °	90
V, $Å^3$	1609.0(11)
Number of reflections to determine final unit cell	9898
Min and Max 2θ for cell determination, °	5.02, 63.04
Z	4
F(000)	760
ρ (*g/cm*)	1.549
λ, Å, (MoKα)	0.71073
μ, (cm^{-1})	0.244

Diffractometer Type	Bruker Kappa Axis Apex2
Scan Type(s)	phi and omega scans
Max 2θ for data collection, °	63.536
Measured fraction of data	0.997
Number of reflections measured	74782
Unique reflections measured	5393
R_{merge}	0.0862
Number of reflections included in refinement	5393
Cut off Threshold Expression	I > 2sigma(I)
Structure refined using	full matrix least-squares using F^2
Weighting Scheme	$w=1/[\mathrm{sigma}^2(Fo^2)+(0.0454P)^2+0.7460P]$ where $P=(Fo^2+2Fc^2)/3$
Number of parameters in least-squares	211
R_1	0.0432
wR_2	0.0941
R_1 (all data)	0.0757
wR_2 (all data)	0.1067
GOF	1.037
Maximum shift/error	0.000
Min & Max peak heights on final ΔF Map (e^-/Å)	-0.469, 0.506

Where:

$R_1 = \Sigma(|F_o| - |F_c|) / \Sigma F_o$

$wR_2 = [\Sigma(w(F_o^2 - F_c^2)^2) / \Sigma(w F_o^4)]^{½}$

$$GOF = [\Sigma(w(F_o^2 - F_c^2)^2) / (\text{No. of reflns. - No. of params.})]^{½}$$

Table S3.2 - Atomic coordinates for C_2D_4 loaded α-Mg formate

Atom	x	y	z	$U_{iso/equiv}$
Mg1	0.25633(4)	0.41882(5)	0.63473(4)	0.00991(12)
Mg2	0.0000	0.5000	0.5000	0.01136(16)
Mg3	0.26112(5)	0.10784(5)	0.68900(4)	0.01041(12)
Mg4	0.5000	0.5000	0.5000	0.01158(16)
O1	0.13009(9)	0.50217(11)	0.72091(8)	0.0115(2)
O2	-0.03826(10)	0.50185(13)	0.63803(8)	0.0173(3)
C1	0.01853(14)	0.51375(17)	0.71127(11)	0.0139(3)
O3	0.15647(9)	0.24122(11)	0.61083(8)	0.0117(2)
O4	0.01768(10)	0.29184(12)	0.50366(8)	0.0160(2)
C2	0.07599(14)	0.21054(17)	0.55117(11)	0.0145(3)
O5	0.39836(9)	0.34587(11)	0.56139(8)	0.0122(2)
O6	0.38823(10)	0.12255(11)	0.59381(8)	0.0143(2)
C3	0.43040(14)	0.22170(16)	0.55296(11)	0.0142(3)
O7	0.19013(9)	-0.20357(11)	0.75380(7)	0.0118(2)
O8	0.18553(10)	-0.06174(11)	0.63271(8)	0.0149(2)
C4	0.16773(14)	-0.17398(16)	0.66942(11)	0.0133(3)
O9	0.18346(9)	0.52502(11)	0.52519(8)	0.0122(2)
O10	0.35044(10)	0.60747(12)	0.46679(8)	0.0162(2)
C5	0.24197(14)	0.60126(16)	0.47062(12)	0.0146(3)
O11	0.34926(9)	0.57971(11)	0.69705(8)	0.0119(2)

O12	0.51831(10)	0.60516(12)	0.62217(8)	0.0170(3)
C6	0.45191(14)	0.62985(17)	0.68598(12)	0.0149(3)
C1X	-0.2822(7)	0.5031(9)	0.8497(8)	0.212(5)
D1	-0.2640	0.5804	0.8131	0.317
D2	-0.2802	0.5105	0.9149	0.317
C2X	-0.3093(10)	0.3810(11)	0.8143(7)	0.257(6)
D3	-0.3115	0.3731	0.7490	0.385
D4	-0.3274	0.3043	0.8514	0.385
H1	-0.0249	0.5332	0.7650	0.017
H2	0.0595	0.1163	0.5426	0.017
H3	0.4923	0.2036	0.5115	0.017
H4	0.1346	-0.2439	0.6316	0.016
H5	0.1976	0.6579	0.4295	0.018
H6	0.4799	0.6924	0.7315	0.018

Table S3.3 - Anisotropic displacement parameters for C_2D_4 loaded α-Mg formate

Atom	u^{11}	u^{22}	u^{33}	u^{12}	u^{13}	u^{23}
Mg1	0.0084(2)	0.0102(2)	0.0111(3)	0.00008(18)	0.00063(19)	0.0001(2)
Mg2	0.0082(3)	0.0130(4)	0.0129(4)	-0.0002(3)	-0.0003(3)	0.0011(3)
Mg3	0.0097(2)	0.0103(2)	0.0113(3)	-0.00001(19)	0.00072(19)	0.0008(2)
Mg4	0.0090(3)	0.0127(4)	0.0131(4)	-0.0008(3)	0.0026(3)	0.0007(3)
O1	0.0081(5)	0.0122(5)	0.0141(5)	0.0008(4)	-0.0001(4)	-0.0010(4)
O2	0.0109(5)	0.0266(7)	0.0145(6)	-0.0007(5)	-0.0005(4)	0.0003(5)
C1	0.0101(7)	0.0176(8)	0.0141(8)	0.0003(6)	0.0024(6)	-0.0009(6)
O3	0.0097(5)	0.0114(5)	0.0138(5)	-0.0008(4)	-0.0012(4)	0.0006(4)
O4	0.0139(5)	0.0144(6)	0.0195(6)	0.0010(4)	-0.0055(5)	0.0010(5)
C2	0.0133(7)	0.0125(7)	0.0176(8)	-0.0016(6)	-0.0020(6)	-0.0017(6)
O5	0.0097(5)	0.0123(5)	0.0148(6)	0.0002(4)	0.0029(4)	0.0004(4)
O6	0.0155(5)	0.0109(5)	0.0166(6)	0.0000(4)	0.0045(4)	0.0018(4)
C3	0.0126(7)	0.0141(8)	0.0161(8)	0.0012(6)	0.0033(6)	-0.0014(6)
O7	0.0126(5)	0.0114(5)	0.0114(5)	0.0007(4)	-0.0004(4)	0.0000(4)
O8	0.0176(6)	0.0123(5)	0.0147(6)	-0.0017(4)	-0.0014(4)	0.0016(4)
C4	0.0148(7)	0.0116(7)	0.0133(8)	-0.0003(6)	-0.0004(6)	-0.0013(6)
O9	0.0093(5)	0.0141(5)	0.0132(5)	-0.0014(4)	0.0001(4)	0.0024(4)
O10	0.0099(5)	0.0176(6)	0.0211(6)	-0.0004(4)	0.0026(4)	0.0035(5)
C5	0.0124(7)	0.0149(8)	0.0165(8)	0.0000(6)	-0.0005(6)	0.0031(6)
O11	0.0099(5)	0.0122(5)	0.0136(5)	-0.0014(4)	0.0017(4)	-0.0009(4)

O12	0.0126(5)	0.0219(6)	0.0165(6)	-0.0041(4)	0.0040(4)	-0.0021(5)
C6	0.0121(7)	0.0182(8)	0.0145(8)	-0.0039(6)	0.0006(6)	-0.0019(6)
C1X	0.107(5)	0.207(9)	0.324(14)	0.049(6)	0.078(7)	0.114(9)
C2X	0.296(13)	0.261(12)	0.221(10)	-0.005(10)	0.177(10)	0.025(9)

Table S3.4 - Bond lengths for C$_2$D$_4$ loaded α-Mg formate

Mg1-O9	2.0576(13)	Mg4-O5^4	2.1079(12)
Mg1-O5	2.0738(13)	Mg4-Mg1^4	3.5060(12)
Mg1-O1	2.0857(13)	O1-C1	1.2715(19)
Mg1-O11	2.0900(13)	O1-Mg3^1	2.0558(13)
Mg1-O7^1	2.0932(13)	O2-C1	1.236(2)
Mg1-O3	2.0996(13)	C1-H1	0.9500
Mg1-Mg3	3.1483(14)	O3-C2	1.2785(19)
Mg1-Mg3^1	3.1689(12)	O4-C2	1.235(2)
Mg1-Mg4	3.5060(12)	C2-H2	0.9500
Mg1-Mg2	3.5516(12)	O5-C3	1.2765(19)
Mg2-O4	2.0506(14)	O6-C3	1.2394(19)
Mg2-O4^2	2.0506(14)	C3-H3	0.9500
Mg2-O2^2	2.0594(14)	O7-C4	1.279(2)
Mg2-O2	2.0595(14)	O7-Mg1^3	2.0932(13)
Mg2-O9^2	2.1132(13)	O7-Mg3^3	2.0952(14)
Mg2-O9	2.1132(13)	O8-C4	1.241(2)
Mg2-Mg1^2	3.5516(12)	C4-H4	0.9500
Mg3-O6	2.0212(14)	O9-C5	1.2834(19)
Mg3-O8	2.0323(14)	O10-C5	1.231(2)
Mg3-O1^3	2.0558(13)	C5-H5	0.9500
Mg3-O3	2.0829(13)	O11-C6	1.2741(19)

Mg3-O7[1]	2.0952(14)	O11-Mg3[1]	2.1125(14)
Mg3-O11[3]	2.1125(14)	O12-C6	1.229(2)
Mg3-Mg1[3]	3.1690(12)	C6-H6	0.9500
Mg4-O10	2.0413(13)	C1X-C2X	1.335(12)
Mg4-O10[4]	2.0414(13)	C1X-D1	0.9500
Mg4-O12[4]	2.0579(13)	C1X-D2	0.9500
Mg4-O12	2.0579(13)	C2X-D3	0.9501
Mg4-O5	2.1079(12)	C2X-D4	0.9500

1. -x+1/2, y+1/2,1+ -z+1/2
2. -x,1+ -y,1+ -z
3. -x+1/2,-1+ y+1/2,1+ -z+1/2
4. 1-x,1+ -y,1+ -z

Table S3.5 - Bond angles for C_2D_4 loaded α-Mg formate

O9-Mg1-O5	94.54(5)	O8-Mg3-Mg1	133.34(5)
O9-Mg1-O1	89.87(5)	O1^3-Mg3-Mg1	130.82(4)
O5-Mg1-O1	172.43(5)	O3-Mg3-Mg1	41.37(3)
O9-Mg1-O11	98.16(5)	O7^1-Mg3-Mg1	41.24(4)
O5-Mg1-O11	95.42(5)	O11^3-Mg3-Mg1	108.37(4)
O1-Mg1-O11	77.83(5)	O6-Mg3-Mg1^3	130.67(4)
O9-Mg1-O7^1	172.55(5)	O8-Mg3-Mg1^3	79.25(5)
O5-Mg1-O7^1	89.15(5)	O1^3-Mg3-Mg1^3	40.43(4)
O1-Mg1-O7^1	87.18(5)	O3-Mg3-Mg1^3	139.65(4)
O11-Mg1-O7^1	87.91(5)	O7^1-Mg3-Mg1^3	102.49(5)
O9-Mg1-O3	94.98(5)	O11^3-Mg3-Mg1^3	40.79(3)
O5-Mg1-O3	92.82(5)	Mg1-Mg3-Mg1^3	140.09(2)
O1-Mg1-O3	92.92(5)	O10-Mg4-O10^4	180.0
O11-Mg1-O3	163.86(5)	O10-Mg4-O12^4	89.30(5)
O7^1-Mg1-O3	78.35(5)	O10^4-Mg4-O12^4	90.70(5)
O9-Mg1-Mg3	133.44(4)	O10-Mg4-O12	90.70(5)
O5-Mg1-Mg3	77.61(4)	O10^4-Mg4-O12	89.30(5)
O1-Mg1-Mg3	103.73(4)	O12^4-Mg4-O12	180.0
O11-Mg1-Mg3	128.05(4)	O10-Mg4-O5	90.74(5)
O7^1-Mg1-Mg3	41.29(3)	O10^4-Mg4-O5	89.26(5)
O3-Mg1-Mg3	40.97(4)	O12^4-Mg4-O5	87.71(5)

O9-Mg1-Mg3^1	107.30(5)	O12-Mg4-O5	92.29(5)
O5-Mg1-Mg3^1	132.76(4)	O10-Mg4-O5^4	89.26(5)
O1-Mg1-Mg3^1	39.73(3)	O10^4-Mg4-O5^4	90.74(5)
O11-Mg1-Mg3^1	41.32(4)	O12^4-Mg4-O5^4	92.29(5)
O7^1-Mg1-Mg3^1	74.50(5)	O12-Mg4-O5^4	87.71(5)
O3-Mg1-Mg3^1	125.12(4)	O5-Mg4-O5^4	180.00(4)
Mg3-Mg1-Mg3^1	111.40(3)	O10-Mg4-Mg1^4	114.12(4)
O9-Mg1-Mg4	76.14(4)	O10^4-Mg4-Mg1^4	65.88(4)
O5-Mg1-Mg4	33.33(4)	O12^4-Mg4-Mg1^4	72.43(4)
O1-Mg1-Mg4	143.39(4)	O12-Mg4-Mg1^4	107.57(4)
O11-Mg1-Mg4	71.11(4)	O5-Mg4-Mg1^4	147.28(3)
O7^1-Mg1-Mg4	110.11(4)	O5^4-Mg4-Mg1^4	32.72(3)
O3-Mg1-Mg4	121.50(4)	O10-Mg4-Mg1	65.88(4)
Mg3-Mg1-Mg4	110.484(19)	O10^4-Mg4-Mg1	114.12(4)
Mg3^1-Mg1-Mg4	112.43(3)	O12^4-Mg4-Mg1	107.57(4)
O9-Mg1-Mg2	32.10(3)	O12-Mg4-Mg1	72.43(4)
O5-Mg1-Mg2	115.25(5)	O5-Mg4-Mg1	32.72(3)
O1-Mg1-Mg2	71.42(4)	O5^4-Mg4-Mg1	147.28(3)
O11-Mg1-Mg2	117.78(4)	Mg1^4-Mg4-Mg1	180.0
O7^1-Mg1-Mg2	140.62(4)	C1-O1-Mg3^1	127.13(10)
O3-Mg1-Mg2	70.44(4)	C1-O1-Mg1	131.28(11)
Mg3-Mg1-Mg2	111.349(19)	Mg3^1-O1-Mg1	99.84(6)

Mg3^{1}-Mg1-Mg2	104.43(3)	C1-O2-Mg2	136.20(11)
Mg4-Mg1-Mg2	106.50(3)	O2-C1-O1	125.59(15)
O4-Mg2-O4^{2}	180.0	O2-C1-H1	117.2
O4-Mg2-O2^{2}	89.66(5)	O1-C1-H1	117.2
O4^{2}-Mg2-O2^{2}	90.34(5)	C2-O3-Mg3	127.52(11)
O4-Mg2-O2	90.34(5)	C2-O3-Mg1	132.79(11)
O4^{2}-Mg2-O2	89.66(5)	Mg3-O3-Mg1	97.65(5)
O2^{2}-Mg2-O2	180.0	C2-O4-Mg2	134.98(11)
O4-Mg2-O9^{2}	89.07(4)	O4-C2-O3	126.16(15)
O4^{2}-Mg2-O9^{2}	90.93(4)	O4-C2-H2	116.9
O2^{2}-Mg2-O9^{2}	93.28(5)	O3-C2-H2	116.9
O2-Mg2-O9^{2}	86.72(5)	C3-O5-Mg1	127.06(10)
O4-Mg2-O9	90.93(4)	C3-O5-Mg4	118.95(10)
O4^{2}-Mg2-O9	89.07(4)	Mg1-O5-Mg4	113.95(6)
O2^{2}-Mg2-O9	86.72(5)	C3-O6-Mg3	132.08(11)
O2-Mg2-O9	93.28(5)	O6-C3-O5	126.06(15)
O9^{2}-Mg2-O9	180.0	O6-C3-H3	117.0
O4-Mg2-Mg1	71.63(3)	O5-C3-H3	117.0
O4^{2}-Mg2-Mg1	108.37(3)	C4-O7-Mg1^{3}	131.18(11)
O2^{2}-Mg2-Mg1	110.33(4)	C4-O7-Mg3^{3}	128.65(10)
O2-Mg2-Mg1	69.67(4)	Mg1^{3}-O7-Mg3^{3}	97.47(6)
O9^{2}-Mg2-Mg1	148.84(3)	C4-O8-Mg3	128.54(11)

O9-Mg2-Mg1	31.16(3)	O8-C4-O7	125.60(15)
O4-Mg2-Mg1^{2}	108.37(3)	O8-C4-H4	117.2
O4^{2}-Mg2-Mg1^{2}	71.63(3)	O7-C4-H4	117.2
O2^{2}-Mg2-Mg1^{2}	69.67(4)	C5-O9-Mg1	124.64(10)
O2-Mg2-Mg1^{2}	110.33(4)	C5-O9-Mg2	118.58(10)
O9^{2}-Mg2-Mg1^{2}	31.15(3)	Mg1-O9-Mg2	116.75(5)
O9-Mg2-Mg1^{2}	148.85(3)	C5-O10-Mg4	141.75(11)
Mg1-Mg2-Mg1^{2}	180.0	O10-C5-O9	125.78(15)
O6-Mg3-O8	94.74(5)	O10-C5-H5	117.1
O6-Mg3-O1^{3}	92.65(6)	O9-C5-H5	117.1
O8-Mg3-O1^{3}	94.84(6)	C6-O11-Mg1	133.42(11)
O6-Mg3-O3	89.25(5)	C6-O11-Mg3^{1}	127.18(11)
O8-Mg3-O3	93.74(6)	Mg1-O11-Mg3^{1}	97.89(5)
O1^{3}-Mg3-O3	171.03(5)	C6-O12-Mg4	134.15(11)
O6-Mg3-O7^{1}	91.33(5)	O12-C6-O11	126.34(16)
O8-Mg3-O7^{1}	170.24(5)	O12-C6-H6	116.8
O1^{3}-Mg3-O7^{1}	92.50(5)	O11-C6-H6	116.8
O3-Mg3-O7^{1}	78.68(5)	C2X-C1X-D1	123.4
O6-Mg3-O11^{3}	170.52(5)	C2X-C1X-D2	116.9
O8-Mg3-O11^{3}	87.57(5)	D1-C1X-D2	119.7
O1^{3}-Mg3-O11^{3}	77.98(5)	C1X-C2X-D3	117.2
O3-Mg3-O11^{3}	99.79(5)	C1X-C2X-D4	122.8

O7^1-Mg3-O11^3	87.69(5)	D3-C2X-D4	120.0
O6-Mg3-Mg1	76.61(4)		

1. -x+1/2, y+1/2,1+ -z+1/2
2. -x,1+ -y,1+ -z
3. -x+1/2,-1+ y+1/2,1+ -z+1/2
4. 1-x,1+ -y,1+ -z

Table S3.6 - Torsion angles for C_2D_4 loaded α-Mg formate

Mg2-O2-C1-O1	-15.2(3)	Mg3-O8-C4-O7	3.1(2)
Mg3^1-O1-C1-O2	145.80(14)	Mg1^2-O7-C4-O8	7.9(2)
Mg1-O1-C1-O2	-16.0(3)	Mg3^2-O7-C4-O8	-149.13(13)
Mg2-O4-C2-O3	-7.7(3)	Mg4-O10-C5-O9	20.8(3)
Mg3-O3-C2-O4	-177.60(12)	Mg1-O9-C5-O10	11.0(2)
Mg1-O3-C2-O4	-17.6(3)	Mg2-O9-C5-O10	-166.98(13)
Mg3-O6-C3-O5	-1.7(3)	Mg4-O12-C6-O11	8.4(3)
Mg1-O5-C3-O6	-6.7(2)	Mg1-O11-C6-O12	12.0(3)
Mg4-O5-C3-O6	170.94(13)	Mg3^1-O11-C6-O12	174.73(13)

1. -x+1/2, y+1/2,1+ -z+1/2
2. -x+1/2,-1+ y+1/2,1+ -z+1/2

Table S3.7 - Potential Hydrogen Bonds for C_2D_4 loaded α-Mg formate

Hydrogen Bond	D—H (Å)	H ···A (Å)	D ···A (Å)	D—H ···A (°)
C2-H2 ···O8	0.95	2.59	3.161(2)	119.0
C4-H4 ···O4[1]	0.95	2.63	3.437(2)	143.6

1. -x, -y,1+ -z

Chapter 4 Summary and Future Works

4.1 Summary

In this work, the dynamics of gas molecules in various MOFs have been investigated thoroughly by SSNMR. The results displayed in this thesis suggest that ^{13}C NMR and ^{2}H NMR are both very useful for the investigation of guest-host interactions within a wide temperature range.

In chapter 2, CO_2 adsorption behavior in α-Mg formate is analyzed by ^{13}C VT experiment, and ^{1}H-^{13}C CP experiment is performed to determine the adsorption site, which has been confirmed to be hydrogen atoms from the framework. The ^{13}C VT experimental spectra are subjected to EXPRESS simulation to predict the dynamics of the adsorbed CO_2. Distinctive adsorption behaviors are found from LT and HT experiments. At low temperatures (293 K and below), all adsorbed CO_2 molecules undergo a combined motion consisting of a localized rotation upon the adsorption sites and a non-localized inter-sites hopping between two hydrogen atoms. The results of HT experiment (313 K and above) suggest that the majority of the adsorbed CO_2 molecules still undergo the combined motion, but a small portion of CO_2 act differently since they only undergo a localized rotation, no inter-sites hopping between the hydrogen sites is found. The two types of motion are both restricted as temperature increases, reflected by the decline of rotation and inter-sites hopping angles. A subtle structural change of the framework at high temperature is proposed to be responsible for the emergence of the second adsorption site and the restricted mobility of CO_2 molecules at high temperature. MD simulations done by our collaborators successfully pinpoint the minimum energy configurations of CO_2 in the channels of α-Mg formate, which are all in close proximity to three types of hydrogen atoms H1, H5 and H6 from the framework, indicating the adsorption takes place among these three types of hydrogen.

Chapter 3 introduces the ethylene adsorption behavior in α-Mg formate and CPO-27-M (M = Mg and Zn) investigated by ^{2}H NMR. The adsorbed ethylene molecules in α-Mg formate undergo two different motions. The majority of ethylene molecules undergo a combined motion of localized rotation and a non-localized twofold hopping, while others follow a localized rotation. In both CPO-27-Mg and Zn, all ethylene molecules obey a similar combined motion consisting of a localized rotation and a non-localized six-sites hopping between the unsaturated metal centres. The affinity between ethylene molecules and unsaturated Mg^{2+} in CPO-27-Mg is found to be stronger than that of Zn^{2+} in CPO-27-Zn. The discrepancy between ethylene adsorbed in α-Mg formate and CPO-27-M is due to the significant difference of the porous structures in these two types of MOFs.

4.2 Future work

In chapter 2 we propose a subtle structural change occurs at high temperature of α-Mg formate, which is deduced from the restricted motion of the adsorbed CO_2 molecules during HT experiment. However, the obtained NMR results can only be considered as indirect evidence for this assumption. Preparing good quality single crystal of α-Mg formate and conducting single crystal X-ray diffraction at high temperature is going to be a follow-up work of this thesis.

In chapter 3, we discuss the ethylene adsorption behavior in α-Mg formate. It will also be interesting to investigate the ethylene/ethane selectivity of α-Mg formate since its zigzag shape channels may have the same effect as molecular sieve, in addition to the potential H-π interaction between the framework hydrogen and the double bond in ethylene.

The MOFs studied in this work all possess relatively simple structures. It will be very interesting to investigate the ethylene adsorption behaviors in more complicated MOFs which possess multiple binding sites or different types of channels in their structures. As mentioned in chapter 1, MIL-53-Al shows a unique breathing effect, the pore size changes accordingly as pressure and temperature vary, which is different from both α-Mg formate and CPO-27-M. Therefore, it will be very interesting to study the dynamic of ethylene in this type of MOF since no such study has been reported so far.[1] Recently reported MIL-101-Cr-SO_3Ag shows high internal surface area and exceptional selectivity of ethylene over ethane that surpasses a number of benchmark solid adsorbents such as CPO-27-Mg and NaX.[2] This significant enhancement is the result of a bifunctional adsorption mechanism that involves the π-complexation formed between the double bond in ethylene molecules and the Ag (I) sites, as well as the electron donating-accepting interaction between the unsaturated Cr (III) and ethylene. The dynamics of ethylene adsorbed upon Ag (I) and Cr (III) sites are anticipated to be different since the adsorption mechanism are dissimilar, which can be easily confirmed by ^{2}H SSNMR. However, due to the difficulty in performing SSNMR experiments upon paramagnetic materials, replacing Cr (III) with diamagnetic metal cations while the structure of MIL-101-Cr-SO_3Ag still maintains will be one of the future works. Subsequently, dynamic analysis of guest molecules using SSNMR will also be performed.

Incorporating functional groups into MOFs has become a common tactic to enhance the CO_2 uptakes. Recently reported amino functionalized MIL-101-Al shows good selectivity of CO_2 over methane,[3] which is due to the strong electron donor-acceptor interaction between CO_2 and the large number of amine groups present in the pores. Mg formate MOF has also been amino modified.[4] Therefore, conducting dynamic studies of ethylene/CO_2 adsorbed in amino functionalized Mg formate and compare the results with the pristine MOF will be very interesting.

4.3 Bibliography

(1) Bourrelly, S.; Llewellyn, P. L.; Serre, C.; Millange, F.; Loiseau, T.; Férey, G. *Journal of the American Chemical Society* **2005**, *127*, 13519.

(2) Zhang, Y.; Li, B.; Krishna, R.; Wu, Z.; Ma, D.; Shi, Z.; Pham, T.; Forrest, K.; Space, B.; Ma, S. *Chemical Communications* **2015**, *51*, 2714.

(3) Serra-Crespo, P.; Ramos-Fernandez, E. V.; Gascon, J.; Kapteijn, F. *Chemistry of Materials* **2011**, *23*, 2565.

(4) Shang, R.; Xu, G.-C.; Wang, Z.-M.; Gao, S. *Chemistry – A European Journal* **2014**, *20*, 1146.

Curriculum Vitae

EDUCATION

Sep. 2013– present	• M.Sc. candidate, Department of Chemistry, Faculty of Science, Western University **Course taken at Western:** Vibrational spectroscopy (92/100); Powder diffraction (84/100); Crystallography (82/100) Chemistry 9658: Seminar (83/100)
Sep. 2006–Jun. 2013	• M.Sc. in Department of Physical Chemistry, College of Environmental and Energy Engineering, Beijing University of Technology (GPA 89/100) • B. Eng. in Department of Applied Chemistry (Biochemistry), Beijing University of Technology (GPA 3.5/4)

RESEARCH EXPERIENCE

Sep. 2013 – present	• Solid state NMR study on interactions between guest molecules and metal organic frameworks
Sep. 2010– Jun. 2013	• Preparation and characterization of non-precious intermetallic as functional electrocatalysts for fuel cell applications

WORK EXPERIENCE

Sep. 2010– present	• Laboratory Teaching Assistant for Chem 1301, 1302 and 2214, Department of Chemistry, Faculty of Science, Western University.
Sep. 2010–July. 2013	• Chair of student union in Department of Physical Chemistry, Beijing University of Technology
Aug. 2008	• Supervisor of two volunteer groups, 2008 Beijing Olympic Games

CONFERENCE AND PUBLICATIONS

- Poster presentation “A Solid State NMR Study of the Interactions Between Guest Molecules and the α-$Mg_3(O_2CH)_6$ Metal-Organic Framework” 98th Canadian Chemistry Conference and Exhibition, Ottawa, ON, Canada, Jul 13-17, 2015. Honorable mention.
- N. Zhang, X. Chen, Y. Lu, D. Xia*, et al. Nano-Intermetallic $AuCu_3$ Catalyst for Oxygen Reduction Reaction: Performance and Mechanism, *Small*, 10 (2014) 2662–2669.
- Y. Lu, N. Zhang, L. An, X. Li, D. Xia*, Synthesis of High Dispersed Intermetallic Ag_4Sn/C and Its Enhanced Oxygen Reduction Reaction Activity, *Journal of Power Sources*, 240

(2013) 606-611.

- Oral presentation on “Synthesis and Characterization of Ag-Sn intermetallic compound as novel non-precious electrocatalyst”, 16th Chinese Conference on Solid state Ionics and International Forum on Next Generation Energy Materials and Technology, Chengdu, China, Jul 6-9, 2012.